Nanoscale

REVIEW

View Article Online
View Journal | View Issue

Cite this: *Nanoscale*, 2020, **12**, 2228

Mechanisms of mechanical reinforcement by graphene and carbon nanotubes in polymer nanocomposites

Dimitrios G. Papageorgiou, * Zheling Li, Mufeng Liu, Ian A. Kinloch and Robert J. Young *

Polymer nanocomposites reinforced with carbon-based nanofillers are gaining increasing interest for a number of applications due to their excellent properties. The understanding of the reinforcing mechanisms is, therefore, very important for the maximization of performance. This present review summarizes the current literature status on the mechanical properties of composites reinforced with graphene-related materials (GRMs) and carbon nanotubes (CNTs) and identifies the parameters that clearly affect the mechanical properties of the final materials. It is also shown how Raman spectroscopy can be utilized for the understanding of the stress transfer efficiency from the matrix to the reinforcement and it can even be used to map stress and strain in graphene. Importantly, it is demonstrated clearly that continuum micromechanics that was initially developed for fibre-reinforced composites is still applicable at the nanoscale for both GRMs and CNTs. Finally, current problems and future perspectives are discussed.

Received 12th August 2019,
Accepted 2nd October 2019

DOI: 10.1039/c9nr06952f

rsc.li/nanoscale

1. Introduction

Polymer nanocomposites reinforced with graphene-related materials (GRMs) or carbon nanotubes (CNTs) have been explored extensively for use as engineering materials in a number of demanding application as a result of their low mass density and exceptional mechanical properties. In

Department of Materials and National Graphene Institute, The University of Manchester, Oxford Road, Manchester M13 9PL, UK.
E-mail: d.papageorgiou@qmul.ac.uk, robert.young@manchester.ac.uk

Dimitrios G. Papageorgiou

Dr. Dimitrios G. Papageorgiou is now a Lecturer in Materials Science at Queen Mary University of London (United Kingdom). He received his Ph.D. from Aristotle University of Thessaloniki (Greece) and continued his post-doctoral studies at the University of Manchester, working on graphene-reinforced polymer nanocomposites. His research activities focus on the fabrication of multifunctional polymer nanocomposites for advanced applications, the analysis of their reinforcement characteristics via *micromechanical theories and all aspects of their structure/property relationships. A major part of his research also involves the deformation mechanisms of nanomaterials and nanocomposites studied with the use of Raman spectroscopy.*

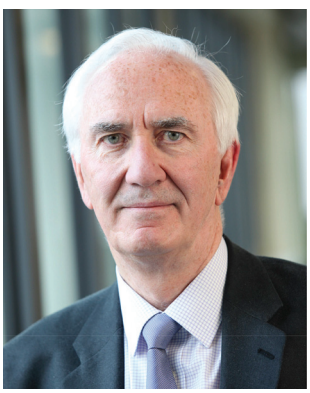

Robert J. Young

Professor Robert J. Young is the Professor of Polymer Science and Technology in the University of Manchester. He was educated at the University of Cambridge and elected to the Royal Academy of Engineering in 2006, the Royal Society in 2013 and to Academia Europaea, the Academy of Europe, in 2015. His main research expertise is upon the relationships between structure and properties in polymers and composites. He pioneered the use of Raman spectroscopy to follow the deformation of fibres and composites. His research interests have extended recently into the field nanotechnology, working in particular upon nanocomposites containing carbon nanotubes and graphene and concentrating upon commercial applications of these nanocomposites.

addition to their excellent inherent properties, the individual morphological characteristics of CNTs[1] and GRMs[2] play a major role on determining the ultimate properties of polymer nanocomposites.

Graphene is comprised of an atomically thin sheet of sp^2 carbon and constitutes the basic building block of carbon nanotubes, as shown in Fig. 1. Single-walled CNTs can be viewed as a rolled-up graphene sheet, with its one-dimensional geometry providing efficient reinforcement only along the length direction. Double-walled CNTs consist of two layers of rolled up graphene and multi-walled CNTs consist of many rolled-up graphene layers. In contrast to CNTs, the two-dimensional nature of graphene and GRMs, ensure that reinforcement takes place along all its in-plane directions. Moreover, as a result of the 2D geometry, graphene displays a larger surface to volume ratio, highly important for the creation of larger interfaces and production of stronger composites. In the present review, we will report in detail the parameters that affect strongly the reinforcing effects of both CNTs and GRMs and discuss the advantages and disadvantages of both types of filler for the production of high-performance polymer nanocomposites.

The majority of the early studies on nanocarbon composites were conducted using CNTs with research upon graphene and graphene-based nanocomposites having taken place only since its first identification and isolation in 2004.[3] Nevertheless, the extensive research studies on the GRM-based materials have now led to a better understanding of the fundamental properties for all of these sp^2 materials. In particular, GRMs have lateral dimensions of the order of microns that makes them amenable to study by a wider range of analytical techniques than in the case of CNTs. For example flakes of monolayer graphene can be easily resolved in an optical microscope,[4] unlike individual nanotubes. Hence, this review of the literature will not be undertaken chronologically. GRMs will be discussed first of all and the findings on these materials will be then related to earlier studies upon CNTs.

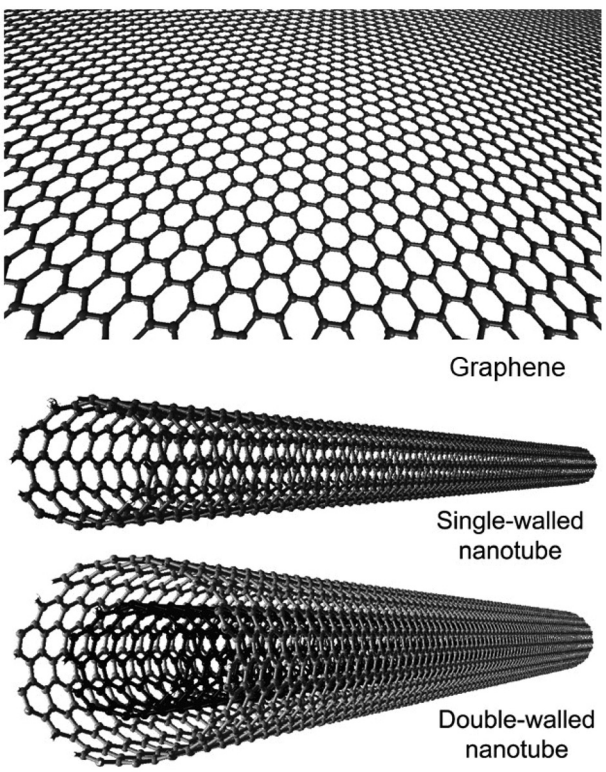

Fig. 1 Graphene and carbon nanotubes (Courtesy of Professor Feng Ding).

A number of scientific challenges have risen over the last years as a result of the rapid expansion of polymer nanocomposites, with the understanding of the elastic properties being one of the most important. There are generally two approaches for the evaluation of the mechanical properties of polymer nanocomposites. A number of researchers have suggested that the mechanics of polymer nanocomposites are similar to polymer composites reinforced with continuous reinforcements such as carbon or glass fibres.[5] In this case, the composite micromechanics, using concepts firstly introduced by Cox[6] and Kelly[7] through the use of shear-lag theory, is employed to predict the distribution of stress and strain in discontinuous fillers within a low-modulus matrix. Raman spectroscopy is a very useful tool towards the application of shear-lag theory in nanocomposites and the monitoring of the stresses within a nanofiller in a matrix, especially for carbon-based fillers with strong resonance Raman scattering.[8] On the other hand, other researchers have taken an opposing viewpoint and have suggested that polymer nanocomposites should be considered as molecular composites or self-reinforced composites, as they are actually quasi-homogeneous molecular blends.[9,10] In this case, composite micromechanics should not be applied to polymer nanocomposites since the properties are controlled by interactions between the fillers and the matrix on the molecular scale. On these terms, important indicators of interaction between the matrix and nanoparticles such as molecular nucleation and confinement (which are not taken into account by micromechanical models) may play a major role on the ultimate properties of polymer nanocomposites.

In this present review, the inherent mechanical properties of both GRMs and CNTs are discussed along with the criteria that determine the effective reinforcement from both nanofillers in polymer nanocomposites. The understanding and prediction of the mechanisms of reinforcement in such systems holds the key for the successful implementation of both nanofillers and we will subsequently explore this direction through the use of analytical models and micromechanical theories. Moreover, the application of Raman spectroscopy for monitoring the deformation of GRMs and CNTs both individually and within polymer nanocomposites through the study of the frequency shifts of the stress-sensitive Raman bands is thoroughly reviewed. Finally, this review is concluded by emphasizing the current challenges and future research directions for both GRM- and CNT-based polymer nanocomposites.

2. Mechanical properties of nanocarbons

2.1 Graphene

2.1.1 Stiffness. The Young's modulus of graphene is one of the properties that make it stand out against other materials. The exceptional mechanical properties of graphene can be attributed to the hexagonal lattice of graphene and the stability of the sp^2 bonds during various types of in-plane deformations. The work of Hone and coworkers[11] first revealed the mechanical properties of graphene through calculating the breaking force of graphene under an AFM nanoindenter. The experimental value of the second order elastic stiffness was found to be equal to $E^{2D} = 340 \pm 50$ N m^{-1}. Assuming an effective thickness of 0.335 nm, this value corresponds to a Young's modulus of $E = 1.0 \pm 0.1$ TPa, which is similar to theoretical predictions.

However, it should be noted that quite a few discrepancies exist in the graphene literature regarding the modulus of graphene, most possibly originating from the inherent and inevitable crumpling of graphene and the presence of different types of defects, both of which can decrease significantly the stiffness. For example, Ruiz-Vargas *et al.*[12] have reported decreased stiffness or crumpled CVD graphene by using nanoindentation. The same conclusion was taken from the work of Nicholl *et al.*,[13] where graphene was softened significantly as a result of cross-plane crumpling. On the other hand, the López-Polín *et al.*[14] used Ar^+ ions to introduce a controlled density of defects into mechanically exfoliated monolayer flakes deposited onto Si/SiO_2 substrates with predefined circular wells and used AFM indentation experiments to obtain the mechanical properties of their samples. Counter-intuitively, the defect-free samples showed a significantly lower stiffness than the ones with defects, when the mean distance of defects was up to ~5 nm (0.2% defect content). Various experimental methods have been utilized for the evaluation of the mechanical properties of graphene and they have been summarized well in a recent review by Kim *et al.*[15] Moreover, in Section 5, we will identify the usefulness of Raman spectroscopy for the study of the mechanical properties of both graphene and carbon nanotubes and their composites.

2.1.2 Strength. It has been established that monolayer and high-quality graphene that contains no defects is the strongest material that has ever been tested. As discussed above, Hone and coworkers[11] revealed that the intrinsic strength of a graphene monolayer is 42 N m^{-1} or 130 GPa. The work of López-Polín *et al.*,[14] where the authors introduced in-plane (sp^2) vacancy-type defects into mechanically exfoliated graphene monolayers, also revealed that a pronounced decrease of strength should be expected with increasing defect density. The measured breaking force dropped by a factor of two for the lowest Ar^+ ion irradiation dose, corresponding to a mean distance between defects is 12 nm and a 30% reduction in strength. Shekhawat and Ritchie[16] used simulation methods to study the effect of line and point defects upon the mechanical properties of nanocrystalline graphene (commonly produced by chemical vapour deposition) and demonstrated that their presence led to a significant reduction in strength. Additionally, in the work of Zandiatashbar *et al.*[17] the authors induced defects on a mechanically-exfoliated graphene monolayer with a modified oxygen plasma technique and measured the stiffness and strength of the flakes *via* AFM nanoindentation (Fig. 2a). Based on their findings, the 2D elastic modulus and strength of graphene are relatively insensitive to defects over the entire sp^3-type defect region, which comes in contrast to the work of Shekhawat.[16] Overall, it can be understood that intrinsic defects in graphene, and especially vacancy defects, can reduce the tensile strength of graphene significantly, while extrinsic defects only influence the stiffness of graphene.

In a recent report from our group,[18] the strength of mechanically exfoliated monolayer graphene was studied in detail through *in situ* Raman mapping at different strain levels (Fig. 2b and c). It was found that after the deposition of the monolayers onto a flexible polymeric substrate the failure mechanisms were either flake fracture or failure of the graphene/polymer interface. The strength of large flakes, was measured to be less than ~10 GPa (Fig. 2d) (more than one order of magnitude lower than the values reported in ref. 11), as a result of the presence of defects that locally concentrated stress.

2.1.3 Toughness. The fracture toughness of graphene is highly relevant to engineering applications and therefore the fracture behaviour of graphene and graphene-based composites is of utmost importance. Zhang *et al.*[19] utilized a micromechanical testing device and a nano-indenter within a scanning electron microscope for the determination of fracture toughness of nanocrystalline graphene. A central crack was introduced to the membranes and brittle fracture was then observed with the application of load. As expected, the fracture stress decreased with increasing crack length, the fracture toughness of graphene was found to be $K_c = 4.0 \pm 0.6$ MPa and the critical strain energy release rate was $G_c = 15.9$ J m^{-2}. In accordance with the Weibull theory developed in the 1950s, the toughness of graphene depends heavily on its weakest links, *i.e.* its defects. An interesting study of Buehler and coworkers[20] revealed that the fracture toughness of polycrystalline graphene is 20–35% higher than pristine graphene as a result of larger energy release rates that decrease with increasing grain size. Equally important, the grain boundaries near a crack tip seem to enable deformation over large areas as a result of their effectiveness in strain redistribution and the creation of complex pathways and branching of the cracks, leading to great energy dissipation.

2.2 Carbon nanotubes

2.2.1 Stiffness. Carbon nanotubes are also known for their exceptionally high stiffness, as first reported by Treacy *et al.*[21] The authors used transmission electron microscopy (TEM) in order to measure the amplitudes of the intrinsic thermal vibrations of MWCNTs and then calculated the Young's modulus to be of the order of 1.8 ± 0.9 TPa. The large uncertainty in these measurements originated from the additional

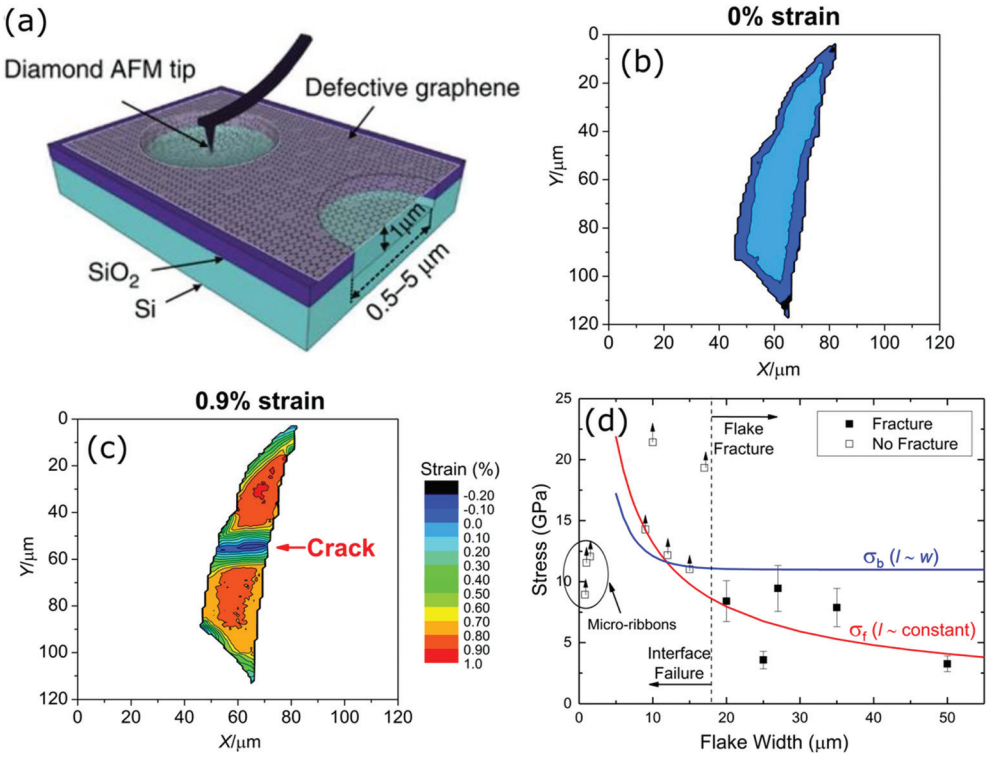

Fig. 2 (a) AFM nanoindentation on suspended graphene sheets with defects[17] (Copyright 2014, Nature Publishing Group), (b) strain contour map of a mechanically-exfoliated monolayer graphene flake before deformation (0% strain), (c) strain contour map of the same flake after fracture (0.9% strain), (d) graph of the graphene failure strength *versus* the flake width for various monolayer graphene flakes (Reproduced from ref. 18 with permission from The Royal Society of Chemistry).

heating from the electron beam and other non-equilibrium perturbations, along with the estimation of the length of the nanotubes and the variation in their structural features away from perfectly nested cylinders. The Lieber group[22] utilized atomic force microscopy (AFM) to determine the bending force *versus* displacement along unpinned lengths of MWCNTs (Fig. 3a) and the average Young's modulus was 1.28 ± 0.29 TPa, with no dependence on the diameter of the tubes. This value was very close to that obtained in the work of Krishnan *et al.*,[23] where the authors used the same method applied by Treacy *et al.*[21] and an average modulus of 1.25 TPa was obtained. In the paper of Yu *et al.*,[24] the authors also obtained the mean Young's modulus of SWCNTs ropes, which was 1.002 TPa. Salvetat and coworkers[25] compared the Young's modulus of MWCNTs produced by arc-discharge, and CVD methods and thus observed the effect of the defect type and concentration on the Young's modulus. The authors also used the AFM method, where they deposited MWCNTs on a well-polished alumina ultrafiltration membrane (Fig. 3b) and measured the deflection over the nominal force by AFM. The average modulus values for arc-discharge MWCNTs was 0.8 TPa, while for the CVD-MWCNTs, the modulus was in the order of 0.03 TPa, clearly showing that the disorder in the latter which can affect the elastic properties significantly.

The bending modulus (E_b) of MWCNTs has been studied by Poncharal *et al.*[26] by transmission electron microscope and MWCNTs with a diameter higher than 8 nm. It is known from elements of vibration analysis that a beam bends by elongation of the outer arc and compression of the inner arc. Thus, by applying this equation to CNTs, E_b can be associated with the Young's modulus of the material. The authors found that the bending modulus of MWCNTs decreases significantly from 1 TPa to almost 0.1 TPa with an increase in the diameter of the nanotubes (from 8 to 40 nm) (Fig. 3c), as a result of a different bending mode of the nanotube from a uniform elastic mode to a mode that is observed as a wave-like distortion mode (Fig. 3d). Given that the frequency of the excitation (ν_j) is known, the bending modulus (E_b) can be obtained from eqn (1):

$$\nu_j = \frac{\beta_j^2}{8\pi}\frac{1}{L^2}\sqrt{(D^2 + D_i^2)}\sqrt{\frac{E_b}{\rho}} \quad (1)$$

where D is the outer (wave-like) diameter, D_i is the inner diameter, L is the length of the nanotube, ρ is the density and β_j is a constant for the jth harmonic.

Overall, it can be seen that although there are some variations in the estimates of the stiffness particularly of CNTs, it is safe to assume that, to a first approximation, both few-layer graphene and small diameter CNTs have a Young's modulus

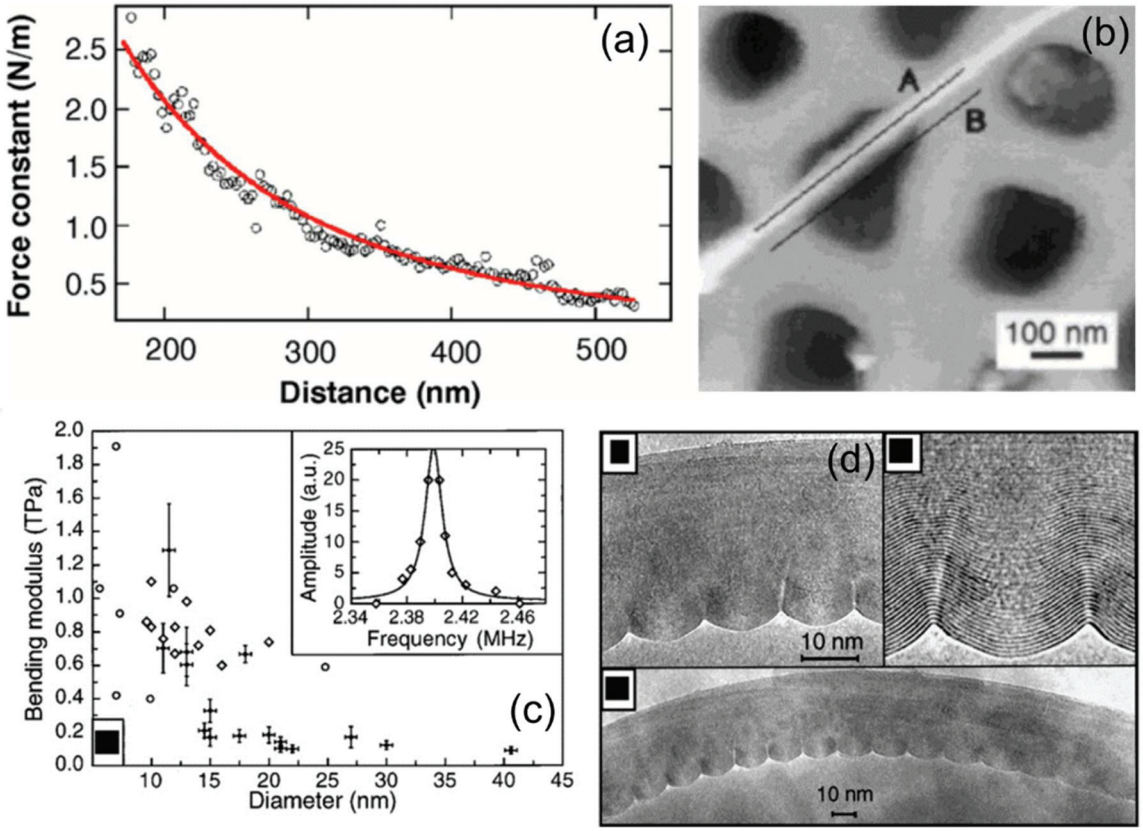

Fig. 3 (a) Graph of the force constant *versus* distance along the axis of a MWCNT[22] (Reprinted with permission from AAAS). (b) AFM image of a MWCNT adhered on an ultrafiltration membrane, with a part of it bridging a port of the membrane[25] (Copyright Wiley-VCH Verlag GmbH & Co. KGaA. Reproduced with permission). (c) Bending modulus of MWCNTs as a function of nanotube diameter, (d) high resolution TEM images of bent nanotubes, showing a wave-like distorsion (radius of curvature ≈400 nm)[26] (Reprinted with permission from AAAS).

approaching 1 TPa. Multi-layer graphene and MWCNTs have lower Young's modulus values as the result of inter-layer slippage and the hole down the centre of CNTs will reduce their modulus further.

2.2.2 Strength. The unique mechanical properties of carbon nanotubes originate from the strength of the in-plane C bonds of graphene, with the difference between them and graphene is that the elastic strain energies of CNTs are affected by the intrinsic curvature of the C–C bonds due to their tubular shape. The mechanical characterization of carbon nanotubes possesses significant challenges as a result of the limitations of characterization methods due to specimen size, specimen preparation, uncertainty in ultimate properties due to the use of indirect measurements and lack of control in nanotube structure. For the above reasons, a wide range of mechanical property values have been reported in the literature.

Ruoff and coworkers in a set of pioneering experiments[24,27] attached the ends of MWCNTs[27] and SWCNT ropes[24] onto the opposing tips of AFM cantilever probes and then the nanotube sections were stress-loaded and observed *in situ* in an SEM chamber. The deflection of the soft cantilever and the length change of the nanotubes were simultaneously recorded. The results revealed that the outermost layer of MWCNTs was the one that fractured *via* a "sword-in-sheath" mechanism, as the fragment lengths were significantly longer than the initial length of the nanotubes (Fig. 4a, b and c). The measured tensile strengths of the outer layer of MWCNTs in this work ranged from ~11 GPa to ~63 GPa, with no apparent dependence on the outer shell diameter. These values are lower than the theoretical predictions of SWCNTs,[28] as a result of structural defects, diameter reduction during elongation and the presence of small twists and/or shear loads.

In the case of the SWCNT bundles,[24] the average tensile strength ranged from ~13 GPa to ~52 GPa, while the maximum tensile strain achieved in this work was ~5.3%, which is in accordance with earlier theoretical predictions.[29] Falvo *et al.*[30] managed to strain MWCNTs up to 16% without observing a separation of the nanotube even after repeated application of bending stresses, revealing once again the high strength and flexibility of carbon nanotubes. In another study, Walters *et al.*[31] also obtained the tensile strength of SWCNT ropes, by applying force *via* an AFM tip to a length of the rope

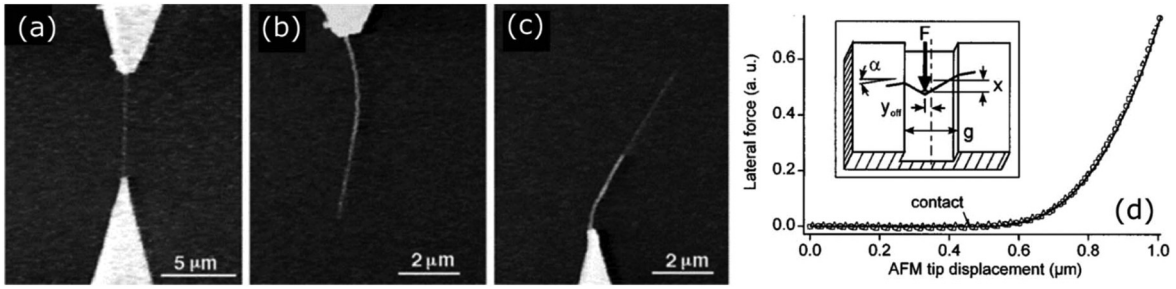

Fig. 4 SEM images of the fracture of MWCNTs under tensile load:[27] (a) a MWCNT gripped onto the AFM cantilever probes having a section length of ~6.9 μm, just before breaking, (b) a fragment of the same MWCNT just after breaking, displaying a length of ~6.6 μm, (c) the other fragment of the starting MWCNT, that was attached on the bottom AFM cantilever probe, exhibiting a length of ~5.9 μm (Reprinted with permission from AAAS), (d) the lateral force on a SWCNT rope suspended across a trench.[31] Data from four consecutive measurements on the same rope (Reprinted with permission from IOP).

that was freely suspended across a trench and by subsequently measuring the AFM tip displacement. They calculated the breaking strain to be 5.8 ± 0.9% (Fig. 4d) and the tensile strength to be 45 ± 7 GPa. Demczyk *et al.*[32] utilized a piezoelectric manipulation holder within a TEM, in order to apply tension to MWCNTs. The authors observed a tensile force at failure of 18 μN and a tensile stress to breakage of 150 GPa, which is higher than previous reports, most probably as a result of the outer walls of MWCNTs breaking almost simultaneously.

Wagner *et al.*[33] followed a different approach for the measurement of the strength of SWCNTs and embedded them into thin polymeric films to perform fragmentation tests, similar to the ones that are routinely performed for the study of the stress transfer ability of fibre-reinforced polymers. The authors found out that the tensile strength was in the order of 55 GPa by using a simple isostress model and the stress is effectively transferred from the matrix to the fibre through the nanotube ends, and the stress transfer efficiency was estimated to be at least one order of magnitude larger than conventional fibre-based composites.

The majority of experimental studies on the strength of carbon nanotubes have not achieved the strength values predicted by theoretical analyses (>100 GPa)[34–36] as a result of the presence of a number of defects along the CNTs, the inadequate measurement procedures and artefacts introduced during sample preparation. However, the important study of Peng *et al.*[37] reported measurements of MWCNTs with mean fracture strength in the order of 100 GPa, in-line with the theoretical expectations. The authors achieved these values by limiting the formation of defects *via* omitting chemical treatments during sample preparation. The nanotubes were then welded to the nanomanipulator probe and transported to a microelectromechanical stage that was placed within a TEM system. Electron irradiation induced crosslinking was achieved by focusing the TEM beam on the suspended portion of MWCNTs, a fact that led to concomitant dramatic increases in sustainable loads, while the stiffness and failure strain of the MWCNTs were only decreased slightly.

In summary, it is clear that both graphene and CNTs are capable in certain circumstances of realising strengths in excess of 100 GPa; however, in practice this is invariably reduced by the presence of either intrinsic or extrinsic defects.

3. Mechanical properties of nanocarbon-based polymer composites

3.1 Graphene nanocomposites

The exceptional mechanical properties of graphene have been one of the most important reasons for the introduction of graphene-related materials into polymers. The proficiency of the scientific community developed for the preparation of high-performance carbon nanotube nanocomposites has been subsequently extended for the preparation of multifunctional graphene-reinforced nanocomposites. We will now describe some of the most important aspects of graphene-based polymer composites for the improvement of their mechanical properties, such as the preparation methods of graphene-based composites, the dispersion and the orientation of the two-dimensional fillers, the lateral dimensions and the thickness of graphene, the waviness of the flakes and the interactions with the matrix.

3.1.1 Preparation/dispersion. The well-established methods that are most commonly used for the preparation of polymer nanocomposites include solution blending, melt mixing and *in situ* polymerization. A number of recent reviews have presented thoroughly various preparation strategies for the production of high-performing graphene-based composites.[2,38–41]

Solution blending is most probably the most widely used method for the preparation of polymer nanocomposites on the laboratory scale as a result of its versatility with the use of various solvents and the possibilities for functionalization of the flakes along with its speed and simplicity.[42–46] In this process, the polymer is initially dissolved in a suitable solvent.

The GRMs are then subsequently dispersed in a solvent that is compatible with the solvent that the polymer has already been dissolved. Graphene-related materials can be produced very successfully *via* liquid exfoliation since the energy that is required to exfoliate graphene is balanced by the solvent–graphene interaction (when the surface energy of graphene matches the one of the solvent).[47] The two elements are then mixed together (by simple mixing or shear mixing or ultrasonication) and during this process, the polymer adsorbs onto the graphene flakes. It is of utmost importance to ensure a full evaporation of the solvent, since the formation of the nanocomposite and the homogeneous dispersion of the flakes take place during this process while additionally, the ultimate properties are highly sensitive to the presence of any solvent, as it can plasticize the matrix and tends to stay at the surface. Additional limiting factors for the use of solution blending include the absence of solubility of some polymers in common solvents and the eco-friendliness of this process, as usually large quantities of solvents are used. Despite these factors, solution processing is widely used in some industries, notably in coatings and some epoxy formulations.

Melt mixing is an industrially-friendly process for the production of (mainly) thermoplastic-based nanocomposites since it is fast and inexpensive. During melt mixing, the polymer is heated above its melting/softening point and then GRMs are added into the polymer melt.[48–54] Mixing can take place by using an internal mixer with different rotor designs (Sigma, Banbury, cam or roller blades) or single-, twin-, triple- or even quad-screw extruders. Various parameters can affect significantly the dispersion of the GRMs within the polymer during melt mixing, including the temperature of mixing, the selection of the appropriate rotors or screw configuration, the feeding rates and the mixing rates. After melt mixing, additional processing steps usually take place such as hot pressing, injection moulding *etc*. which can also affect significantly the dispersion, the structure and the orientation of the fillers. The polymer nanocomposites that are produced by melt mixing can display an adequate dispersion of the fillers; however, the high shear forces that are required for the efficient mixing of the components of the system can lead to the formation of folds/wrinkles or even breaking of the nanoplatelets that lead to the reduction of their effective modulus.[55] An additional problem that is associated with the use of melt mixing is the fact that the high temperatures, particularly for high performance systems such as PEEK, can lead to the decomposition of the functional groups on the surface of the GRMs or even the decomposition of the polymer. The group of Paiva has also explored the concept of re-agglomeration, where a small-scale mixer with a relaxation chamber was utilized[56–58] for the production of GNP-reinforced polypropylene nanocomposites. The results have shown that re-agglomeration takes place in the relaxation chamber since an increase of the agglomerate area takes place, affecting significantly the subsequent dispersion rate of GNPs in the second mixing zone. A gradual decrease of the number and size of GNP agglomerates was also observed and at low shear rates, interparticle interactions induced re-agglomeration.[58] As expected, the surface modification of GNPs delayed re-agglomeration and enhanced the mechanical properties and the electrical conductivity.[57]

Furthermore, *in situ* polymerization allows grafting of the filler onto the polymer, which subsequently leads to an increase in the compatibility between the components of the system and an improved interface.[59–62] In this method, the GRMs are mixed with the monomer and then polymerization is initiated by heating or radiation after a suitable initiator is diffused in the liquid monomer. Once the reaction is initiated, the monomer that is present in and out of the layered material polymerizes and the filler nanoplatelets can be delaminated within the final polymer nanocomposites. The specific process is not easily scalable compared to melt mixing or solution blending, while additional problems include the increase of viscosity during the polymerization that prevents the production of nanocomposites at high filler loadings and leads to the creation of agglomerates.

Finally, layer by layer (LbL) assembly is another useful technique that can be used for the production of multifunctional and highly ordered graphene-based composites. In LbL assembly oppositely charged polyelectrolytes and graphene-related materials can be deposited on a substrate to create desired nano-architectures, multilayer thin films of specific thickness or hierarchical nanostructures. Usually, the interactions between the components of the assembly can be tuned by applying coordination chemistry, electrostatic and charge-transfer interactions, or simply hydrogen and covalent bonding. The 2D geometry of GRMs that provides high surface area makes them ideal for the preparation of such composites, while additionally the epoxy and hydroxyl groups in the basal plane of GO offer opportunities for the increase of the electrostatic attractive interactions and hydrogen bonding. The work of Zhao *et al.*[63] revealed that the modulus of $(PVA/GO)_{300}$ multilayer films with a bilayer thickness of 3 nm was doubled compared to the neat PVA, while more recently Vallés *et al.*[64] reported that the combination of a positively charged polyelectrolyte (PEI) and electrochemically reduced GO $(PEI/GO)_{10}$ (6 μm thick) led to very high electromagnetic interference (EMI) shielding values, in the order of ~29 dB. The review from Xiao *et al.*[65] has nicely summarized the current literature status on the LbL assembly of various nanoarchitectures.

A combination of the above-mentioned techniques has been applied in a number of studies in order to counterbalance some disadvantages from each method and ensure better dispersion of the nanofillers. For example, the group of Fina has prepared graphene-reinforced poly(butylene terephthalate) nanocomposites by inducing ring-opening polymerization within a twin screw micro-extruder.[66,67] The nanocomposites produced displayed enhanced mechanical properties and improved thermal and electrical conductivities. In a different study, Maio *et al.*[68] used a combined wet phase inversion method and melt mixing in order to produce GO-reinforced ethylene vinyl acetate (EVA) and nylon 6 (PA6) nano-

composites. The combined approach led to an efficient removal of the solvent and improved mechanical properties.

3.1.2 Orientation. The spatial orientation of the fillers is very important in polymer nanocomposites, as the reinforcement is higher when the fillers are aligned in the direction of strain. The two-dimensional nature of GRMs can enable easier alignment of the nanoplatelets, since when forces act in the out-of-plane direction of the nanocomposites, such as compression moulding or filtering/evaporation, induce an orientation in the in-plane direction.[69,70] Obviously, more sophisticated methods such as the ones that have been developed in the past for CNTs can be applied for the alignment of GRMs. For example, in the work of Wu *et al.*[71] the authors applied an external electric field in order to orient GNPs within an epoxy resin (Fig. 5a, b and c). The application of an AC electric field led to the GNPs being transversely aligned to the crack growth direction and the flakes exhibited increased interactions with the crack tip. The mode I fracture toughness was increased by nearly 900% and a number of intrinsic and extrinsic mechanisms were identified as responsible for this increase; however, the contribution from each individual mechanism is too hard to analyse.

Another interesting method has been reported by Li *et al.*[72] who used multilayer coextrusion for the fabrication of composites made of alternating layers of polymer and polymer/graphene composites. A modulus reinforcement of 118% was reported at 2 wt% of graphene as a result of the planar orientation of graphene in the individual polymer layers. The formation of other layered graphene/polymer structure, where graphene is essentially oriented in the in-plane direction, has been explored in the works of Vlassiouk *et al.*[73] and Liu *et al.*[74] In the two separate studies, CVD graphene has been sandwiched between two polymer layers of poly(methyl methacrylate) and polycarbonate. Vlassiouk *et al.*[73] clearly showed that the preparation of these model composites might be a viable method to realise the unique mechanical properties of monolayer graphene in the macroscale, as the effective modulus of graphene (E_{eff}) in the structures was found equal to 1.2 ± 0.5 TPa. However, the value of E_{eff} that was calculated in the work of Liu *et al.*[74] was significantly lower, in the order of 360 GPa. This can originate from the higher number of consecutive graphene/polycarbonate layers, where graphene within the structure can form ripples or it can also bend, something that is very difficult to monitor during the preparation procedure. Either way, this is a promising method that can utilise several of the unique properties of graphene such as the electrical or mechanical properties and the upscaling of this method can provide solutions for a number of applications.

The use of a magnetic field, which has been extensively explored for the preparation of oriented GNP-based composites was also employed for a set of polyimide/graphene composites.[75] The authors decorated graphene with supermagnetic, tethered nickel nanoparticles, oriented their fillers by applying high and low magnetic field and it was found that the tensile modulus of the highly oriented nanocomposites was increased significantly.

Finally, 3D printing for the production of polymer nanocomposites is another technique that can induce orientation of graphene-related materials within a polymer. In the work of Yang *et al.*,[76] the authors used electrically assisted 3D printing for the production of graphene-based, nacre-inspired structures with enhanced properties. The use of the electric field led to the achievement of a nanoscale-to-microscale assembly of the GNPs, while the use of 3D printing induced a microscale-to-macroscale assembly. The alignment of GNPs led to anisotropic conductivity and also creates a "bridge and interlock" phenomenon within the composites, essential to confer a stress-induced damage. Overall this is an exceptional study, taking advantage of a very strong, nature-inspire structure and modern composite fabrication techniques which led to excellent final results, revealing that the produced materials can take advantage of the multifunctional properties of graphene for the creation of smart and lightweight structures.

Polarised Raman spectroscopy has been identified as a technique that can be used to quantify the spatial orientation of graphene, which has a large effect upon its ability to reinforce nanocomposites.[78] Li *et al.*[74] applied the method to a number of GO-reinforced systems and obtained the Krenchel orientation factor (η_o), which can be subsequently substituted in a number of micromechanical equations such as the modified rule of mixtures. The local orientation of graphene is defined by its surface normal and can be seen in Fig. 5d as the z direction in the x, y plane. The Raman scattering intensity

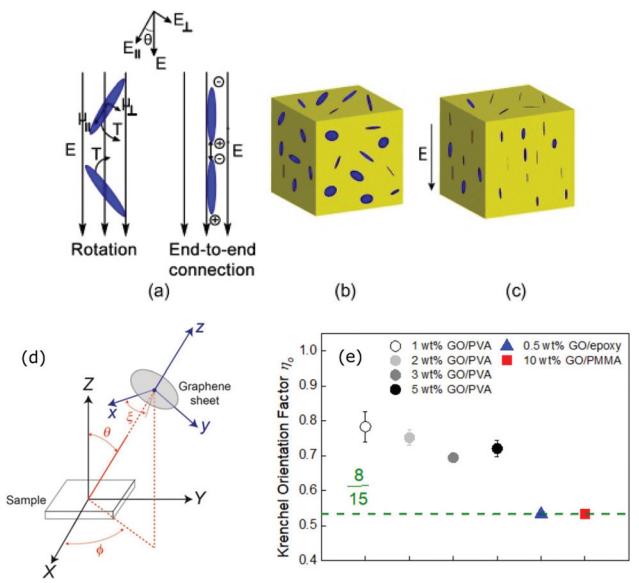

Fig. 5 Two different alignment mechanisms of the GNPs by an AC electric field through: (a) rotation (left) and end-to-end connection (right) of polarized GNPs, (b) initial random orientation of GNPs within an epoxy resin, (c) oriented GNPs along the electric field direction within the resin[71] (Copyright 2015, with permission from Elsevier), (d) the relationship between the local coordinate system of a graphene sheet (x, y, z) and the nanocomposite (X, Y, Z) defined by the three Euler angles (θ, φ, ξ),[77] (e) Krenchel orientation factor of the composites studied in ref. 77 (the dashed line represents the Krenchel factor of 8/15 for the materials reinforced with randomly distributed GNPs (Copyright 2016, with permission from Elsevier).

under VV laser polarization can then be expressed as a function of the polarization angle Φ:

$$I_{sample}(\Phi) = I_o\left\{\frac{8}{15} + < P_2(\cos\theta) > \left(-\frac{16}{21} + \frac{8}{7}\cos^2\Phi\right) + < P_4(\cos\theta) > \left(\frac{8}{35} - \frac{8}{7}\cos^2\Phi + \cos^4\Phi\right)\right\} \quad (2)$$

where I_o is the amplitude, $P_i(\cos\theta)$ is the Legendre polynomial of the i-th degree and $<P_i(\cos\theta)>$ is the average value. The Herman's orientation factor (S) is the $<P_2(\cos\theta)>$, while the higher the $<P_2(\cos\theta)>$ and $<P_4(\cos\theta)>$ values, the higher the orientation of graphene in a composite. After substitution on the orientation distribution function, the Krenchel orientation factor can be obtained by:

$$\eta_o = \frac{8}{15} + \frac{8}{21} < P_2(\cos\theta) > + \frac{3}{35} < P_4(\cos\theta) > \quad (3)$$

For a composite with a perfect orientation of the flakes $<P_2(\cos\theta)> = <P_4(\cos\theta)> = 1$, while for random orientation $<P_2(\cos\theta)> = <P_4(\cos\theta)> = 0$. Finally, for a composite where the nanoplatelets are randomly aligned, $\eta_o = 8/15$ (Fig. 5e). The important implication of this study to the general field of composites comes from the conclusion that the reinforcing efficiency of 2-dimensional materials is significantly higher than fibre or nanotube-based materials. This is because the Krenchel orientation factor for randomly oriented 1-dimensional fillers reduces the modulus by a factor of 5 ($\eta_o = 1/5$), while for 2-dimensional fillers it is only reduced in less than half. The values of $<P_2(\cos\theta)>$ and $<P_4(\cos\theta)>$ also enable the reconstruction of the full orientation distribution function of graphene flakes in composites.

3.1.3 Flake dimensions. As it is known from numerous experimental studies on fibre-reinforced composites, short fibres are less effective in reinforcing composites compared to longer or continuous fibres. This phenomenon has been explained in detail by the shear lag and other theories, where a critical reinforcement length exists for good mechanical properties. The major parameters that affect the critical length l_c are the aspect ratio of the nanoplatelets (in the case of GRM-reinforced composites) and the interfacial interaction between the filler and the matrix (interfacial strength). In the work of Gong *et al.*[5] the minimum critical length for reinforcement in a model graphene/PMMA system was found to be in the order of ~3 μm as a result of low interfacial strength of the filler and the matrix (around 1 MPa). This observation has important consequences in the production of GRMs, since methods such as liquid exfoliation usually produce small flakes, that are not able to transfer stress as effectively and modest improvements are observed in mechanical properties. A number of studies have reported that larger flakes are more effective in reinforcing polymer composites, as a result of better stress transfer than their smaller counterparts.[55,79–81] It should be noted, however, that the original lateral dimensions of the GRMs are not always the same with the dimensions of GRMs within the composites post-processing. Manufacturing processes such as extrusion, internal mixing, injection moulding, compounding and others involve the use of high shear or high stress on the 2D nanoplatelets, a fact that can lead to them bending, folding, curving or even breaking within the composites (Fig. 6). This observation can significantly reduce their effective aspect ratio and subsequently their reinforcement characteristics.

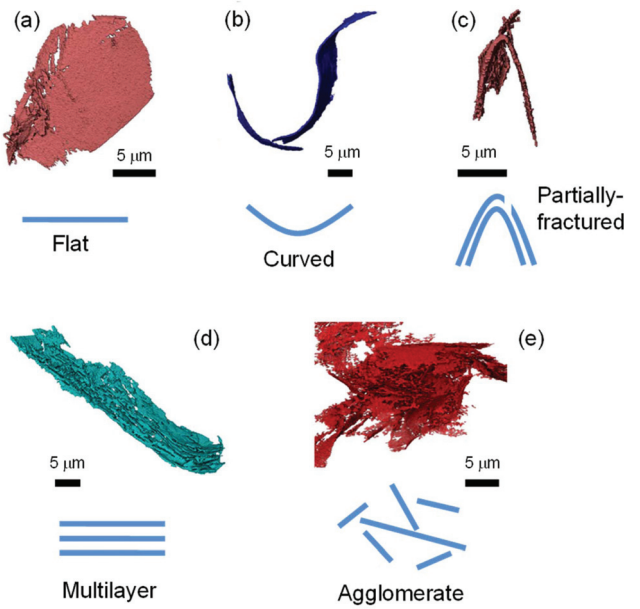

Fig. 6 The taxonomy of individual GNP flakes as obtained from X-ray computed tomography in an epoxy/GNP composite. (a) A flat flake, (b) two curved GNP flakes, (c) a curved GNP flake that fractured partially in the middle, (d) a multi-layer flake with a large number of layers, (e) an agglomerate of flakes[82] (Copyright 2019, with permission from Elsevier).

The emergence of X-ray computed tomography now enables the visualization of the "real" structure and morphology of the nanofillers within composites and provide important information regarding the effect of processing on the fillers. The recent study of Li *et al.*[82] has shed some light to this crucial issue of mechanical reinforcement from GNPs and the authors suggested that a size reduction of at least a factor of two should be expected for epoxy/GNP composites prepared by stirring and sonication of GNPs within the resin. Very long flakes are clearly more prone to bending and agglomeration/restacking than smaller ones, so a balance of the lateral dimensions should always be kept in mind. This effect can be observed more commonly in materials with low shear modulus (*i.e.* elastomers) since the stress transfer is less effective than stiffer materials and the interfacial strength of the filler/matrix interface is small. For example, in the case of natural rubber reinforced by GNPs[83] or GO[84] with different lateral dimensions, the Young's modulus of the composites with the smaller flakes was higher than that with the largest flakes.

3.1.4 Wrinkling. The out-of-plane deflection that is caused either by shear or in-plane compression in GRMs is called wrinkling. Generally, the functionalized forms of GRMs, such as GO display a more wrinkled structure as a result of the disrup-

tion of the network of sp^2 bonded carbons from the functional groups, that leads to an increased possibility for deformation and the small buckling threshold of graphene that cannot support even a small level of shear or compression.[85] Wrinkles can significantly affect the roughness and the properties of the nanoplatelets. The presence of wrinkles in the structure of GRMs is somewhat controversial since their presence essentially reduces the aspect ratio of the platelets; on the other hand, they can affect the stress distribution around the matrix and improve the stress transfer due to an enhanced shear strength of the graphene/polymer interface.[86] Additionally, there are studies that report an increase of the interactions with the polymer chains, leading to better properties.[87] The early work of Ramanathan *et al.*[88] revealed that wrinkled single layer graphene increased interactions with the matrix, which has as a result a higher enhancement of the mechanical properties at low loadings, compared to expanded graphite or carbon nanotubes. A similar conclusion can be taken from the study of Rafiee *et al.*[89] for epoxy/graphene composites, where the authors reported that the wrinkled (rough) surface of graphene led to enhanced filler/matrix adhesion and interlocking at the interface. The wrinkles are highly irregular; however, and the application of high stress during the manufacturing or testing of the composites can alter the wrinkling pattern.

Moriche *et al.*[90] demonstrated that the composite preparation method can alter the morphology of the nanoplatelets significantly and consequently, their properties. The authors studied epoxy/GNP composites prepared by different methods and found out that when GNPs are firstly dispersed by sonication, they retain their wrinkled morphology, which leads to higher residual stress in the nanocomposites. On the other hand, the calendering method enabled the separation and exfoliation of the nanoplatelets and their extension *via* flattening (Fig. 7). The number of calendering cycles is important as at higher cycles number a higher residual stress was observed. According to Wang *et al.*[91] the amplitude (A) (eqn (4)) and wavelength (λ) (eqn (5)) of a wrinkle is directly proportional to the flake dimensions (length and thickness):

$$A^4 \approx \frac{16\nu L^2 t^2 \varepsilon}{3\pi^2(1-\nu^2)} \quad (4)$$

$$\lambda^4 \approx \frac{4\pi^2 \nu L^2 t^2}{3(1-\nu^2)\varepsilon} \quad (5)$$

where ν is the Poisson's ratio, L is the graphene length, t is the graphene thickness and ε is the edge contraction on a suspended graphene sheet.

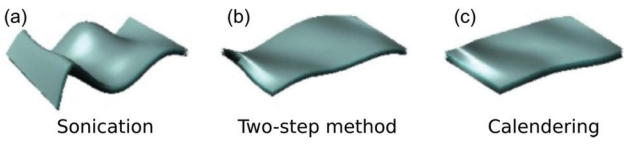

Fig. 7 Schematics of the morphology of GNPs within an epoxy resin after using different preparation techniques[90] (Copyright 2015, with permission from Elsevier).

3.1.5 Interfacial interactions. The ultimate properties of graphene-based polymer nanocomposites are highly dependent on the dispersion of the fillers and the interfacial interactions between the matrix and the filler. The interface of polymer nanocomposites can be engineered by functionalizing GRMs. Generally, graphene can be modified relatively easily by using covalent and non-covalent methods. Covalent functionalization takes places at the edges and the surface of graphene flakes and is based on the formation of covalent links between graphene and other functional groups while non-covalent functionalization involves processes such as hydrogen bonding, electrostatic interactions, π–π stacking interactions, polymer wrapping and other methods.[92,93] The functional groups on the surface of GRMs can be small motifs or polymer chains that can subsequently form strong physical or chemical interactions between the graphene flakes and the polymeric matrices.[88,94–97] Based on the preparation process, different strategies for the enhancement of interfacial interactions should be followed. For example, when using solution blending, the polymers should be compatible with the solvents that will be used for the functionalization and exfoliation of the GRMs. For *in situ* polymerization, the graphene nanoplatelets can be functionalized prior to their mixture with the monomers or the pre-polymers, while for melt mixing the temperature of mixing should be taken into account since organic functional groups are not thermally stable at high temperatures.

3.2 Carbon nanotube nanocomposites

Even though the intrinsic properties of carbon nanotubes can ensure the good performance of the produced CNT-based nanocomposites, there are several parameters, the control of which can ensure the maximization of performance of CNTs in the composites. Some of the most important parameters include the dispersion and orientation of CNTs, the length of the CNTs, the waviness, the interfacial interaction between CNTs and the matrix and the chirality. Several investigators have attempted to evaluate those parameters individually and in combination and they will be discussed in the following section.

3.2.1 Preparation/dispersion. The state of dispersion of nanomaterials within polymer nanocomposites is known to be of vital importance for the physicochemical properties of the ultimate materials. The differences in the distribution of micro- and nano-scale fillers can be seen in Fig. 8, where the very large quantities of CNT and GNP individual nanoparticles (only at 0.1 vol%) within a reference volume of 1 mm^3, lead to an exceptionally large surface area within the nanocomposite.[93] In the case of CNTs, the achievement of homogeneous dispersion has been proven to be a challenging task because of the high van der Waals interactions between individual nanotubes, which leads to the formation of tangled intertwined agglomerates. The generation of these agglomerates increases the viscosity of the matrix pronouncedly, obstructing the processing procedure and making the further enhancement of the properties difficult. Especially for the case

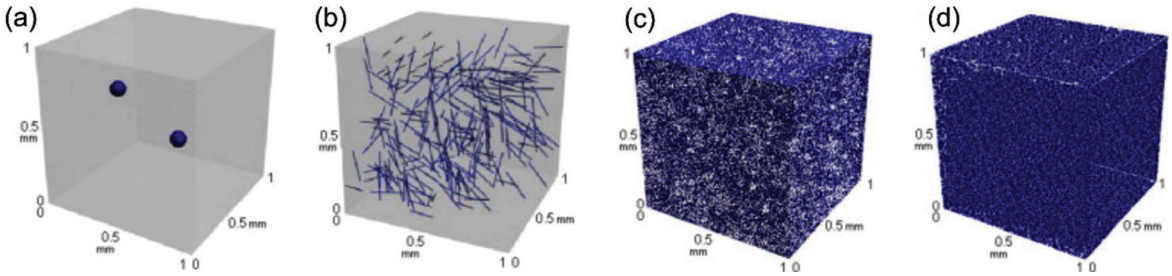

Fig. 8 Distribution of micro- and nano-scale fillers (filler content: 0.1 vol% in a reference volume of 1 mm^3) (a: Al_2O_3 particle; b: carbon fibre; c: GNP; d: CNT)[98] (Copyright 2010, with permission from Elsevier).

of the mechanical properties, the irregular shape of the agglomerates and their low aspect ratio leads to a poorer interface between the matrix and the filler and failure is known to initiate at these points, since they act as stress concentrators. Numerous preparation strategies have been reviewed[98–102] for the efficient dispersion of CNTs within polymer matrices and we will now discuss briefly some of the most important ones.

Various techniques can be employed for the melt processing of nanocomposites, such as extrusion,[103] injection moulding,[104] calendaring,[105] compression moulding[106] and others. One of the most popular approaches for the production of CNT-based composites is the blending of the polymers with nanotubes at high filler content to form a masterbatch that is subsequently diluted by adding pure polymer during production. The specimens are then produced by either injection or compression moulding. This process is also favoured by industry since handling of nanomaterials for direct incorporation into composites at varying filler loadings can be challenging. The majority of studies that have followed this approach have reported excellent mechanical properties at even high filler loadings.[107–112] The group of Potschke has investigated extensively the effect of CNTs in a number of polymeric matrices *via* melt mixing and masterbatch dilution. In their research, they evaluated a number of important characteristics for the efficient dispersion of CNTs within a polymer matrix such as the screw profile, the temperature profile, the rotation speed, the injection moulding parameters and the specific mechanical energy.[113–118] In general, higher extrusion/rotation speeds are known to lead to smaller agglomerates and better dispersion due to the higher level of shear stress that is acting on the primary agglomerates; this fact can, however, lead to a decrease of the nanotube length and a subsequent deterioration of their intrinsic properties. The dispersion of the initial agglomerates through the creation of secondary agglomerates (or clusters) of CNTs *via* thermal annealing in the quiescent melt as well as under shear deformation is certainly an interesting one, as it has been shown to lead to a significant increase in electrical conductivity due to the formation of a network of interconnected agglomerates.[119,120] The overall process takes place during the mixing and includes the initial wetting of the primary agglomerates by the polymer, the weakening of the agglomerates from the infiltration of the polymer chains, then the dispersion of agglomerates by erosion and rupture and finally the distribution of the individual nanotubes in the polymer. The manipulation of shear and the elongational flow during the preparation procedure is critical in this case since it can either lead to a build-up or a destruction of the secondary agglomerates, which is subsequently reflected on the ultimate properties.[119]

Solution blending is also one of the most popular methods for the production of polymer nanocomposites and for the dispersion of fillers that are known to form agglomerates readily. This method involves the dispersion of CNTs within a polymer or solvent by some form of energetic agitation, the mixing of CNTs and the polymer and the subsequent evaporation of the solvent for the production of a composite film. The functionalization of CNTs is known to improve the dispersion of CNTs significantly. Critical parts of this process for the production of the nanocomposite are the correct selection of the solvent for the dispersion of the CNTs, the time and energy applied to the CNT/solvent suspension, the efficient mixing of the polymer/CNT blend and the full evaporation of the solvent. In addition, the final step of the solution blending process can commonly induce re-agglomeration of the CNTs so strategies such as the coagulation have been applied where the CNT/polymer suspension is poured into an excess of nonsolvent. This approach has as a result of the entrapment of the precipitation of CNTs from the polymer chains, preventing them from bundling.[121,122]

In situ polymerization involves the dispersion of nanotubes in monomers and the subsequent polymerization of the monomers.[123] This process is quite useful for the preparation of nanocomposites when the polymer matrix is resistant to chemicals or possesses properties that make melt mixing difficult (*i.e.* high melting point, high viscosity *etc.*). The functionalization of the CNTs prior to the mixing with the liquid monomer or solvent can induce better dispersion within the composites. It should be noted, though, that at higher CNT contents there is a lack of polymerization reactions as well as the major increase of viscosity. Nevertheless, *in situ* polymerization enables grafting of the polymer molecules onto CNTs and the formation of covalent bonding between the CNTs and the matrix by various condensation reactions, leading to significantly improved mechanical properties.

As mentioned earlier, LbL assembly is a versatile technique that can enable the creation of high performing, multifunc-

tional nanocomposite materials. In the early work of Mamedov *et al.*,[124] the authors fabricated free-standing single-walled CNT/polyelectrolyte membranes with enhanced strength, as a result of the minimization of structural defects originating from phase segregation. Since then, a number of works have dealt with the preparation and the properties of CNT-based LbL assemblies and the enhanced performance of the nanocomposites in terms of the mechanical, electrical and other properties have been clearly exhibited.[125–128]

Combinations of the above-mentioned techniques have also been employed by a number of groups for the efficient preparation of high-performing CNT-based composites. For example, CNTs have been coated with polyethylene by *in situ* polymerization of ethylene catalyzed directly from the nanotube surface and they have been subsequently melt-blended with HDPE,[129] ethylene-*co*-vinyl acetate (EVA)[130] or polycarbonate.[131] Another combination that has been applied is the use of solution blending and extrusion such as in the studies of Thostenson and Chu where CVD-MWCNTs were dispersed in a solution of polystyrene in tetrahydrofuran (THF) to form a nanocomposite film, which was subsequently chopped and extruded. The resultant nanocomposites showed improved tensile modulus, yield strength and ultimate strength.[132]

3.2.2 Orientation. The one-dimensional nature and high aspect ratio of CNTs can be exploited further through their alignment. In this way, their exceptional anisotropic properties can be realized by further improving the mechanical and multifunctional properties of the nanocomposites. It should be pointed out that orientation is not always preferable for mechanical reinforcement since the anisotropy can reinforce the material significantly in the direction of alignment, while the tensile properties can be worsened in the other directions. Various strategies have been explored in the literature for the alignment of CNTs, including the application of an electric or magnetic field, the use of mechanical force, and electrospinning.[133]

Electric fields have been utilized in a number of creative ways in order to induce alignment of CNTs within a matrix. Importantly, the behaviour of CNTs can be controlled by adjusting the gap between the electrodes of the AC or DC electric fields and it is highly dependent on the surface charge and the type and frequency of electric field. More specifically, in the application of an AC electric field the alignment of CNTs takes place due to their dielectrophoretic behaviour, since the electrophoretic mobility of the field is zero and CNTs essentially disrupt the homogeneity in the electric field. Thus, the use of AC electric fields has been reported to be more effective in the production of uniform and aligned networks, such as in the work of Martin *et al.*[134] The parameters of the AC electric field, such as the field voltage and frequency are vital for inducing orientation of CNTs; it should be noted, however, that increased voltage can also promote a degree of agglomeration, so a fine balance has to be maintained.[135] Moreover, as the research of Ma *et al.* has shown, oxidized MWCNTs were dispersed and aligned in PMMA at a higher degree than their un-functionalized counterparts due to a higher amount of charges and a larger dipole moment.[136]

On the other hand, on the application of a DC electric field, the CNTs move towards the electrodes of opposite charge as a result of their electrophoretic mobility and the surface charge. The alignment in this case can be controlled by the level of applied potential. The important work of Kim and coworkers[137] evaluated the orientation of MWCNTs in an epoxy matrix as a function of the DC electric field. As well as an exceptionally-low electrical percolation threshold of about 0.0031 vol% in the direction of alignment, the tensile modulus of the oriented composites at 0.3 wt% CNTs was 40% higher than for the neat epoxy, while the fracture toughness was 51% higher at the same filler content. For higher filler loadings, the Young's modulus was reduced, as a result of a reduced degree of alignment; the increased loadings also lead to an increase in the viscosity of the epoxy resin, thus making it more difficult for the CNTs to move and orient under the DC field. It should also be noted that the transverse storage modulus obtained by dynamic mechanical analysis for the aligned CNT composites was lower than that of the randomly-oriented CNT composites due to the lower restriction of the macromolecular chains of the resin in the transverse direction, similar to the work of Zhu *et al.*[138]

The application of a magnetic field is another method for the fabrication of oriented MWCNT-based nanocomposites.[139,140] The fabrication of MWCNTs commonly involves the use of metal catalysts such as Fe, Co or Ni, an amount of which can remain in the MWCNTs after the preparation procedure and subsequently respond to the application of low magnetic fields. Ma *et al.* aligned CNTs with Ni particles as a residual catalyst in an epoxy under a low magnetic field of 0.4 T.[141] The authors reported that the alignment of CNTs perpendicular to the crack plane resulted to significantly higher fracture toughness and energy compared to the randomly oriented CNT samples or to the samples where CNTs were oriented parallel to the crack plane. Another similar method involves the coating of CNTs with superparamagnetic particles, which can facilitate the orientation of the nanotubes.[142] Kimura *et al.*[143] first reported on the use of a magnetic field of 10 T for the polymerization of a polyester resin and MWCNTs. The storage modulus measurements revealed that the alignment of the MWCNTs attributed a higher increase of the modulus in the parallel direction compared to that for the perpendicular direction. There are also reports where the orientation of MWCNTs in an epoxy matrix by magnetic field has also been shown to degrade the mechanical properties of the system due to a decoupled orientation of the polymer chains due to the inhibition of the macromolecular chain movement and the formation of a highly-disordered complex microstructure.[144] This fact once again reveals that the alignment of CNTs in an epoxy resin is highly dependent on the cross-linking molecules and the core polymer component of the resin.

The alignment of CNTs can also be attained by the use of mechanical force during the processing of the nanocomposites. For example, flow-induced alignment of MWCNTs

has been achieved by the application of intense drag/shear forces during the moulding process in a variety of polymer matrices.[145–148] Mechanical stretching is also a technique that has been proven to produce aligned CNTs.[149,150] Jin *et al.*[151] followed this procedure for CNTs in a polymerized matrix, however, it is important to understand that the large draw ratio can lead to unfavourable interface binding between CNTs and the matrix. Also, Schulte and coworkers aligned high loadings of CNTs in an epoxy matrix, at a MWCNT fraction of 68 wt% by applying hot-press infiltration through a semi-permeable membrane. The Young's modulus in the direction parallel to the alignment was in the order of 36 GPa, while the electrical conductivity was 3.7×10^4 S m^{-1}.

Finally, electrospinning is another method, amongst many, that can be used for the production of aligned CNT-based nanocomposites.[152,153] A number of studies, such as the one of Cheng and coworkers[154] on polyacrylonitrile/MWCNT composite nanofibre sheets produced by electrospinning have reported an improvement in the mechanical properties.[155–157] More recently King *et al.*[158] managed to engineer single- and double-walled CNTs into highly aligned arrays by electrospinning poly(ethylene oxide) and functionalized CNTs solutions (Fig. 9). Mechanical testing revealed that at a CNT loading of 3.9 wt%, the strength and ductility were improved by a factor of 3, while the modulus increased by a factor of 4. The process can be further optimized in order to allow a higher control of the nanotube orientation, by using a magnetic field. Magnetic field assisted electrospinning is easy to set up by using just two magnets added to conventional electrospinning, the CNTs are highly-aligned and the resultant fibres can be easily transferred to other substrates.[159,160]

The quantification of the spatial orientation of CNTs was made firstly by Liu *et al.*[161] by adjusting the theory developed earlier to quantify the orientation of polymer chains, including liquid crystals.[162] The orientation of a carbon nanotube is defined by its axial direction in a coordinate system. The Raman scattering intensity, obtained from the products of the tensors of the CNT and the vectors of Raman laser representing its polarisation directions, can be expressed as a function of the polarization angle Φ for the VV polarisation configuration:

$$I_{\text{sample}}(\Phi) \propto \frac{1}{5} + < P_2(\cos\theta) > \left(-\frac{2}{7} + \frac{6}{7}\cos^2\Phi\right) + < P_4(\cos\theta) > \left(\frac{3}{35} - \frac{6}{7}\cos^2\Phi + \cos^4\Phi\right) \quad (6)$$

where $P_i(\cos\theta)$ is the Legendre polynomial of the i-th degree and $<P_i(\cos\theta)>$ is the average value. Specifically, the definition of $<P_2(\cos\theta)>$ is the same as the well-known Herman's orientation factor (S) commonly used in polymer field. From eqn (6) it can be understood that the higher the $<P_2(\cos\theta)>$ and $<P_4(\cos\theta)>$ values, the better the orientation of CNTs in a composite. $<P_2(\cos\theta)>$ and $<P_4(\cos\theta)>$ being equal to unity stands for the unidirectional orientation of CNTs, while $<P_2(\cos\theta)>$ and $<P_4(\cos\theta)>$ being equal to 0 means that all the CNTs are randomly oriented three-dimensionally in bulk. This, as calculated by Krenchel[163] for the case of fibres, reduces the reinforcement efficiency to only 1/5, as compared to unidirectionally-oriented CNTs in composites.

3.2.3 Nanotube dimensions. The length of CNTs is a very important parameter for the mechanical reinforcement of polymer matrices as a critical fibre length exists for the efficient load transfer from the matrix to the fibre and the stiffening of the nanocomposite. However, very long tubes have increased tendency to agglomerate and form entaglements; thus, they are much more difficult to disperse homogeneously within a matrix. This has been clearly shown in the study of Bai and Allaoui, where the shortest MWCNTs outperformed the longest ones in terms of mechanical properties due to a reduction of the agglomerates as a result of their length.[164] Moreover, it should be kept in mind that high energy processes such as sonication or ball milling that precede the mixing procedure are known to lead to a damage of the nanotube structure and a decrease of the average length.[165] The critical length l_c for effective load transfer from a matrix to the fibre is given by the following equation:

$$l_c = \frac{\sigma_f d}{2\tau_c} \quad (7)$$

where σ_f is the tensile strength of the fibre, d is the diameter of the fibre and τ_c is the strength of the fibre-matrix bond. It implies that for CNT lengths lower than the l_c, the CNTs cannot be gripped to the matrix and as a result they will slip during the elongation procedure, therefore not transferring stress effectively. Wan *et al.*[166] established the minimum critical length of SWCNTs to be in the order of 270 nm if no weak interphase exists between the filler and the matrix. The authors also revealed that the effective modulus of long SWCNT fibres can be about twice that of short fibres (Fig. 10a). There are also studies such as the one by Wang *et al.*[167] where the differences in the length of MWCNTs did not affect the elastic properties of the composites. It should be noted that even though in this work the length of the tubes increased, the diameter also increased and as a result the

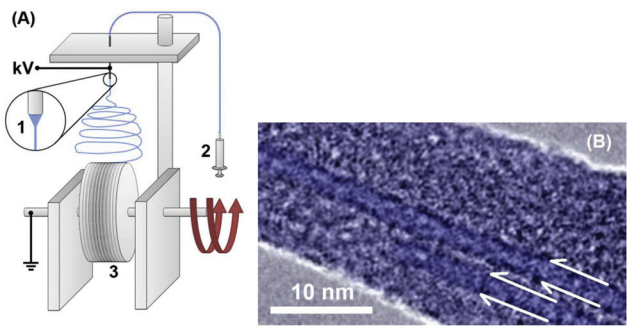

Fig. 9 (A) Schematic diagram of the electrospinning setup used by King *et al.*[158] showing (1) the single needle spinneret, (2) the pumped syringe and (3) the grounded high speed collector where full alignment of the CNTs takes place within the fibres. (B) The coloured TEM micrograph shows the CNTs embedded within the PEO electrospun nanofibre (Copyright 2018, with permission from Elsevier).

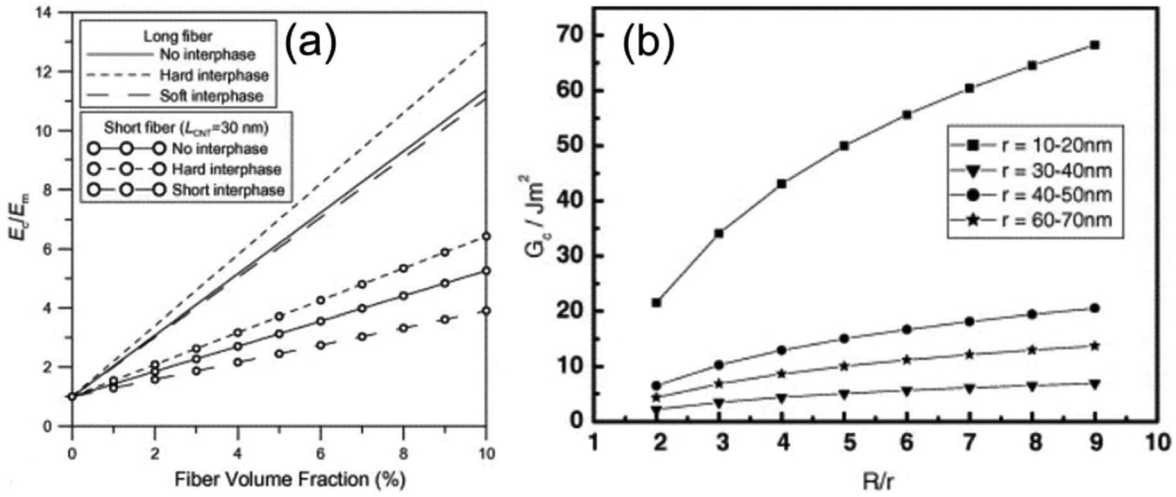

Fig. 10 (a) Effect of fibre length and quality of the interphase on the effective Young's modulus of the composite[166] (Copyright 2005, with permission from Elsevier). (b) Calculated interfacial fracture energy for the pullout of a single MWCNT from a polyethylene–butene matrix for various R/r values, where R/r is a stress transfer parameter, r is the fibre radius and R is the matrix radial distance from the axis of the fibre, at which shear tends to be zero[170] (Copyright 2004, with permission from Elsevier).

aspect ratio of the MWCNTs remained unchanged; this can explain the mechanical properties of the composites being unaffected.

The diameter of the tubes is another important parameter for the reinforcement of polymeric matrices. SWCNTs possess smaller diameters and larger specific surface areas than MWCNTs. This large surface area can be beneficial for good stress transfer; however, it induces strong attractive forces between CNTs, which subsequently leads to excessive agglomeration. Multi-walled CNTs display larger diameters and as a result can be dispersed more efficiently but their shorter length can lead to the formation of a smaller interface for stress transfer and lower aspect ratio, thus poorer mechanical properties. Larger diameter nanotubes can also exhibit a lower effective modulus due to inter-wall slippage.[168] It is clear, therefore, that a fine balance need to be maintained between the number of walls and the specific surface area in order to compromise between mechanical reinforcement and homogeneous dispersion. Cadek *et al.* showed that the low diameter MWCNTs were more efficient for reinforcing poly(vinyl alcohol) (PVA) since SWCNTs formed a number of agglomerates and DWCNTs were able to reinforce the matrix only up to 1 wt%.[169] Wagner and coworkers have identified that smaller diameter nanotubes formed a stronger interface with a polyethylene-butene matrix, a fact that led to a higher fracture energy, as measured by single fibre pullout tests (Fig. 10b).[170] Finally, the work of Thostenson and Chou has clearly shown that larger nanotube diameters leads to a lower effective modulus and to the occupation of a greater volume fraction in the composite, compared to lower diameter nanotubes.[171]

3.2.4 Waviness/curvature. The nanotube waviness or curvature can act as a limiting agent for the maximization of the mechanical properties of a polymer matrix, leading to a decreased stiffness. The waviness of nanotubes is not a parameter that can be fully addressed experimentally and for this reason, several attempts have been made in the literature for modelling the behaviour of nanotubes and its effect on the effective modulus of the composites by applying micromechanics,[172,173] molecular dynamics simulations,[174] finite element methods[175–178] and combinations of them.[179] For example, Fisher *et al.* proposed a combination of finite element and micromechanical methods for the determination of the effective modulus of a wavy CNTs embedded in a matrix,[180] and it was found to be dependent on the ratio of the sinusoidal wavelength to the nanotube diameter.[181] The general consensus from all of these studies is that the high waviness of nanotubes has a detrimental effect on the mechanical properties of the CNTs and especially on the effective axial stiffness that they contribute to the nanocomposite.

3.2.5 Interfacial interactions. As mentioned earlier, the performance of CNTs within polymers is heavily dependent on the interfacial interactions between the components of the system. The aromatic nature of the carbon bonds on the CNT walls makes them chemically stable and the interaction of the un-functionalized CNTs with the polymer takes place mainly through weak van der Waals interactions. Different chemical modification schemes have been explored in the literature for the enhancement of the polymer/nanotube interactions such as π–π or electrostatic interactions, chemical bonding and van der Waals force. Numerous researchers have devoted their efforts in fine-tuning these interactions and the introduction of functional moieties for the development of a strong chemical affinity between the corresponding polymer matrix and nanotubes for the efficient transfer of mechanical load. The topic of chemical functionalization of CNTs for the enhance-

ment of the interactions with the polymer matrices has been covered extensively by a number of well-cited reviews and will not be discussed further.[98,99,101,182]

4. Composite micromechanics

4.1 Rule of mixtures

The simplest and most straightforward relationship that was developed originally for the description of the reinforcement of a low modulus matrix by a high modulus fibre, for stress parallel to the fibre direction, is the rule of mixtures. The Young's modulus of a composite E_c consisting of infinitely long and aligned fibres is given by:

$$E_c = E_f V_f + E_m(1 - V_f) \quad (8)$$

where E_f and E_m are the moduli of the fibre and the matrix and V_f is the volume fraction of the fibre. Despite its simplicity, this relationship has been confirmed on numerous occasions to be effective in describing the essence of fibre reinforcement, especially at low fibre contents. Thus, when strain is applied to both the fibre and the matrix, the stress in the fibres is much higher than that in the matrix, with the fibres carrying most of the load and subsequently reinforce the low modulus matrix. The above relationship has been applied in a large number of investigations upon polymers reinforced with GRMs[2] and the results clearly revealed the differences in the stress transfer mechanisms among polymer matrices with different degrees of stiffness. From the E_f *versus* E_m plots for different GRMs (Fig. 11) it was concluded that the filler modulus scales with the matrix modulus and stress is transferred more effectively when the matrix is stiffer.

However, given the fact that the above equation does not take into account important factors such as the orientation, the length (or aspect ratio) and the agglomeration of the fibres (which are all very important in the case of nanocomposites), it should be mainly used as an approximation for the modulus of the filler or of the composite. Based on this, a modified rule of mixtures has also been proposed for the calculation of the Young's modulus of a composite:

$$E_c = E_{eff} V_f \eta_o \eta_l + E_m(1 - V_f) \quad (9)$$

where E_{eff} is the effective modulus of the fibres, η_o is the Krenchel orientation factor, which depends on the average orientation of the fibres with respect to the applied stress and η_l is the length factor, which depends on both the length of the fibre and the interface between the fibre and the matrix. The Krenchel orientation factor can be obtained experimentally, as it has been shown in the previous section, *via* the use of polarized Raman spectroscopy for the correlation of the degree of spatial orientation of the reinforcement with the mechanical properties of the nanocomposites. Other techniques such as X-Ray diffraction,[183,184] transmission electron microscopy,[185] and fast Fourier transformation with scanning electron microscopy (SEM)[186] have also been used. Overall, as mentioned earlier, the Krenchel orientation factor for aligned nanotubes or nanoplatelets is equal to unity (η_o = 1), while for the case of nanotubes oriented in two dimensions the η_o = 3/8, while for nanoplatelets η_o = 1. Finally, for randomly oriented nanotubes, the η_o = 1/5, while for nanoplatelets η_o = 8/15 (Fig. 12).[78,187] Since random orientation is the most common situation for polymer nanocomposites where graphene-related materials or carbon nanotubes are used as reinforcements, the higher reinforcing efficiency in this respect, of the GRMs is clear.

The length factor (or fibre length distribution factor) can be calculated by using the Cox equation:

$$\eta_l = 1 - \frac{\tanh(ns/2)}{ns/2} \quad (10)$$

where s is the aspect ratio of the fibre and $n = \sqrt{\frac{2G_m}{E_f}\left(\frac{t}{T}\right)}$. The main assumption behind the use of the length factor is that the matrix and the filler remain elastic during deformation, the interfacial bonding is perfect, while on the basis of the shear-lag theory the shear stress at the ends of the fibre is maximum and falls to zero after half the critical length.

Li *et al.*[188] included an agglomeration factor (η_a) within the modified rule of mixtures, taking values between 0 and 1. It is 1 for perfect dispersion and effective stress transfer from the matrix to the filler and 0 is for major agglomeration, so that the effect from the nanoscale dimensions of the filler is diminished and thus nearly no stress transfer takes place. The modified Rule of Mixtures (mROM) in this case takes the form:

$$E_c = \eta_o \eta_l E_{eff} \eta_a V_f + E_m(1 - V_f) \quad (11)$$

and the product $\eta_a V_f$ can be considered the effective volume fraction, which essentially is the volume fraction of the flakes that transfer the strain effectively as a result of good dispersion and no agglomeration with other nanoflakes.

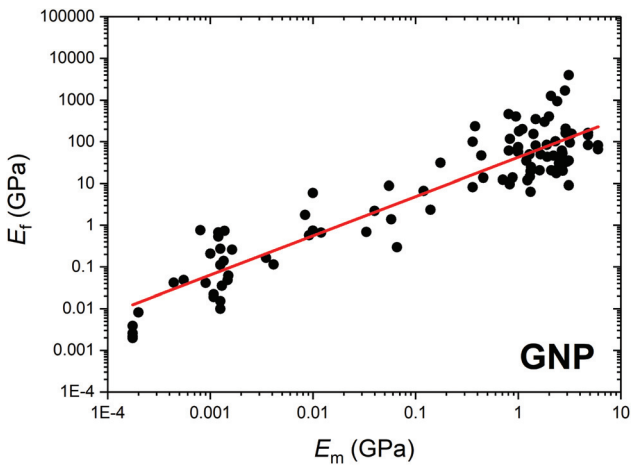

Fig. 11 Filler modulus (E_f) *versus* matrix modulus (E_m) for a number of different literature reports where polymers of varying degrees of stiffness were reinforced by graphene nanoplatelets. The solid line represents the linear fit of the data and has a slope of unity[2] (Copyright 2017, with permission from Elsevier).

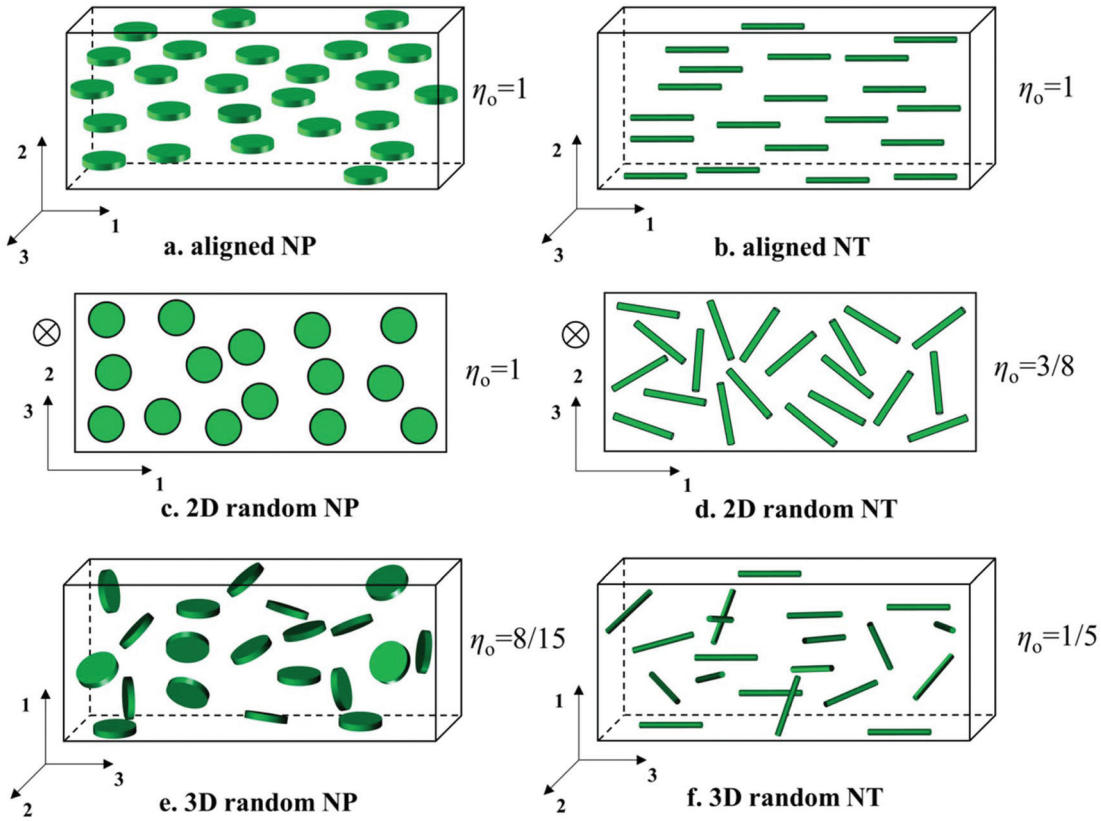

Fig. 12 Schematics of nanoplatelet (NP) and nanotube (NT) nanocomposites with different orientation of the nanofillers: (a and b) aligned, (a, c and d) randomly oriented, in-plane and (e and f) 3D randomly oriented (Adapted from ref. 187).

For the case of CNT-based composites, Omidi *et al.*[189] also modified the classical rule of mixtures, in order to account for the non-linearity in the modulus at higher loadings of CNTs (V_{NT}), in an epoxy-MWCNT composite with filler contents up to 10 wt%. The proposed equation involves several parameters that are crucial for effective reinforcement in CNT-based composites such as an exponential shape function, a length efficiency parameter (κ_l), an orientation factor (κ_o) and a waviness parameter (κ_w). The final form of the modified rule of mixtures proposed by Omidi *et al.*[189] is:

$$E_{C/M} = (\kappa_l \kappa_o \kappa_w E_{NT/M} - 1) V_{NT} e^{aV_{NT}} \quad (12)$$

where $E_{C/M} = (E_C - E_M)/E_M$, $a = \dfrac{\ln \beta}{V_{NT}}$ and $\beta = \dfrac{E_{C/M}}{(\kappa_l \kappa_o \kappa_w E_{NT/M} - 1) V_{NT}}$.

The results from the application of eqn (12) reveal that the fitting is quite good when the waviness parameter (κ_w) is 0.4, showing high degree of waviness, given the fact that for straight nanotubes $\kappa_w = 1$.

The rule of mixtures gives a simple yet reliable estimation of the Young's modulus of composites based on the modulus and volume fraction of each component. It considers the major factors that determine the performance of the composites, which is particularly useful for industrial applications so, during development, major issues can be prioritised.

4.2 Shear-lag analysis

The rule of mixtures was derived originally for continuous fibres, hence some assumptions were made for simplification, such as perfect/elastic interfacial bonding, infinitely long fillers, unidirectional alignment of fillers *etc.*[190] For continuous fibres these assumptions are valid, but when the size of fillers decreases, *e.g.* discontinuous or chopped fibres, modification of those assumption has to be considered. As the interfacial adhesion is related closely to the size of filler, when the filler has a finite size, the stress transfer through interfacial adhesion is reduced. Kelly[191] discussed how stress can be transferred from matrix to fillers with finite length in his book *Strong Solids*, where the interfacial shear stress on the filler is balanced by the axial stress. In this scenario, the deformation of both filler and matrix can be depicted schematically in Fig. 13.

It can be seen that under axial deformation, the filler deforms the most in the central part while deforms the least at the edges, which leads to a high interfacial shear stress at the edges of filler as a result of the large displacement between filler and matrix around filler edge.

This stress distribution can be quantified by using the 'Kelly–Tyson' model,[7] assuming a constant shear stress at the ends of fillers. A more accurate model was proposed by Cox,[6] *i.e.* the 'shear-lag' model, for fibres in paper science which has been widely studied and applied since then.[192] For 1D fibres, it

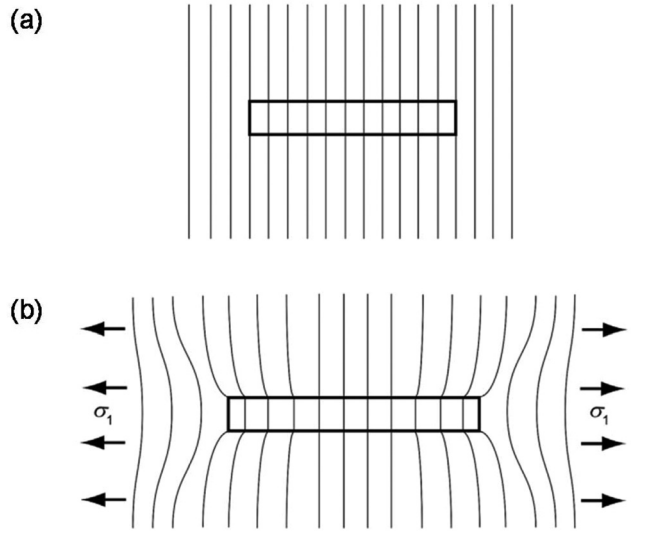

Fig. 13 Single filler with finite size and matrix at the (a) undeformed and (b) deformed state with a tensile stress σ_1. The vertical lines represent the positions perpendicular to the stress.

has the form as below, while detailed discussion of the 'shear-lag' theory can be found elsewhere:[193]

$$\sigma_f = E_{eff} e_m \left[1 - \frac{\cosh(nx/r)}{\cosh(nl/2r)}\right] \quad (13)$$

where

$$n = \sqrt{\frac{2G_m}{E_{eff}} \frac{1}{\ln(R/r)}} \quad (14)$$

In eqn (13), σ_f is the stress on the filler, E_{eff} is the Young's modulus of the filler, and e_m is the strain applied to the matrix. R and r stand for the radius of the representative volume element and the filler, respectively. l is the length of filler in the strain direction, along which the position is defined as x. Although not mathematically rigorous, eqn (13) presents a way of estimating the stress distribution of the filler along the strain direction. Dividing both sides by the modulus of fillers one can obtain the strain distribution as well. On this basis, the shear stress τ_i along the filler can be derived by differentiating eqn (13) to give:

$$\tau_i = \frac{n}{2} E_{eff} e_m \frac{\sinh(nx/r)}{\cosh(nl/2r)} \quad (15)$$

Eqn (15) shows one of the major differences from the Kelly–Tyson model, *i.e.* the non-constant interfacial shear stress. Likewise, for 2D fillers such as graphene, the shear-lag model has been revisited recently and modified as:[5]

$$\sigma_f = E_{eff} e_m \left[1 - \frac{\cosh(nx/t)}{\cosh(nl/2t)}\right] \quad (16)$$

where

$$n = \sqrt{\frac{2G_m}{E_{eff}} \frac{t}{T}} \quad (17)$$

Apart from t and T denoting for the thickness of the 2D filler and the representative volume element, other parameters have the same physical meaning as eqn (17) for a 1D filler. Similarly, the shear stress along a 2D filler can be written as:

$$\tau_i = nE_{eff} e_m \frac{\sinh(nx/t)}{\cosh(nl/2t)} \quad (18)$$

Both the 'Kelly–Tyson model' and the 'Shear-lag model' depict the stress transfer efficiency from matrix to fillers in composites where the strain in fillers starts to build up from the edge and reaches the strain applied to the matrix at a distance from the filler edge (Fig. 14a), and 90% of this distance is defined as the 'critical length-l_c'. The region in the critical length reinforces the composite poorly while the central part delivers an effective reinforcement, in accordance with Fig. 4. The size of l_c has been found to be several hundred μm for fibres[194] and 2–4 μm for graphene,[5] though it can vary with the level of strain even for one system. In order to give an effective reinforcement, it is usually considered that the size of fillers needs to be 10 times of l_c.[5] Fillers with size below this value are still able to provide reinforcement, however with a significantly reduced reinforcement efficiency, especially when the size of filler is comparable to l_c (Fig. 14b).

When the applied strain is over a critical value, fragmentation of the fillers occurs, *e.g.* ~1.0% for fibres.[194] Its strain distribution as found by using the stress/strain sensitive Raman band position shows that strain in each fragmented fibre is very low as a result of the length of the fragments being shorter than or comparable to the critical length of fibres.

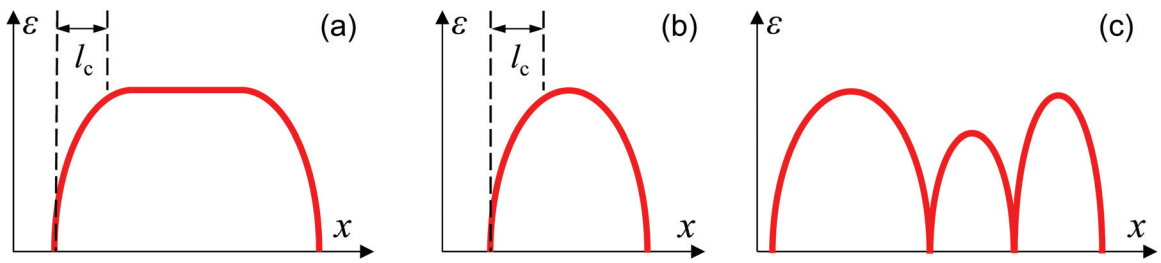

Fig. 14 The strain distribution in a filler (either 1D or 2D) along the strain direction for various filler lengths showing fragmentation as well. (a) Sufficiently long fillers, (b) filler with size comparable to l_c and (c) fragmented filler.

Similar behaviour has been found on graphene which is equivalent to having a significantly reduced 'length factor'.[195]

The discussion above highlights the great importance of the interfacial adhesion in composites as the load is normally applied only to the matrix and not the fillers. Interface modification can be employed to strength the interface, and typical techniques include physical approach (interface roughening) and chemical modification (plasma, functionalisation *etc.*).[196] The levels of interfacial adhesion can be evaluated by using several techniques such as pull-out, push-out, microdroplet and fragmentation test.[197] Regarding the stress/strain distribution of filler, Raman spectroscopy has been demonstrated as a powerful and quantitative tool by simply monitoring the stress/strain sensitive Raman band position[198] and will examined in detail in the next section.

Micromechanical models can be combined to deliver a more accurate and rigorous prediction and estimation of the mechanical properties of composites. For example, the rule of mixtures can be modified by implementing the 'shear-lag' theory with more factors being taken into consideration such as the size and spatial orientation of the fillers. In our previous study we combined the shear lag theory with the modified rule of mixtures in order to understand the mechanisms of reinforcement of polymers from graphene nanoplatelets.[195] Thus, starting from the mean stress along an aligned individual nanoplatelet:

$$\overline{\sigma_f} = \frac{1}{l}\int_{-l/2}^{+l/2} \sigma_f(x)\mathrm{d}x \tag{19}$$

If we substitute x in the shear-lag equation with the aspect ratio of a graphene nanoplatelet (l/t) then the eqn (16) can be rewritten as:

$$\sigma_f(x) = E_{\mathrm{eff}} e_m \left[1 - \frac{\cosh\left(ns\frac{x}{l}\right)}{\cosh\left(\frac{ns}{2}\right)}\right] \tag{20}$$

For uniform strain, after combining eqn (16) and (20) and performing a series of substitutions and Taylor series, the final equation for the modulus of graphene nanoplatelets within a composite is given:

$$E_f \approx \eta_0 \frac{s^2}{12}\frac{t}{T}\frac{E_m}{(1+\nu)} \tag{21}$$

where ν is the Poisson's ratio of the polymer matrix. Substituting this equation back into the rule of mixtures equation with the assumption of $t/T \sim V_f$ we obtain the final equation:

$$E_c \approx E_m\left[1 - V_f + \frac{s^2}{12}\frac{\eta_o}{(1+\nu)}{V_f}^2\right] \tag{22}$$

As can be understood, the value of the E_f (and subsequently of E_c) depends upon the degree of orientation (η_o), the interfacial parameter t/T which is essentially an indication of the strength of the interface and most importantly, of the aspect ratio s of the nanofiller. It is also interesting to notice that on first observation the composite modulus is essentially independent of the filler modulus (at least for soft polymers where E_m < 500 MPa) and depends mostly on the above-mentioned parameters.

Another very important parameter in the use of the shear-lag theory and the subsequent derivation of eqn (21), which explains the mechanism of reinforcement of polymers from graphene-related materials is the interfacial parameter t/T. This parameter depends upon how fast the stress decays into the matrix away from the nanofiller and it is controlled generally by the volume fraction of the filler and the strength of the interface between the filler and the matrix. In a bulk nanocomposite, the t/T ratio is associated strongly with the proximity of neighbouring particles and hence the volume fraction of the filler. Liu *et al.*[199] proposed a mechanical percolation mechanism for the reinforcement of a thermoplastic elastomer by graphene. The authors designed a set of equations for V_f below and above the percolation threshold volume fraction (V_p). Below V_p the reinforcement originates from the inherent ability of individual GNPs to transfer stress effectively (Fig. 15a and b), while above V_p, accelerated stiffening is observed due to the reduction of the distance between adjacent flakes (Fig. 15c and d). The proposed equations are:

$$E_c/E_m = 1 + \left(0.056\eta_o {s_{\mathrm{eff}}}^2 \frac{t}{T} - 1\right)V_f \tag{23}$$

for $V_f < V_p$ and in this case the interfacial parameter equals to V_p and

$$E_c/E_m = 1 - V_f + 0.056\eta_o {s_{\mathrm{eff}}}^2 {V_f}^2 \tag{24}$$

for $V_f \geq V_p$. The three-stage reinforcement model was found to fit the experimental results very well (Fig. 15e).

4.3 Semi-empirical models

In addition, there are also other micromechanical models that one can adopt to predict the Young's modulus of composites, such as Halpin–Tsai model[200] and the Mori–Tanaka model.[201] The Halpin–Tsai model can be shown as below:

$$E_c = E_m\left[\frac{3}{8}\frac{1+\eta_L s V_f}{1-\eta_L V_f} + \frac{5}{8}\frac{1+2\eta_T s V_f}{1-\eta_T V_f}\right] \tag{25}$$

$$E_{\parallel} = E_m\left[\frac{1+\eta_L s V_f}{1-\eta_L V_f}\right] \tag{26}$$

where

$$\eta_L = \frac{E_f/E_m - 1}{E_f/E_m + s}, \quad \eta_T = \frac{E_f/E_m - 1}{E_f/E_m + 2}$$

E_c and $E_{\parallel}$ are the Young's modulus of composite with randomly-oriented and unixially-aligned fillers, respectively. Eqn (25) and (26) can be applied for both the 1D and 2D fillers but it is worth noting that the definition of s is sometimes slightly different.[202,203] The parameter s is generally dependent on both the geometry and the boundary conditions of the reinforcement. Thostenson and Chou[171] modified the equations of Halpin and Tsai by considering s for an aligned short fibre composite to be equal to $s = 2\frac{l}{d} + 40V_f$ and for low

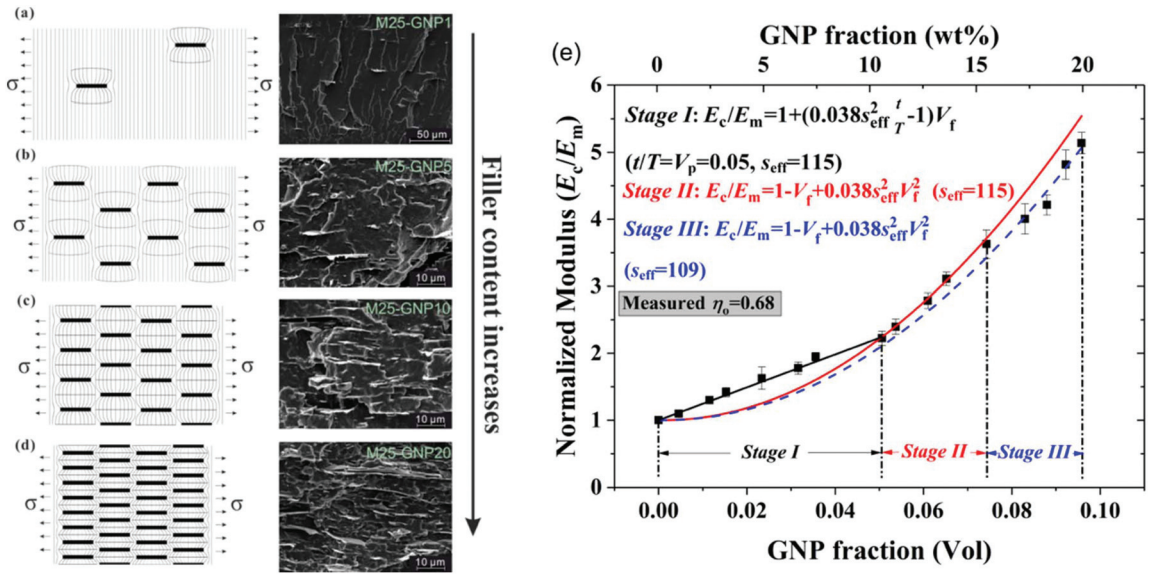

Fig. 15 Schematic illustration of shear lag units at low filler contents (a and b) below the percolation threshold volume fraction V_p and at higher contents (c and d) above V_p. (e) Fittings of normalized modulus against V_f with eqn (23) and (24) for a TPE-GNP nanocomposite.[199]

volume fractions $s = 2\frac{l}{d}$. The authors also showed that the effective fibre modulus is dependent on the nanotube modulus according to the equation: $E_{\text{eff}} = \frac{4t}{d}E_{\text{NT}}$. This approach takes into account that the outer shell of the CNTs carries the majority (if not all) load that is applied, since the bonding between the outer layer and the inner layers was thought to be relatively poor. Thus, when substituting the above equations to the original Halpin–Tsai equation, the final equation that can express the nanocomposite modulus in terms of both the matrix and carbon nanotube properties is:[171]

$$E_{\parallel} = E_{\text{m}}\left[1 + 2\left(\frac{l}{d}\right)\left(\frac{(\text{E}_{\text{NT}}/\text{E}_{\text{m}}) - (d/4t)}{(E_{\text{NT}}/E_{\text{m}}) - (l/2t)}\right)V_{\text{NT}}\right] \times \left[1 - \left(\frac{\text{E}_{\text{NT}}/\text{E}_{\text{m}}) - (d/4t)}{(E_{\text{NT}}/E_{\text{m}}) - (l/2t)}\right)V_{\text{NT}}\right]^{-1} \quad (27)$$

The nanotube diameter must be known for the application of the above equation, as it is very important to the reinforcement efficiency of CNTs, while it should also be noted that eqn (27) is valid only for $l > d > 4t$.

The excellent work of Liu and Brinson[187] has clearly identified that the amount of interface in carbon nanotube-based composites, compared to nanoplatelet-based composites (assuming perfect dispersion and equal ability for polymer-filler interactions), is significantly larger. Thus, the mechanical reinforcing efficiency of nanotubes is higher than that of nanoplatelets of the same aspect ratio, for longitudinal properties of the aligned composites. Given the fact that for commercially-available CNTs and GRMs, the aspect ratio of GRMs is significantly lower than CNTs, the later are expected to perform better towards modulus reinforcement, when oriented along the tensile axis.

4.4 Other factors

From the micromechanical models discussed above, it can be seen that the size and spatial orientation of fillers play significant roles in determining the Young's modulus of composites, hence their quantification is of paramount value. However, it is worth pointing out that other factors are also influential. In particular, the waviness and wrinkling induced during manufacturing especially for fillers at nano- or micro-scale. They are thought to be the reason why the experimental values are lower than the ones predicted from theoretical models. Furthermore, agglomeration is another reason that many studies in the literature have used to interpret the deviation between the measured and estimated Young's modulus of composites. Due to their different scale and hence much large surface area than macroscale fibres, nanofillers are prone to agglomerate. Although practically difficult, attempts have been made to use models to predict the effect of agglomeration on the mechanical properties of composites.[204]

5. Analysis of GRM- and CNT-based composites using Raman spectroscopy

Raman spectroscopy is a non-destructive experimental technique that can be used to characterise in detail all sp^2 carbons from zero to three dimensions such as fullerenes (0D),[205,206] carbon nanotubes (1D),[207] graphene (2D)[208] and graphite (3D).[209] The physical properties of sp^2 carbons that are corre-

lated to electrons and phonons can be obtained through Raman spectroscopy, along with unique crystallographic and vibrational information.[210] The usefulness of Raman spectroscopy in the study of sp^2 carbons lies in the combination of the Raman process with optical absorption to (or emission from) an excited state; in this case the Raman intensity signal can be enhanced by several orders of magnitude by resonance.[211] The specific effect is the reason why the one-atom-thick graphene can provide a strong and well-defined Raman signal or why individual single walled carbon nanotubes can be clearly identified. In this review, we will focus on the Raman spectroscopy of carbon-based nanocomposites and the information we can obtain through the application of this technique, since the use of Raman for the study of graphene or carbon nanotubes has been well documented and presented in detail in a number of highly-cited reports.[212–215]

5.1 GRM-based nanocomposites

As in the case of carbon fibres or carbon nanotubes, Raman spectroscopy has been employed extensively for the study of the micromechanics of reinforcement by graphene-related materials (GRMs) in nanocomposites. The strong resonant Raman scattering, even from a one-atom-thick graphene flake, produces a well-defined Raman signal and enables the observation of a number of very interesting phenomena under various conditions (Fig. 16). One of the parameters that enhance the usefulness of Raman spectroscopy in the study of GRMs is the fact that pronounced differences can be observed between flakes with a different number of layers. For the case of monolayer graphene, the intensity of the characteristic 2D (or G') (~2690 cm^{-1}) band is twice the intensity of the G band (~ 1580 cm^{-1}), while in the case of bilayer graphene flakes, the 2D band is comparable or even weaker than the G band. Furthermore, a change of shape can be seen due to the resonance effects in the electronic structure of the two-layer material, while also a shift of the 2D band towards higher wavenumbers can be observed for bilayer graphene.[216] With increasing number of layers the 2D band shifts to even higher wavenumbers and more asymmetric/broader shape, while for more than 5 layers, the signal resembles the one of graphite. The defect-induced D band, which is usually found in different forms of graphitic carbon is most commonly observed in the case of imperfect graphene prepared by methods such as chemical vapour deposition (CVD) and thermal expansion, while it is very prominent in graphene oxide as a result of defects, vacancies and distortions induced during oxidation.

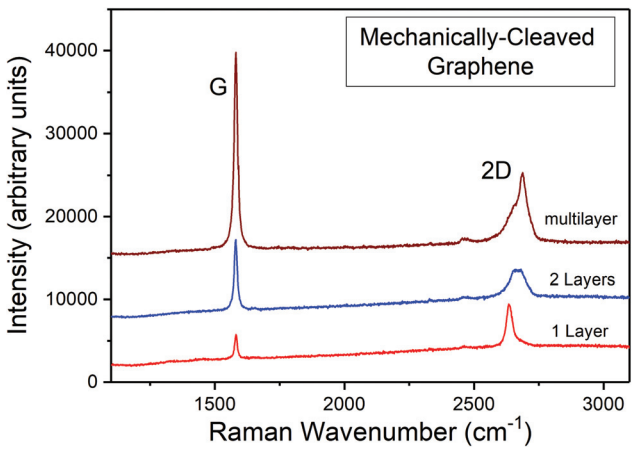

Fig. 16 Raman spectra of graphene showing the difference in spectra between monolayer, bilayer and multilayer samples.[198]

Raman spectroscopy can be used for the detailed study of both free-standing graphene-related materials, graphene deposited on a flexible substrate or graphene-filled polymer nanocomposites. For this reason, this section will be divided into two parts: the investigation of the mechanical properties of (i) graphene flakes on a substrate and (ii) graphene-based polymer nanocomposites and "model" nanocomposites.

5.1.1 Graphene flakes deposited on a substrate. The deformation of monolayer graphene deposited on a flexible substrate leads to significant bond stretching and lattice distortion, which can be realised through the downshift of the characteristic 2D band. The work of Mohiuddin *et al.*[217] first identified correctly that for the monolayer, the characteristic downshift of the 2D band is in the order of -60 ± 5 cm^{-1} $\%^{-1}$ strain, after uniaxial bending, consistent with the material having a modulus in the order of 1 TPa. This value was further confirmed in several studies from different research groups. It is generally considered in the literature as the reference value for the redshift of the Raman 2D band of graphene under tensile strain and can be used as the calibration value for the evaluation of strain within monolayer graphene. The authors reported the splitting of the G peak into the G^+ and G^- peaks (similar splitting takes place in CNTs due to curvature), while the 2D and 2D′ bands did not split at low strain levels. The red shift calculated for the G^+ band was -10.8 cm^{-1} $\%^{-1}$ strain and for the G-band was -31.7 cm^{-1} $\%^{-1}$ strain, approximately half of the 2D band. It is known that the G^+ band is polarized perpendicular to the strain axis, while G^- is polarized along the strain axis and the difference in the downshift of these two bands originate from their eigenvector orientations. The authors also calculated the Grüneisen parameter for the first time by using the equation:

$$\gamma_m = -\frac{1}{\omega_m^0}\frac{\partial \omega_m^h}{\partial \varepsilon_h} \quad (28)$$

where $\varepsilon_h = \varepsilon_{II} + \varepsilon_{tt}$ is the hydrostatic component of the strain and l and t refer to the parallel and perpendicular directions of the strain, while ω_m^0 and ω_m^h correspond to the frequency of the phonons of peak m at zero strain.

After a series of substitutions and transformations the final form of the Grüneisen parameter for the graphene bands takes the form:

$$\gamma_{D,2D}^{uniax} = -\frac{\Delta\omega_{D,2D}}{\omega_{D,2D}^0(\varepsilon_{ll} + \varepsilon_{tt})} \quad (29)$$

The Grüneisen parameters obtained were $\gamma_G = 1.99$, $\gamma_{D'} = 1.61$, $\gamma_D = 3.55$ and $\beta_G = 0.99$. Galiotis and coworkers[218] further confirmed the original findings of Mohiuddin *et al.*[219] when

they deformed monolayer graphene flakes under tension and compression. The high flexibility of graphene was revealed by the buckling of the material at about 0.7% strain. Also, the $\partial\omega/\partial\varepsilon$ was reduced from +25 cm^{-1} $\%^{-1}$ strain to zero at ~0.7 strain, indicating the presence of residual strain. It should be noted that in the case of nanocomposites, the rate of decrease should be smaller, as simply deposited and uncoated flakes are more prone to detachment under compressive forces.

Polyzos *et al.*[220] managed to suspend monolayer flakes for the evaluation of the "true" uniaxial deformation. This was achieved by sandwiching the monolayer flake between two PMMA layers and by suspending its central part by the removal of a section of PMMA with e-beam lithography. The authors reported on the splitting of both G and 2D bands of graphene and the results of the G band were in accordance with the ones obtained by Mohiuddin *et al.*[219] for graphene suspended in air (Fig. 17a and b). On the other hand, the reported strain sensitivities of −84 cm^{-1} $\%^{-1}$ strain for the $2D_1$ and −94 cm^{-1} $\%^{-1}$ strain for the $2D_2$ components of the 2D peak are the largest values of phonon shifts reported for uniaxial deformation (Fig. 17c and d). This study reveals the difficulties in the application of uniaxial strain in 2D materials deposited on a flexible substrate and proposes a good practice for the manipulation of graphene on the nanoscale and the implementation of experimental mechanical measurements.

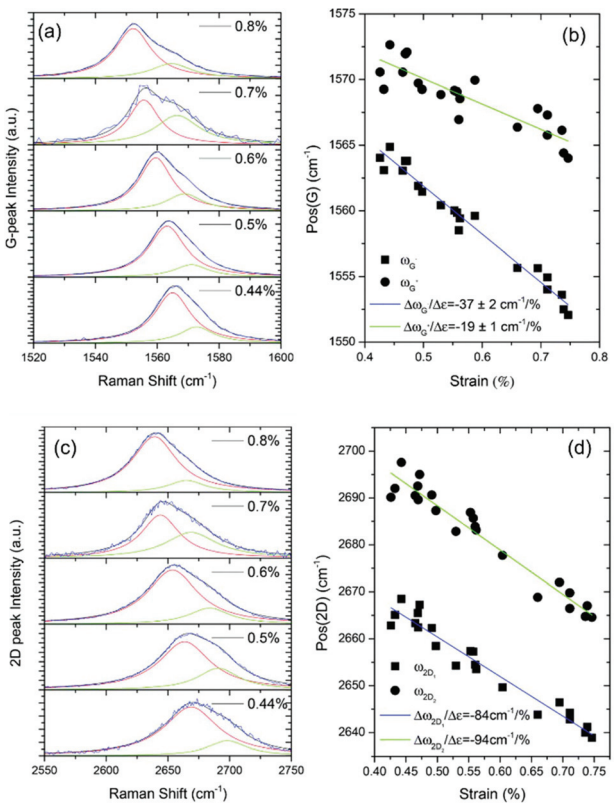

Fig. 17 (a) The G-peak of a suspended monolayer graphene flake at various strain levels; the splitting of the G^- and G^+ components are clearly seen. Each strain level corresponds to a different lateral position across graphene. (b) The two components of G peak (G^- and G^+) and the respective downshift of the G peak as a function of strain. The straight lines are least-squares-fitted to the experimental data. (c) The 2D-peak of suspended monolayer graphene in air at various strain levels (d) 2D sub-peaks as a function of strain. The straight lines in figures (b) and (d) are least-squares-fitted to the experimental data (Reproduced from ref. 220 with permission from The Royal Society of Chemistry).

In addition to monolayer graphene, the investigation of graphene with a larger number of layers is of utmost importance for practical applications, since the inherent properties and behaviour of few- and many-layer graphene should be identified, as they will be used mostly for the fabrication of bulk nanocomposites. Gong *et al.*[221] undertook a study on the effect of the number of layers on the downshift of the characteristic Raman bands and it was found that there is a decrease in the band shift rate with increasing layer number (Fig. 18a). Monolayer and bilayer graphene display almost the same redshift rate, while from that point on the shift of the 2D band decreases as a result of weak van der Waals forces between the layers and lower internal stress transfer. Additionally, the G band of trilayer graphene was reported to split into the G^- and G^+ components at higher strains in tension (Fig. 18b), while as expected, in compression, both Raman peaks (G and 2D) blueshift up to a critical compressive strain (Fig. 18c and d).[222]

The trilayer graphene possesses a higher bending rigidity compared to the monolayer, however it has been reported that its critical strain is 4 times smaller than the one found in single layer graphene. Since earlier studies established that shear at the graphene-substrate interface is the mechanism of stress transfer, Anagnostopoulos *et al.*[223] investigated the effect of the edges of graphene upon axial stress transfer by Raman mapping near the edges of a monolayer that was supported onto a SU-8/PMMA matrix. The authors revealed that the presence of unintentional doping, residual stresses (from the preparation procedure) and/or edge defects lead to a deviation from the classic shear-lag prediction for a region of ~2 μm from the edge. This should be taken into account, especially in studies where mapping of graphene flakes is performed by Raman spectroscopy and the experimental results of stress *versus* position are (commonly) fitted with the shear-lag equation.

Raman spectroscopy can be also applied for monitoring the response of the G band of monolayer graphene in relation to the response of carbon fibres to the application of strain.[224] A universal value of average phonon shift rate with axial stress has been proposed to be $-5\omega_0^{-1}$ (cm^{-1} MPa^{-1}) where ω_0 is the G peak position at zero stress for both graphene and carbon fibres with an annular morphology. Another very important aspect of this work was the construction of a universal plot for the downshift of the G band that enables the quantification of the shift for all graphitic materials (Fig. 19).

Chemical functionalization is considered to be one of the most prominent methods for the improvement of the interactions between a nanomaterial and a polymer. In this context, Zhang and coworkers[227] functionalized monolayer graphene deposited onto a PMMA beam in order to improve the

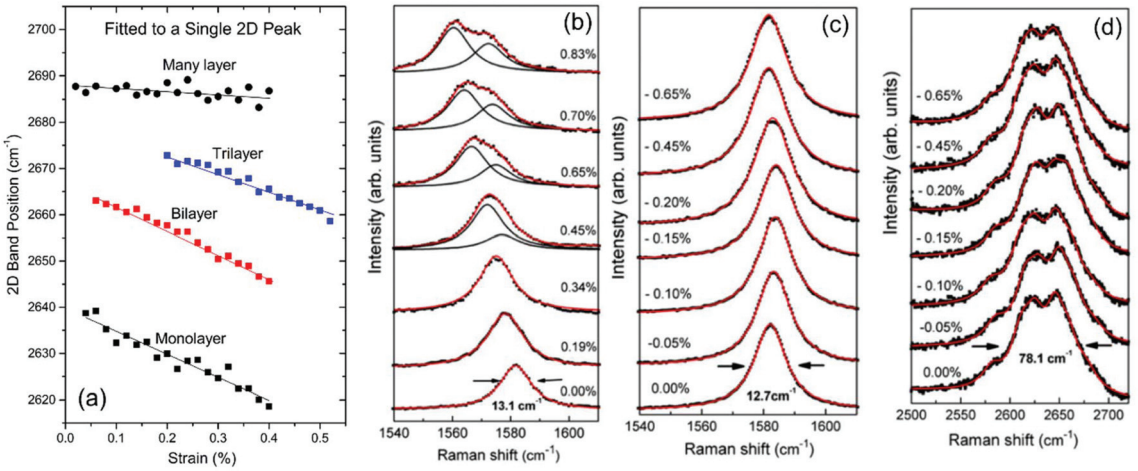

Fig. 18 Shifts with strain of the 2D band for adjacent monolayer, bilayer, and trilayers regions on a graphene flake showing monolayer, bilayer and trilayer regions, along with the shift with strain for the 2D band of a multilayer flake (all 2D bands were force fitted to a single Lorentzian peak)[221] (Copyright 2012 by the American Chemical Society). (b) Evolution of the G Raman peak under uniaxial tensile strain in a trilayer part of a flake displaying regions with different thickness. The evolution of (c) G and (d) 2D Raman peaks under uniaxial compression for a trilayer flake.[222]

interactions between the two materials. The authors utilized an O_3/H_2O gaseous mixture in order to oxidize the monolayer under a controlled functionalization procedure. The strain distribution (ε_g) can be plotted as a function the position (x) along the length direction based on the shear lag model (eqn (16)). As mentioned earlier, the shear-lag equation suggests that the strain is maximized at the centre of the flake ($x = 0$) and the maximum interfacial shear stress occurs at the edges ($x = \pm L/2$). From Fig. 20a it can be seen that eqn (16) fits well the experimental results at low strains, while beyond the critical sliding strain (ε_c) it is not able to predict the strain distribution as a result of interfacial sliding at the edges.

The results revealed that the stress transfer is more effective for functionalized monolayers (Fig. 20b), leading to enhanced mechanical properties due to the formation of hydrogen bonds at the interface. The interfacial shear strength (τ_c) was also derived based on the linear slope of the strain distribution according to:

$$\tau_c = E_{gra} t \frac{d\varepsilon}{dx} \approx E_{gra} t \frac{\varepsilon_p}{L/2} \quad (30)$$

where E_{gra} is the modulus of monolayer graphene (1 TPa), t = 0.35 nm and $d\varepsilon/dx$ is the slope of gradient in sliding zones. Importantly, the τ_c values for functionalized graphene (≈1.7 MPa) were almost four times higher than that of monolayer graphene, indicating the effectiveness of functionalization on the formation of a stronger filler/matrix interface. Another interesting observation from this excellent study is the effect of excessive O-containing groups under high degrees of functionalization, which create a high number of defects and induce crack initiation and propagation under tension. Therefore, a balance should be kept regarding the amount of functional groups in graphene for efficient mechanical reinforcement.

The majority of publications dealing with of strain in graphene and the *in situ* evaluation of the Raman spectra follow the uniaxial deformation of graphene-related materials. The application of biaxial strain and the study of the Raman spectra is also of utmost importance as this procedure is highly related to the performance of graphene in thin films, membranes and pressure sensors. A few studies have made an attempt to evaluate the behaviour of 2D materials under biaxial strain. Casiraghi and coworkers[228] created graphene bubbles (or balloons) where monolayer and bilayer graphene was strained biaxially. The Grüneisen parameter was obtained and was in agreement with the report of Mohiuddin, while the small strain (~1.2%) did not affect the stacking configuration. It was also reported that doping and strain caused by the interactions of graphene with the substrate, can also affect the Grüneisen parameters and these are the most important reasons why there are variations in the literature regarding the Grüneisen parameters of graphene. For example, in the work of Ding *et al.*,[229] piezoelectric actuators were used for the application of biaxial strain but the Grüneisen parameters of the D and 2D bands were different than the ones obtained from Casiraghi and coworkers[228] (γ_D = 2.3 and γ_{2D} = 2.98). In a manner similar to the previous study, Lee *et al.* applied pressure to graphene suspended over round holes and measured the strain after inducing a bulging of the samples, similar to balloons. The Grüneisen parameter were taken to be equal to $\gamma = 2.2 \pm 0.1$ and the shear deformation potential was taken equal to $\beta = 0.93 \pm 0.04$; thus, the strain was calculated by: $\Delta\omega_b = -2\omega_0\gamma\varepsilon_b$, where ω_0 is the frequency of unstrained graphene and ε_b is the biaxial strain. The G peak shift was in the order of -13 cm^{-1} %$^{-1}$ strain, while the biaxial modulus of monolayer graphene was equal to 2.4 ± 0.4 TPa, while for bilayer was equal to 2.0 ± 0.5 TPa. It should be noted that these values might be slightly higher than the usual values of

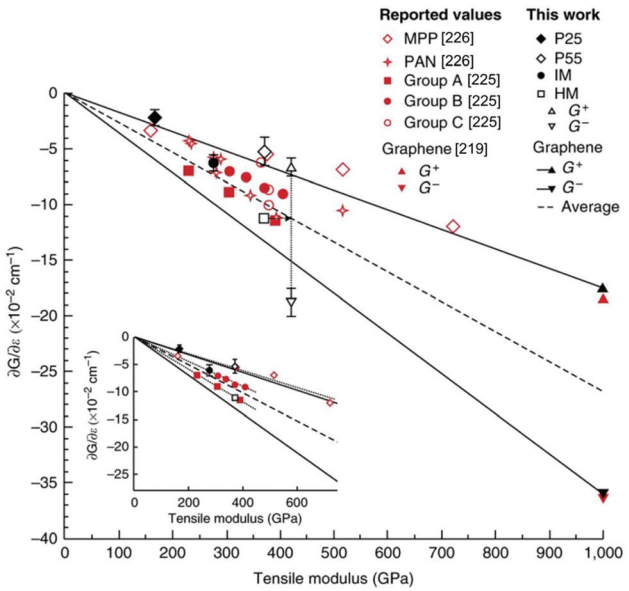

Fig. 19 The characteristic downshift of the G band of graphene and carbon fibres *versus* the tensile modulus of the respective materials. The black solid and dashed lines correspond to fits to experimental data for graphene. The graphene G sub-bands values measured in this study and in ref. 219, are represented by black and red triangles, respectively. Also, from ref. 225 where a number of different types of fibres were studied, in red, the solid square points correspond to group A fibres, the solid circles correspond to group B, the open circles to group C, whereas the diamonds to MPP-CFs and the stars to various PAN-CFs from the work of Huang and Young.[226] In black, data points for high modulus (HM) (open square), intermediate modulus (IM – full circle), P25 (full diamond) and P55 (open diamond) CFs measured in this work.[224] The high modulus carbon fibre G band splitting and its projection onto the graphene average line are represented by the black open triangles. The inset shows the $\partial\omega_G/\partial\sigma$ least-squares line fits for group A ($\partial\omega_G/\partial\sigma$ = 3 cm^{-1} GPa^{-1}), B (2.3 cm^{-1} GPa^{-1}) and MPP-CFs (1.5 cm^{-1} GPa^{-1}) as dotted lines. The other symbols in the inset have the same meaning as in the main plot. The error bars represent the standard deviation from all measurements on the given fibre[224] (Copyright 2011, Springer Nature Publishing Group).

the biaxial modulus of graphene, as the authors managed to apply a maximum strain of only 0.19%, while higher strains lead to softening of the material and a subsequent reduction of the modulus.

Androulidakis *et al.* utilized a cross-type shaped apparatus for the application of biaxial strain where the as 2D materials are deposited on the centre of the cross.[230] The authors subjected a number of graphene related materials to controlled biaxial deformation and the mean values of $\partial\omega_{2D}/\partial\varepsilon$ and $\partial\omega_G/\partial\varepsilon$ for a monolayer graphene membrane were found to be equal to −148 ± 6 cm^{-1} $\%^{-1}$ strain and −62.3 ± 5 cm^{-1} $\%^{-1}$ strain respectively. Similar to the results from the application of uniaxial strain, bilayer graphene showed very similar shifts to monolayer graphene, while the increasing layer number led to a reduction of the shift rates as a result of cohesive failure within the flakes. Finally, Metzger *et al.*[231] investigated graphene membranes that were deposited over a patterned substrate with shallow depressions. The authors observed that the membranes did not remain free-standing but adhered to the substrate despite the biaxial strain. The Grüneisen parameters obtained were close to the ones of Mohiuddin, while the downshift of the 2D band was slightly higher than the values reported by Androulidakis, of the order of 203 ± 20 cm^{-1} $\%^{-1}$ strain.

Most of the investigations discussed earlier were undertaken upon the deformation characteristics of flat graphene, but the case of wrinkled graphene presents a lot of interest as the majority of the graphene nanoplatelets that are commonly used as reinforcements in polymer composites display wrinkles and folds that reduce the reinforcing efficiency. Li *et al.*[232] deposited CVD graphene on a poly(ethylene terephthalate) substrate and followed the uniaxial deformation mechanics of wrinkled graphene by Raman spectroscopy. It was found that the wrinkles separated the flat graphene into isolated islands with a size of ~1 μm and the downshift of the 2D band was in the order of −12.8 cm^{-1} $\%^{-1}$ strain, less than 25% of the refer-

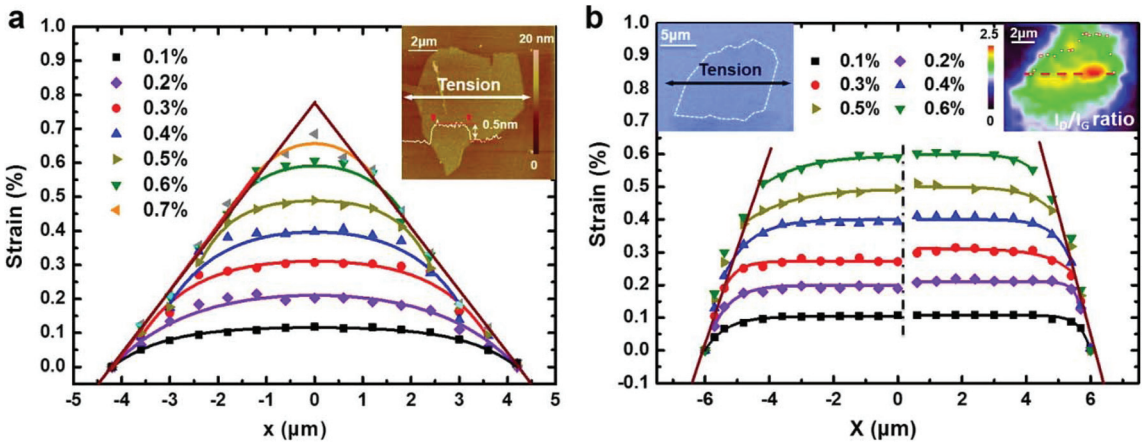

Fig. 20 The strain distribution across the tensile axis of (a) a monolayer, pristine graphene and (b) oxidized graphene, at different strain levels. The inset in (a) shows the AFM image of the monolayer, while in (b, left panel) the optical image of the monolayer graphene and (b, right panel) the corresponding Raman contour map of I_D/I_G of the specific flake. The solid lines represent the fits based on the nonlinear shear-lag model (Reprinted (adapted) with permission from ref. 227. Copyright 2016 American Chemical Society).

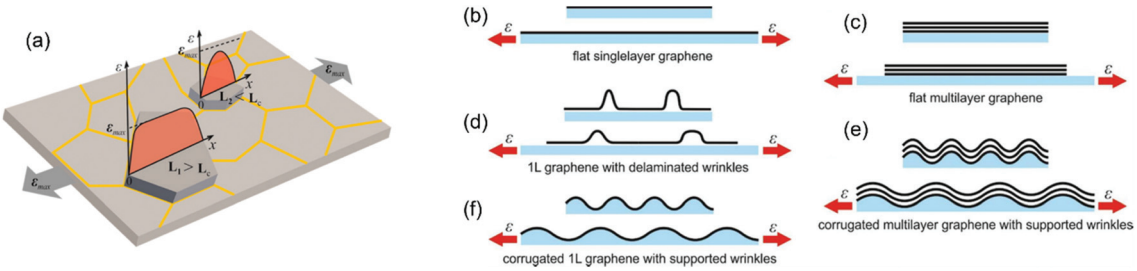

Fig. 21 Schematic diagram (a) explaining the proposed stress transfer mechanism in wrinkled CVD graphene (l_i is the length of the *i*-crystallite and l_c the critical transfer length) (Reprinted (adapted) with permission from ref. 232. Copyright 2015 American Chemical Society). Schematic of the morphology and qualitative stress transfer of a flat (b) mono- and (c) few-layer graphene, (d) wrinkled CVD graphene on polymer, and wrinkled (e) few- and (f) monolayer graphene (Reprinted (adapted) with permission from ref. 86. Copyright 2017 American Chemical Society).

ence 2D band shift rate of ~ −60 cm^{-1} $\%^{-1}$ strain (Fig. 21a). It should be noted though that the wrinkles examined in this case have little to do with the performance of wrinkled material in bulk composites, as the stress transfer length (1.2 μm) is probably lower than the critical length and this can explain the low shift rates. Moreover, this work deals with wrinkles constrained from flat graphene areas, a compression of 2–3% is developed upon cooling from ~ 1000 °C, which leads to the formation of wrinkles, but such CVD material is highly unlikely to be used in composites.

Anagnostopoulos *et al.*[233] developed a similar CVD graphene/epoxy system and the redshift of the 2D band displayed a rate of ~−18 cm^{-1} $\%^{-1}$ strain up to 1.4% strain, that is less than 30% than the one expected for a flat monolayer graphene. As shown in a study[234] the group of Galiotis managed to create similar mosaic patterns to those observed in CVD graphene by means of lateral wrinkling induced by tension and Euler buckling resulting from uniaxial compression upon unloading. The same group has also provided evidence[86] that the "corrugation" of flat graphene enhances the load bearing capability of few-layer graphene, as compared to flat specimen (Fig. 21b–e). The authors commented that the interfacial shear stress between the graphene and the polymer increased due to wrinkling and the downshift of the characteristic 2D band was in the order of −57 cm^{-1} $\%^{-1}$ strain for both monolayer, bilayer and trilayer graphene (Table 1). This was unexpected since it is known that for increasing layer number, the interlayer coupling cannot transfer the load efficiently. The exceptional performance of the wrinkled material was attributed to the small amplitude wrinkled morphology due to the enhanced shear strength of the interface. It should be noted at this point that the definition of wrinkling is very broad thus its effect is difficult to quantify. Finally, in a very recent study, Li *et al.*[235] came up with an analytical equation to quantity the effect of different types of wrinkles and folds on graphene, after applying strain engineering to wrinkled and folded graphene. It was found that wrinkles do not reduce the reinforcement efficiency significantly when majority of graphene still conforms to substrate, while when graphene detaches from substrate its efficiency drops significantly as a result of delamination.

Table 1 Shift rates for simply supported graphene with thickness of one to three layers under tension for the 2D and G Raman peaks (Reprinted (adapted) with permission from ref. 86. Copyright 2017 American Chemical Society)

	Thickness (no. of layers)	∂Pos (2D)/$\partial\varepsilon$ (cm^{-1} $\%^{-1}$)	∂Pos (G^+)/$\partial\varepsilon$ (cm^{-1} $\%^{-1}$)	∂Pos (G^-)/$\partial\varepsilon$ (cm^{-1} $\%^{-1}$)
Wrinkled flakes	1	−57.4 ± 3.0	−9.7 ± 0.8	−29.6 ± 1.1
	2	−57.1 ± 1.5	−11.4 ± 1.5	−28.2 ± 1.3
	3	−57.1 ± 2.8	−12.7 ± 1.1	−29.8 ± 1.0
≪Flat≫ flakes	2	−48.6 ± 2.5	−11.6 ± 0.7	−27.9 ± 1.0
	3	−28.6 ± 1.4	−6.5 ± 1.8	−18.3 ± 1.2

Another material that presents a highly-wrinkled, 2D morphology is graphene oxide (GO). Generally, the study of the application of strain to GO and the *in situ* Raman measurements presents a number of challenges due to the presence of the functional groups that damage the graphene lattice and give rise to the defect-activated 2D band. In addition, GO is also vulnerable to damage from the laser beam as thermal- or photo-reduction of the material can take place. Additionally, the absence of the strain-sensitive 2D band is another limiting factor for the study of GO with Raman. Young and coworkers analysed the deformation micromechanics of GO by strain engineering.[236] Interestingly, the results showed that the number of GO layers does not affect the reinforcement efficiency of GO; this effect is possibly associated with the enhanced interlayer adhesion GO due to the functionalisation, which is already too large even for few-layer GO and as a consequence the interlayer stress transfer is not effective. Moreover, the degree of layer exfoliation is not expected to play any role on the mechanical reinforcement in GO-based nanocomposites. The application of strain (up to 1%) led to a downshift of the D band in the order of −14.9 cm^{-1} $\%^{-1}$ strain. Interestingly, when the authors mapped the strain distribution in a GO flake, the strain profile remained constant along the flake, which is in contrast to what is observed for monolayer graphene, where the strain increases from the edges and remains constant only at the centre of the flake, in accordance with the expectation from the shear-lag theory. This observation, along with the poor resolution of the GO edges under the microscope and the spatial resolution of Raman spectro-

meter (1–2 μm) do not allow the determination of the critical length for reinforcement, making the classical shear-lag theory not applicable for this specific material.

5.2.2 "Model" graphene nanocomposites. In addition to its practicality for the characterization of individual, free-standing graphene flakes, Raman spectroscopy has also been applied with great success to follow the molecular deformation of graphene within polymer nanocomposites, through the study of the stress-induced Raman band shifts. As mentioned in the previous section, the slope of -60 ± 5 cm^{-1} %$^{-1}$ strain for the 2D band has been observed in a number of early experimental studies[218,219] for free-standing graphene; thus, it can be used as a calibration value for the determination of stress or strain distribution in graphene nanoplatelets in nanocomposites. The work of Gong *et al.*[5] showed that Raman spectroscopy can be used in order to monitor the stress transfer in a "model" composite, consisting of a PMMA beam as the substrate, a thin layer of SU-8 epoxy-based negative photoresist where monolayer graphene was deposited and the structure was then spin-coated with a thin layer of PMMA (50 nm). The authors observed the characteristic downshift of the 2D band up to 0.4% strain, while from that point on the band shifts became irregular, as a result of relaxation of the specimen and possible damage of the polymer/graphene interface. The unloading procedure revealed that the 2D band position was at a higher wavenumber than before loading, suggesting that graphene underwent slippage in the composites and then was subjected to in-plane compression. The process that was well-established for the strain mapping along carbon fibres was also adopted for the graphene monolayer in this work at 0.4% and 0.6% strain. The results revealed once again that the strain builds up from the edges towards the centre of the flake and the behaviour was analysed with the shear lag theory, which assumes that there is elastic stress transfer from the matrix to the filler through shear at the filler-matrix interface (eqn (16) and (18)).

The product *ns* depends on both the degree of interaction of the graphene flake with the matrix and the morphology of the flake and of the strain mapping at 0.4% strain it was found to be equal to 20, showing that the behaviour could be modelled. Furthermore, the critical length (l_c) for the evaluation of the quality of reinforcement from graphene flakes was obtained, and according to its definition, it is the product of 2× the distance over which the strain rises from the fibre ends to the plateau. In this case, it is ~3 μm, while it is generally thought that the fibre length in order to obtain good reinforcement should be ~10l_c, revealing that flakes of around 30 μm diameter are needed to reinforce a polymer significantly.

The same group also reported on the use of Raman spectroscopy for mapping the strain in a model nanocomposite consisting of graphene sandwiched between two thin layers of SU-8 and deposited onto a PMMA beam.[237] Once again, the strong resonance from graphene enabled the authors to monitor the stress-induced band shifts and map the strain distribution. The mapping procedure revealed clearly the development of cracks as a result of fragmentation at 0.8% strain (Fig. 22). As this strain is very low for a graphene monolayer to undergo fragmentation, it is quite possible that cracking took place only in the SU-8 coatings. Moreover, the authors showed that the interfacial shear stress (IFSS) in the fragments was only ~0.25 MPa, an order of magnitude lower than the IFSS before fragmentation. A further study of model nanocomposites where graphene was deposited onto a PMMA beam and then coated with an epoxy resin, revealed that the rate of band shift per unit strain for monolayer graphene is independent of whether the coating exists or not[221] (Fig. 23a). On the other hand, for the case of bilayer graphene, the poor stress transfer between the graphene layers led to a lower rate of band shift for the uncoated specimen (Fig. 23b). For bulk composites, this means that bilayer graphene is equally effective for mechanical reinforcement, to monolayer graphene, while only 15% of the efficiency is lost with trilayer graphene, while according to the authors for more than 7 layers of graphene, the reinforcing efficiency drops to half that of monolayer graphene.

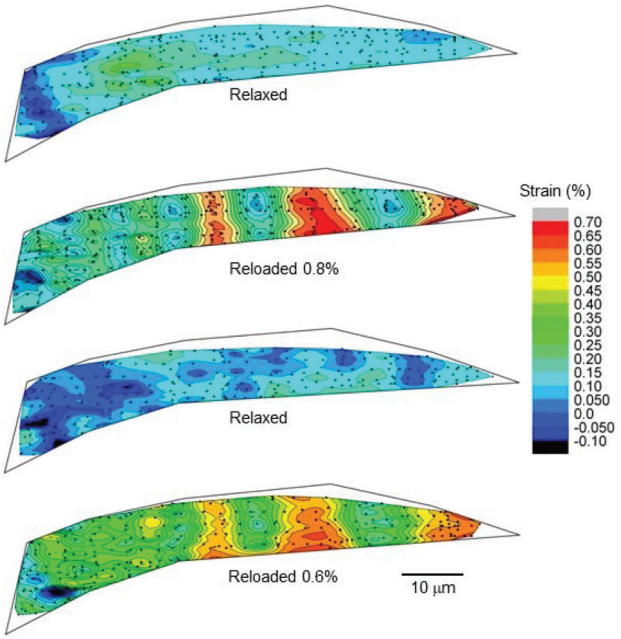

Fig. 22 Strain contour mapping through Raman spectroscopy over the coated graphene monolayer in the relaxed states and reloaded to 0.8% and 0.6% strain (Reprinted (adapted) with permission from ref. 237. Copyright 2011 American Chemical Society).

In a recent, interesting study of Eichorn and coworkers, the authors created a model bilayer graphene/nanocellulose composite and studied the deformation behaviour by applying strain.[238] A quite high stress transfer efficiency of 66% was derived at the cellulose/graphene interface, while the splitting of the G band enabled the calculation of shear strain in the graphene. Moreover, the stress uptake and the compression buckling strain in model graphene monolayer nanocomposites was evaluated by Frank *et al.* by monitoring the shift of the G or 2D Raman bands.[239] The compression strain led to a decrease in the values of $\partial\omega_{G,2D}/\partial\varepsilon$ up to a point where the slope started to increase, indicative of progressive buckling which leads to the collapse of the flakes. The critical buckling

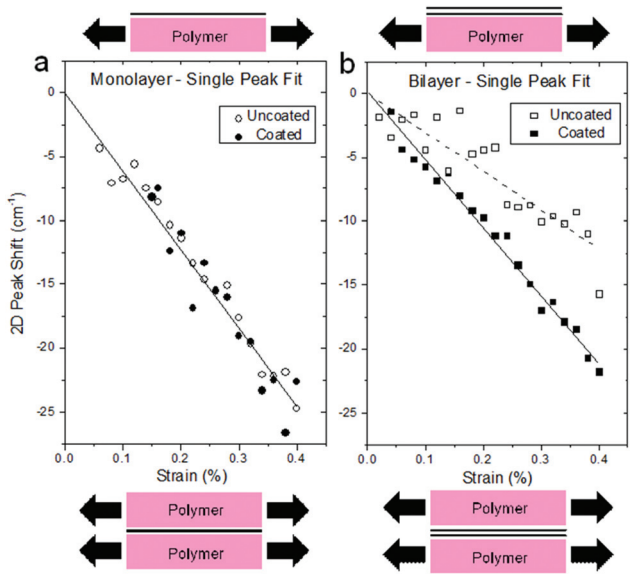

Fig. 23 Downshift of the 2D Raman band of graphene during deformation upon the PMMA beam (laser excitation 633 nm). (a) A monolayer graphene flake deformed before and after coating with SU-8 epoxy-based negative photoresist. (b) A graphene bilayer deformed before and after coating with SU-8. (Schematic diagrams of the deformation of the uncoated (above) and coated (below) graphene are also included). (Reprinted (adapted) with permission from ref. 221. Copyright 2012 American Chemical Society).

strain, as expected, depends on the size of the flakes and their geometrical characteristics.

5.2.3 Bulk graphene nanocomposites. Given that the stress transfer from the matrix to a fibre can be followed very effectively through the use of Raman spectroscopy, the Young's modulus of carbon-based materials (E_R) can be estimated from the slope of the plots of the 2D (or D) Raman band position against strain. For graphene-related materials, where the characteristic downshift of the 2D band is in the order of: $(\partial\omega_{2D}/\partial e)_{(ref)} = -60$ cm^{-1} %$^{-1}$ strain the E_R can be estimated from the relationship:

$$E_R = \frac{\partial\omega_{2D}}{\partial e}\frac{E_{gra}}{(\partial\omega_{2D}/\partial e)_{(ref)}}(\text{GPa}) \quad (31)$$

where $\partial\omega_{2D}/\partial e$ is determined for the 2D band in cm^{-1} %$^{-1}$ strain and E_{gra} is the modulus of graphene (E_{gra} = 1050 GPa). The above equation can be adjusted for the case of the D band, where $(\partial\omega_D/\partial e)_{(ref)} = -30$ cm^{-1} %$^{-1}$. The shear-lag theory can be also modified to include this equation and takes the form:

$$E_R = \eta_o E_{eff}\left[1 - \frac{1}{\cosh\left(\frac{ns}{2}\right)}\right] \quad (32)$$

and the final equation for flexible matrices is:

$$E_R \approx \eta_o \frac{s^2}{8}\frac{t}{T}\frac{E_m}{(1+\nu)} \quad (33)$$

The application of both equations E_f and E_R in the study of Liu *et al.*[55] enabled the effective aspect ratio of the graphene nanoplatelets in bulk nanocomposites to be quantified, while as was expected the modulus from Raman spectroscopy was higher than that obtained from the tensile measurements. This comes as a result of the application of Raman spectroscopy to flakes that are axially aligned to the surface of the sample (so that η_o = 1), while the GNPs were partially aligned in the bulk composites. In the same study it is also clearly shown that the effective aspect ratio (s_{eff}) is pronouncedly reduced with increased filler loading due to agglomeration between graphene nanoplatelets.

5.2 CNT-based composites

The combination of the versatility of Raman spectroscopy along with the strong resonance from carbon nanotubes[8] can provide a wealth of information regarding the effect of CNTs in polymer nanocomposites. A number of research investigations have applied Raman for the evaluation of the nanotube-polymer interactions, the dispersion characteristics, the orientation of nanotubes and the response of CNTs during the application of strain by following the Raman band shifts or the peak width changes.

5.2.1 Characterization. The Raman spectrum of SWCNTs displays the following characteristic features: radial breathing modes at low frequencies (<400 cm^{-1}) corresponding to the movement of carbon atoms towards the radial direction, the double-resonant, disorder induced D band (~1350 cm^{-1}), the G band (~ 1600 cm^{-1}) resulting from the in-plane vibrations of the sp^2 C–C bonds and the 2D (G') band (2500–2700 cm^{-1}) that is an overtone of the D band.[240] It should be noted that the Raman spectrum of MWCNTs differs from that for SWNTs and it resembles closely that of carbon fibres. The sharp peak at ~ 1582 cm^{-1} corresponds to one of the E_{2g} modes, while the D band at 1334 cm^{-1} is attributed to the microcrystalline structure and the breakdown of the translational symmetry of MWCNTs. Finally, the 2D (G') band which is the overtone of the D band can be seen at ~ 2663 cm^{-1}.

Polarized Raman spectroscopy has been proven very useful for the evaluation of the orientation of carbon nanotubes within a polymer matrix.[241] The intensity of the Raman G band of CNTs is known to decrease monotonously with increasing angle between the polarization direction of the polarizer and the nanotube axis.[242] Chang *et al.*[243] used polarized Raman spectroscopy for the evaluation of orientation in a SWCNT/polypropylene fibre composite and observed that the scattering intensity of the G band decreased significantly when the angle between the fibre axis and the polarization of light changed from 0 to 90°, revealing an orientation of SWCNTs along the fibre direction. In addition, in an excellent study by Peijs and coworkers[244] on oriented PVA/SWCNT tapes, the authors also used polarised Raman spectroscopy for the characterisation of the orientation of the nanotubes. They reported that when the scattered light is analysed parallel to the incident laser polarisation (VV geometry), the intensity of the Raman peaks is proportional to $\cos^4\theta$ where θ is the angle between the direction of the polariser and the fibre. The inten-

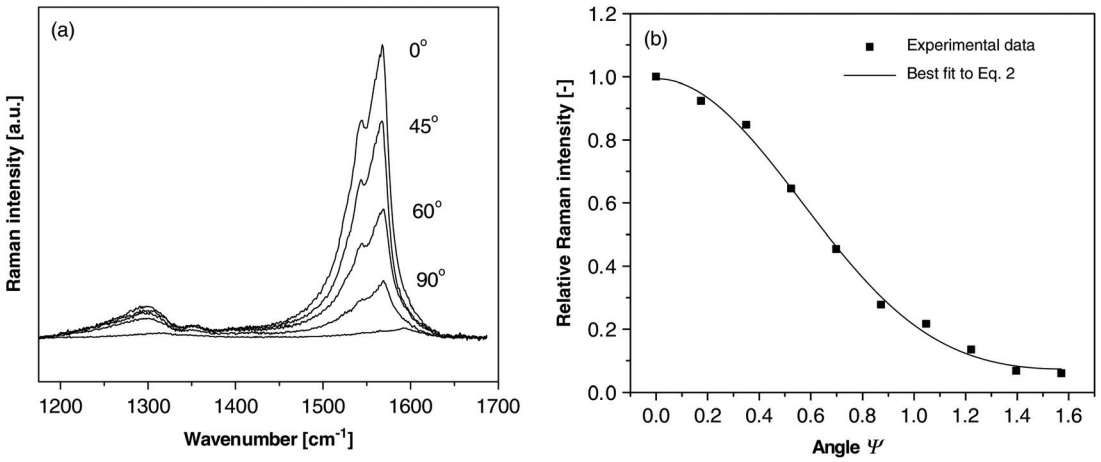

Fig. 24 (a) Raman spectra of oriented SWCNT-PVA composites, at different tape orientations, with respect to the incident polarization, (b) relative Raman intensity *versus* the angle between the polarization direction and the sample axis Ψ (0–π/2), at draw ratio 5, revealing a high degree of orientation of the SWCNTs.[244]

sity as a function of the angle between the drawing direction and incident polarization (Ψ) is given by:

$$I(\Psi) = \int_{\Psi-\pi/2}^{\Psi+\pi/2} cF(\theta - \Psi, \Delta)\cos^4\theta \mathrm{d}\theta \quad (34)$$

where the width of distribution is given by Δ, also c gives the maximum intensity when $\theta = 0$ and $F(\theta - \Psi, \Delta)$ is a distribution function given by:

$$F(\theta - \Psi, \Delta) = \frac{\Delta/2\pi}{[(\theta - \Psi)^2 - (\Delta/2)^2]} \quad (35)$$

where Δ is now the FWHM of the distribution and indicates the degree of orientation, as larger Δ shows higher degree of orientation. The results for the PVA/SWCNT tapes, revealed a high degree of alignment of the nanotubes (Fig. 24).

5.2.2 Deformation. The use of Raman spectroscopy for the evaluation of the stress distribution in carbon or aramid fibres and their composites, through the shifts of the characteristic Raman bands was well established when carbon nanotubes were first reported by Iijima and Ichihashi.[245] Naturally, the application of this experimental technique quickly expanded into the field of carbon nanotube composites. The seminal work of Cooper *et al.*[246] clearly demonstrated that the tensile deformation of CNT-filled composites can be characterised and followed *via* Raman spectroscopy. The authors monitored the stress transfer between the epoxy matrix and SWCNTs and MWCNTs from the characteristic Raman band shifts. It was shown that the characteristic downshift of the 2D (G') Raman peak for SWCNTs within the epoxy resin was -15 cm^{-1} %$^{-1}$, while for MWCNTs was in the order of -5.3 cm^{-1} %$^{-1}$. These slopes reveal the stress transfer efficiency from the matrix to the nanotubes and normally, the steeper the slope, the higher the stress transfer efficiency and thus, the effective modulus of the nanotubes. Additionally, as the research of Wagner and co-workers has shown, the band shift per unit strain is higher when the nanotubes are aligned along the directions of both the laser polarization and maximum strain.[241,247]

It should be noted that the deviations from linearity in the downshift of the characteristic Raman bands are indicators of an interface failure and thus, a less effective load transfer. Slippage of the CNTs (or the respective filler) takes place at the interface because the generally weak interfacial interactions cannot bear the shear stress, reducing this way the load transfer efficiency. Another important aspect of the study of Cooper *et al.* was the establishment of a method to calculate the effective modulus of nanotubes by using the universal calibration rate of -5 cm^{-1} %$^{-1}$ GPa^{-1} for the 2D (G') band in carbon fibres and assuming that this value was also valid for CNT composites. However, their approach led to wide bounds in terms of modulus calculation for the nanotubes since they did not take into account the polarization of the laser in their analysis. Deng *et al.*[248] in a subsequent study modelled the effective modulus of the nanotubes in PVA/SWCNT composite by suggesting that the effective modulus E_{eff} can be obtained by:

$$E_{\mathrm{eff}} = \frac{S_0}{-0.05} \quad (36)$$

where S_0 is the shift rate and -0.05 is the universal calibration rate. For an aligned system $S_0 = S(0)$, while for randomly oriented systems, the laser polarisation should be taken into account, which after a series of substitutions gives:

$$S_0 = 1.3 \times S_{\mathrm{VV}}\ (0) \quad (37)$$

$$S_0 = 3.3 \times S_{\mathrm{VH}}\ (0) \quad (38)$$

which suggests that the E_{eff} of the randomly oriented nanotubes can be calculated by using the universal calibration factor and corrected by multiplying by a factor of 1.3 for VV (incident and scattered lasers are parallel to the reference axis) configuration and 3.3 for VH (incident and scattered lasers are

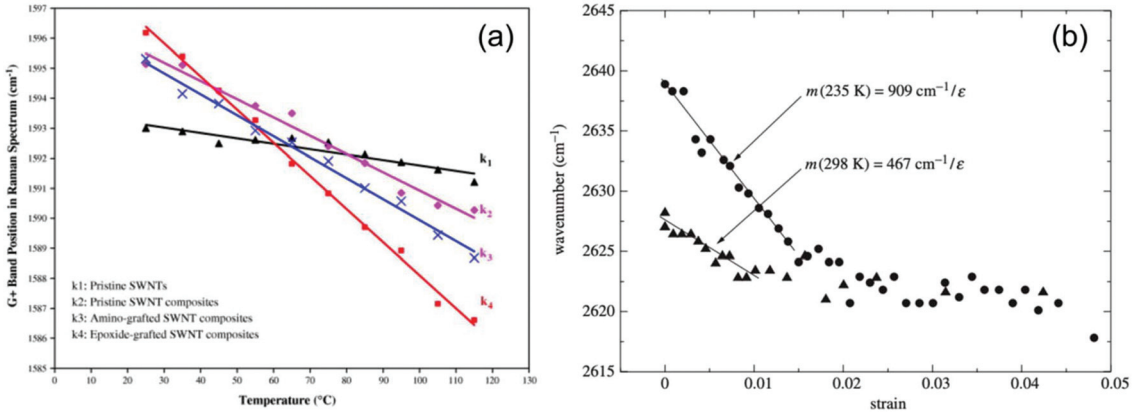

Fig. 25 (a) G^+ Raman band shift of the SWCNT-epoxy composites when heated[250] (Copyright 2008, with permission from Elsevier), (b) Raman band shift of the SWCNT-PUA composites under different temperatures.[251]

parallel and perpendicular, respectively, to the reference axis) configuration. The E_{eff} values reported in this work were in the order of 530–700 GPa. An empirical linear relationship has been proposed in the important study of Wood *et al.*[241] between Raman wavenumber shift of the D* band of SWCNTs and the stress σ in the polymer in the elastic regime:

$$\sigma = \left(\frac{\text{shift}}{m_1}\right) E_{\text{m}} \tag{39}$$

where m_1 is the proportionality constant (or calibration factor) and E_{m} is the matrix modulus. It should be noted that the matrix modulus is used for low nanotube contents, on the basis that the mechanical response of the composite is unchanged with respect to the pure polymer, while at higher filler contents the modulus of the nanocomposite sample should be taken into account. For the strain response of the D* (2D) peak for SWCNTs, the slope $m_1 = -467\ \text{cm}^{-1}/\varepsilon$ can be considered as the calibration value. Thus, a spectroscopic stress–strain curve can be constructed with the use of the Raman signal of CNTs in a matrix, under strain.

The effect of temperature on the Raman spectra of a CNT-based nanocomposite is also important, as a result of the differences in the coefficient of thermal expansion (CTE) and the rigidity of the polymer. For example, the CTE of SWCNTs is in the order of $10^{-6}\ ^\circ\text{C}^{-1}$, while the CTE of an epoxy resin is $\sim 6.5 \times 10^{-5}\ ^\circ\text{C}^{-1}$.[249] This difference leads to a large thermal stress in the filler-matrix interface. When the interfacial bonding is strong, then the interatomic distance of C atoms in the nanotube will increase due to thermal stress; this will cause a decrease of bonding potentials and a decline of the Raman vibration frequency. The work of Wang *et al.*[250] clearly exhibited that thermal loading in epoxy composites reinforced with neat and functionalised SWCNTs leads to a downshift of the Raman G^+ band with increasing temperature. Interestingly, pure SWCNTs (not mixed with the epoxy resin) showed a very small change in their Raman spectra, while all composite samples displayed a downshift, with the functionalized-SWCNT composites demonstrating a more efficient stress transfer (and a larger downshift) (Fig. 25a). On the other hand, it is well known that the modulus of the polymers is a temperature-dependent parameter. Thus, increasing the temperature can lead to a higher mobility of the macromolecular chains and subsequent decrease of the efficiency of stress transfer, while as expected, a decrease of the temperature leads to a restriction of the movement of the chains and to a stiffer matrix, which in turn contributes in a more efficient load transfer. This has been clearly demonstrated in the study of Zhao and Wagner,[251] where the authors prepared a polyurethane acrylate (PUA)-SWCNT composite and measured the Raman band shifts under different temperatures. As expected, the slope of the 2D (G') band at small strains (up to 2%) was higher at 235 K ($-9.09\ \text{cm}^{-1}\ \%^{-1}$ strain) than 298 K ($-4.67\ \text{cm}^{-1}\ \%^{-1}$ strain) (Fig. 25b). It is clear that the two phenomena are competitive to each other, thus the contributions from both should be taken into account when performing *in situ* Raman tests of carbon nanomaterials-reinforced composites at various temperatures.

In a more recent study by Young *et al.*[252] the authors studied the interfacial and internal stress transfer in nanocomposites reinforced with different types of carbon nanotubes (SWCNTs and MWCNTs). As expected, the downshift of the 2D (G') band in SWCNT-based composites was over four times higher than MWCNT composites ($-14.1 \pm 3.3\ \text{cm}^{-1}\ \%^{-1}$ strain over $-3.4 \pm 1.3\ \text{cm}^{-1}\ \%^{-1}$ strain) (Fig. 26a). Interfacial slippage took place for the SWCNTs at 0.5% strain. In the case of MWCNTs, it is the inner-wall slippage that delays the epoxy/MWCNT slippage at the interface, thus the interfacial stress transfer is considerably better. The authors modelled the deformation of the two types of nanotubes in the nanocomposites by introducing a stress transfer efficiency factor k_{i} ($0 \le k_{\text{i}} \le 1$), where for perfect stress transfer $k_{\text{i}} = 1$ and for no stress transfer $k_{\text{i}} = 0$. For the MWCNT/epoxy nanocomposites k_{i} was found to be around 0.7, attributed to imperfect bonding between layers, while k_{i} decreases with increasing number of layers (Fig. 26b). Importantly, the authors suggested that the

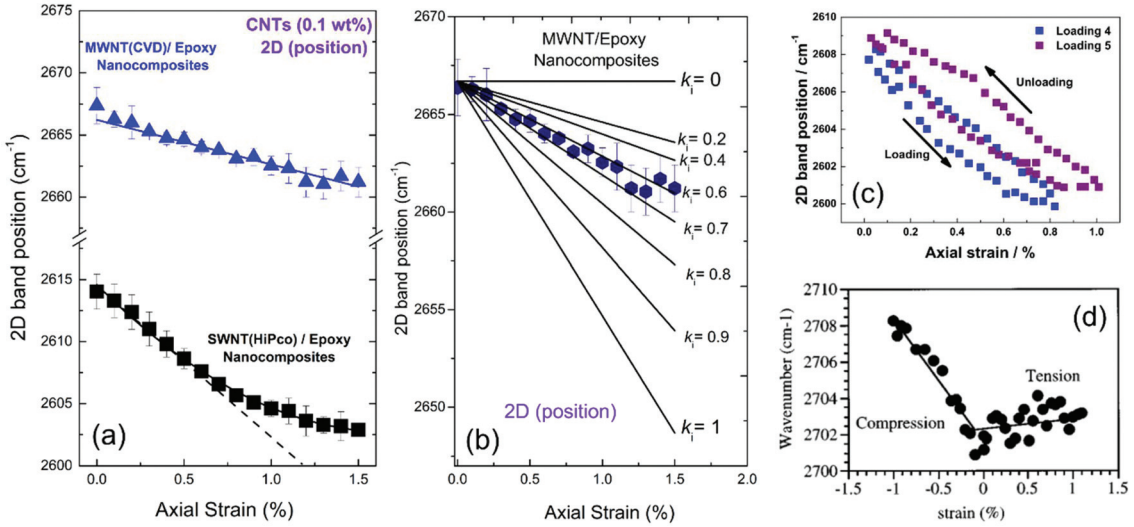

Fig. 26 (a) Shift of the 2D (G') band positions of SWCNT- and MWCNT-reinforced epoxy nanocomposites, (b) shift of the Raman 2D (G') band (hexagons) and theoretical simulation as a function of strain (straight lines) at different values of stress transfer efficiency parameters[252] (Copyright 2016, Springer Nature Publishing Group), (c) shift of the Raman 2D (G') band for cyclic deformation for 0.8 and 1% maximum loading strain for an epoxy-SWCNT nanocomposite. Data showing both loading (blue squares) and unloading (purple squares) procedures[254] (Copyright 2016, Springer Nature Publishing Group), (d) Raman Wavenumber shift as a function of strain for a MWCNT-epoxy nanocomposite[168] (Reprinted with permission from AIP).

load in MWCNT-based nanocomposites is taken mainly by the outside layer and the inner layers actually decrease the reinforcement efficiency. It should be pointed out that a similar stress transfer efficiency factor of around 0.7 was found for few-layer graphene (Fig. 18a),[221] showing the similarity of the interlayer stress transfer phenomenon for the different carbon nanomaterials.

Winey and coworkers[253] on their study on SWCNT/PMMA fibres reported a downshift of the G band of -7.5 cm^{-1} %$^{-1}$ strain for small strains (up to 0.2% strain). The authors also identified that during the unloading procedure the G peak position recovered back linearly at the same rate, while after the second loading, the G peak displayed the characteristic downshift at the same rate with the initial loading procedure, revealing the reversibility of load transfer. Kao and Young[254] also looked into the cyclic deformation of epoxy/SWCNT composites and as expected, the maximum loading strain and loading cycles affected significantly the interfacial adhesion. A hysteresis loop was obtained from the mismatch between the loading and unloading processes, due to the damage at the nanotube-epoxy interface, which enabled the authors to calculate the energy dissipation and modelling of the interface damage (Fig. 26c).

The deformation of a MWCNT/epoxy nanocomposite under tension and compression was investigated in the work of Schadler *et al.*[168] (Fig. 26d). The 2D (G') band shifted upwards by ~7 cm^{-1} under 1% compressive strain, while under tension, a slightly downward shift was reported. This observation was in contrast with the bulk mechanical properties of the composites, which indicated a ~24% improvement of compression modulus and a ~20% improvement in tension modulus. The difference arises from the different modes of deformation in the two experimental techniques. The MWCNTs are expected to carry the load from their outer tube to the inner tubes, but in practice this is difficult due to weak van der Waals interactions between the tubes. Therefore, under tension, the deformation of the inner walls is small. Thus, since the Raman signal is averaged for the whole MWCNT, the overall peak shift is insignificant. On the other hand, during compression the load is transferred effectively to the inner tubes through buckling and bending of the nanotubes, while slippage under compression is prevented due to seamless structure of MWCNTs and geometrical constrains the outer layers impose on the inner layers. This has as a result pronounced upward shifts of the 2D (G') band.

The functionalization of CNTs for the improvement of both the dispersion and interfacial properties can also lead to a differentiation of the Raman band shifts, compared to the unfunctionalized materials. For example, the work of Liu *et al.*[255] revealed that the functionalization of SWCNTs with hydroxyl groups (SWCNT-OH) led to a more efficient stress transfer than neat SWCNTs in a PVA matrix; thus, the band shift of the PVA/0.5 wt% SWCNTs was in the order of -2.61 cm^{-1} %$^{-1}$ strain, while the band shift of the PVA/0.6wt% SWCNT-OH was in the order of -36.9 cm^{-1} %$^{-1}$ strain. The same conclusion comes out of the study of Lachman *et al.*[256] where carboxylated SWCNTs (SWCNT-COOH) within a PVA matrix, displayed higher shifts at low strains, than the neat SWCNT-PVA composites, as a result of the better interfacial adhesion. However, the bulk mechanical properties of the SWCNT-PVA fibres were better than the COOH-SWCNT/PVA fibres, as a result of the carboxylation procedure, which is known to degrade the wall structure of nanotubes.

Even though the deformation of individual carbon nanotubes cannot be followed *via* the application of strain in combination with Raman spectroscopy as a result of their nanoscale dimensions, they can be used as coatings of different types of

fibres and the local stress can then be studied by using Raman spectroscopy. The works of Jin *et al.*[257,258] revealed that the coating of low- and high-modulus carbon fibres with carboxylated SWCNTs enabled them to analyse the fibre fragmentation during the deformation process and to follow the 2D Raman band shifts along the fibre length. The presence of the SWCNTs led to very high interfacial shear stress, in the order of 50 MPa and >30 MPa for low- and high-modulus carbon fibres, respectively, as a result of the additional bonding caused by the presence of the functional groups.

6. Conclusions and outlook

Graphene-related materials and carbon nanotubes offer unique opportunities for the evolution of polymer nanocomposites towards enhanced performance and multifunctionality. The reinforcement mechanisms of both types of nanocomposites have been reviewed thoroughly in the present manuscript by evaluating the inherent properties of the nanofillers and the parameters that affect significantly the ultimate properties of the polymer nanocomposites. Various well-established micromechanical theories that were developed initially for continuous composites have been examined for their applicability in polymer nanocomposites and there is overwhelming evidence that the elastic deformation of graphene- or nanotube-reinforced polymers can be modelled using classical composite micromechanics. Finally, the usefulness of Raman spectroscopy on the assessment of the mechanical properties of both nanofillers has been highlighted; numerous qualities and characteristics of sp^2 carbon allotropes can be identified through the use of Raman spectroscopy. The shift rates of the Raman bands are highly dependent on the Young's modulus of the nanocarbons and thus, it has been shown how they can be used as universal stress sensors for the study of the mechanics of polymer nanocomposites.

Overall it can be concluded that both types of nanofillers can reinforce low-modulus polymers significantly as a result of their inherent properties. Obviously, they display different reinforcement characteristics as a result of their completely different geometry and various parameters that originate from processing. The CNT-related materials, when aligned, display a remarkably-high aspect ratio that contributes to the creation of a large polymer-filler interface, which subsequently leads to very high levels of mechanical reinforcement. Thus, in this case the CNTs perform better than GRMs; however, alignment of CNTs even at a laboratory scale is quite challenging to achieve and scaling up of these processes at an industrial level is still uncertain. On the other hand, when CNTs are randomly oriented, they reinforce polymers less effectively than GRMs, because of their 1D geometry, which leads to a reduction of their effective modulus by 5, as can be concluded from their Krenchel orientation factor. In comparison, when GRMs are randomly oriented within a polymer, their effective modulus drops to less than half (8/15) as a consequence of their 2D geometry. Another major disadvantage of CNTs in the production of high-performing polymer nanocomposites is the very large increase in the viscosity of the final materials, which comes as a result of the formation of entanglements between CNTs, leading to a significantly poorer dispersion and a reduction of the effective aspect ratio of nanotubes. On the other hand, graphene related materials are much easier to process at higher loadings, as the viscosity of the polymer-graphene mixture is commonly significantly lower. One additional advantage of nanoplatelet-type materials such as GRMs, is that they can display an increased ability to alter a larger zone of polymer than nanotubes as a result of their micron-size lateral dimensions, through the creation of cooperating regions of altered dynamics, which can interact with each over above a certain percolation threshold volume fraction.

Despite the relatively high level of understanding of the mechanical reinforcement mechanisms of polymer nanocomposites with GRMs or CNTs, the impressive mechanical properties of both nanofillers still have not been fully realised in composite structures. The creation of continuous composites with lightweight spun fibres produced by CNTs or GRMs can be a solution to this problem, where both the unique multifunctional properties of both nanocarbons could be employed along with enhanced performance at very high filler loadings. Obviously the 1D materials (CNTs) are more appropriate than 2D materials (GRMs) for the creation of continuous fibres, leading to high inter-tube stress transfer and so far, CNT-based fibres seem to outperform GRM-based ones. Another critical aspect for the maximization of the performance of both nanocarbons in polymer nanocomposites is the precise engineering of the polymer-filler interface, that contributes significantly to the mechanical properties of the composites. Direct growth of CNTs or graphene onto macroscale glass/carbon fibres can lead to an increased cross-plane improvement in interlaminar shear stress, while evidently, the chemical modification of both fillers can enhance the polymer-filler interactions and as a consequence, the mechanical properties.

Even though the mechanical reinforcement characteristics of both nanocarbons has been explored for numerous polymer matrices, a number of challenges still exist and prevent full understanding of the reinforcement mechanisms, maximization of the performance of the composites and production of such composites extensively in an industrial scale. For example, the scale-up of the production of high-quality and low-cost GRMs is a major issue that reflects on both the commercialization and ultimate properties of the materials. From a modelling viewpoint, the mechanical strength of the polymer nanocomposites and the extent of the interfacial zone for both nanofillers should be analysed, while in terms of production the effective toughening of various polymers at low filler contents and the formation of composites with hybrid (1D:2D) nanofillers should be explored.

Conflicts of interest

There are no conflicts to declare.

Acknowledgements

This project has received funding from the European Union's Horizon 2020 Research and Innovation Programme under grant agreement no. 785219, the Royal Academy of Engineering and Morgan Advanced Materials.

References

1 E. T. Thostenson, Z. Ren and T.-W. Chou, Advances in the science and technology of carbon nanotubes and their composites: a review, *Compos. Sci. Technol.*, 2001, **61**(13), 1899–1912.
2 D. G. Papageorgiou, I. A. Kinloch and R. J. Young, Mechanical properties of graphene and graphene-based nanocomposites, *Prog. Mater. Sci.*, 2017, **90**, 75–127.
3 K. S. Novoselov, A. K. Geim, S. Morozov, D. Jiang, Y. Zhang, S. Dubonos, I. Grigorieva and A. Firsov, Electric field effect in atomically thin carbon films, *Science*, 2004, **306**(5696), 666–669.
4 R. R. Nair, P. Blake, A. N. Grigorenko, K. S. Novoselov, T. J. Booth, T. Stauber, N. M. Peres and A. K. Geim, Fine structure constant defines visual transparency of graphene, *Science*, 2008, **320**(5881), 1308.
5 L. Gong, I. A. Kinloch, R. J. Young, I. Riaz, R. Jalil and K. S. Novoselov, Interfacial stress transfer in a graphene monolayer nanocomposite, *Adv. Mater.*, 2010, **22**(24), 2694–2697.
6 H. Cox, The elasticity and strength of paper and other fibrous materials, *Br. J. Appl. Phys.*, 1952, **3**(3), 72.
7 A. Kelly and W. Tyson, Tensile properties of fibre-reinforced metals: copper/tungsten and copper/molybdenum, *J. Mech. Phys. Solids*, 1965, **13**(6), 329–350.
8 R. Saito, M. Hofmann, G. Dresselhaus, A. Jorio and M. S. Dresselhaus, Raman spectroscopy of graphene and carbon nanotubes, *Adv. Phys.*, 2011, **60**(3), 413–550.
9 G. Marom and H. D. Wagner, Should polymer nanocomposites be regarded as molecular composites?, *J. Mater. Sci.*, 2017, **52**(14), 8357–8361.
10 P. Calvert, Strength in disunity, *Nature*, 1992, **357**(6377), 365–366.
11 C. Lee, X. Wei, J. W. Kysar and J. Hone, Measurement of the elastic properties and intrinsic strength of monolayer graphene, *Science*, 2008, **321**(5887), 385–388.
12 C. S. Ruiz-Vargas, H. L. Zhuang, P. Y. Huang, A. M. Van Der Zande, S. Garg, P. L. McEuen, D. A. Muller, R. G. Hennig and J. Park, Softened elastic response and unzipping in chemical vapor deposition graphene membranes, *Nano Lett.*, 2011, **11**(6), 2259–2263.
13 R. J. Nicholl, H. J. Conley, N. V. Lavrik, I. Vlassiouk, Y. S. Puzyrev, V. P. Sreenivas, S. T. Pantelides and K. I. Bolotin, The effect of intrinsic crumpling on the mechanics of free-standing graphene, *Nat. Commun.*, 2015, **6**, 8789.
14 G. López-Polín, C. Gómez-Navarro, V. Parente, F. Guinea, M. I. Katsnelson, F. Pérez-Murano and J. Gómez-Herrero, Increasing the elastic modulus of graphene by controlled defect creation, *Nat. Phys.*, 2014, **11**, 26.
15 J. H. Kim, J. H. Jeong, N. Kim, R. Joshi and G.-H. Lee, Mechanical properties of two-dimensional materials and their applications, *J. Phys. D: Appl. Phys.*, 2018, **52**(8), 083001.
16 A. Shekhawat and R. O. Ritchie, Toughness and strength of nanocrystalline graphene, *Nat. Commun.*, 2016, **7**, 10546.
17 A. Zandiatashbar, G.-H. Lee, S. J. An, S. Lee, N. Mathew, M. Terrones, T. Hayashi, C. R. Picu, J. Hone and N. Koratkar, Effect of defects on the intrinsic strength and stiffness of graphene, *Nat. Commun.*, 2014, **5**, 3186.
18 X. Zhao, D. G. Papageorgiou, L. Zhu, F. Ding and R. J. Young, The strength of mechanically-exfoliated monolayer graphene deformed on a rigid polymer substrate, *Nanoscale*, 2019, **11**(30), 14339–14353.
19 P. Zhang, L. Ma, F. Fan, Z. Zeng, C. Peng, P. E. Loya, Z. Liu, Y. Gong, J. Zhang and X. Zhang, Fracture toughness of graphene, *Nat. Commun.*, 2014, **5**, 3782.
20 G. Jung, Z. Qin and M. J. Buehler, Molecular mechanics of polycrystalline graphene with enhanced fracture toughness, *Extreme Mech. Lett.*, 2015, **2**, 52–59.
21 M. J. Treacy, T. Ebbesen and J. Gibson, Exceptionally high Young's modulus observed for individual carbon nanotubes, *Nature*, 1996, **381**(6584), 678.
22 E. W. Wong, P. E. Sheehan and C. M. Lieber, Nanobeam mechanics: elasticity, strength, and toughness of nanorods and nanotubes, *Science*, 1997, **277**(5334), 1971–1975.
23 A. Krishnan, E. Dujardin, T. W. Ebbesen, P. N. Yianilos and M. M. J. Treacy, Young's modulus of single-walled nanotubes, *Phys. Rev. B: Condens. Matter Mater. Phys.*, 1998, **58**(20), 14013–14019.
24 M.-F. Yu, B. S. Files, S. Arepalli and R. S. Ruoff, Tensile loading of ropes of single wall carbon nanotubes and their mechanical properties, *Phys. Rev. Lett.*, 2000, **84**(24), 5552.
25 J. P. Salvetat, A. J. Kulik, J. M. Bonard, G. A. D. Briggs, T. Stöckli, K. Méténier, S. Bonnamy, F. Béguin, N. A. Burnham and L. Forró, Elastic modulus of ordered and disordered multiwalled carbon nanotubes, *Adv. Mater.*, 1999, **11**(2), 161–165.
26 P. Poncharal, Z. Wang, D. Ugarte and W. A. De Heer, Electrostatic deflections and electromechanical resonances of carbon nanotubes, *Science*, 1999, **283**(5407), 1513–1516.
27 M.-F. Yu, O. Lourie, M. J. Dyer, K. Moloni, T. F. Kelly and R. S. Ruoff, Strength and breaking mechanism of multiwalled carbon nanotubes under tensile load, *Science*, 2000, **287**(5453), 637–640.
28 B. I. Yakobson, Fullerenes, in *Recent advances in the chemistry and physics of fullerenes and related materials*, ed. K. M. Kadish and R. S. Ruoff, Electrochemical Society, Pennington, NJ, 1997, pp. 549–560.

29 M. B. Nardelli, B. I. Yakobson and J. Bernholc, Brittle and ductile behavior in carbon nanotubes, *Phys. Rev. Lett.*, 1998, **81**(21), 4656.
30 M. R. Falvo, G. J. Clary, R. M. Taylor II, V. Chi, F. P. Brooks Jr., S. Washburn and R. Superfine, Bending and buckling of carbon nanotubes under large strain, *Nature*, 1997, **389**, 582.
31 D. Walters, L. Ericson, M. Casavant, J. Liu, D. Colbert, K. Smith and R. Smalley, Elastic strain of freely suspended single-wall carbon nanotube ropes, *Appl. Phys. Lett.*, 1999, **74**(25), 3803–3805.
32 B. G. Demczyk, Y. M. Wang, J. Cumings, M. Hetman, W. Han, A. Zettl and R. O. Ritchie, Direct mechanical measurement of the tensile strength and elastic modulus of multiwalled carbon nanotubes, *Mater. Sci. Eng., A*, 2002, **334**(1), 173–178.
33 H. Wagner, O. Lourie, Y. Feldman and R. Tenne, Stress-induced fragmentation of multiwall carbon nanotubes in a polymer matrix, *Appl. Phys. Lett.*, 1998, **72**(2), 188–190.
34 S. Ogata and Y. Shibutani, Ideal tensile strength and band gap of single-walled carbon nanotubes, *Phys. Rev. B: Condens. Matter Mater. Phys.*, 2003, **68**(16), 165409.
35 T. Dumitrică, T. Belytschko and B. I. Yakobson, Bond-breaking bifurcation states in carbon nanotube fracture, *J. Chem. Phys.*, 2003, **118**(21), 9485–9488.
36 G. G. Samsonidze, G. G. Samsonidze and B. I. Yakobson, Kinetic theory of symmetry-dependent strength in carbon nanotubes, *Phys. Rev. Lett.*, 2002, **88**(6), 065501.
37 B. Peng, M. Locascio, P. Zapol, S. Li, S. L. Mielke, G. C. Schatz and H. D. Espinosa, Measurements of near-ultimate strength for multiwalled carbon nanotubes and irradiation-induced crosslinking improvements, *Nat. Nanotechnol.*, 2008, **3**(10), 626.
38 Y. Li, Z. Feng, L. Huang, K. Essa, E. Bilotti, H. Zhang, T. Peijs and L. Hao, Additive Manufacturing High Performance Graphene-based Composites: A Review, *Composites, Part A*, 2019, 105483.
39 W. Chee, H. Lim, N. Huang and I. Harrison, Nanocomposites of graphene/polymers: a review, *RSC Adv.*, 2015, **5**(83), 68014–68051.
40 V. Mittal, Functional polymer nanocomposites with graphene: a review, *Macromol. Mater. Eng.*, 2014, **299**(8), 906–931.
41 D. G. Papageorgiou, I. A. Kinloch and R. J. Young, Graphene/elastomer nanocomposites, *Carbon*, 2015, **95**, 460–484.
42 E. Lago, P. S. Toth, G. Pugliese, V. Pellegrini and F. Bonaccorso, Solution blending preparation of polycarbonate/graphene composite: boosting the mechanical and electrical properties, *RSC Adv.*, 2016, **6**(100), 97931–97940.
43 S. Park, S. He, J. Wang, A. Stein and C. W. Macosko, Graphene-polyethylene nanocomposites: Effect of graphene functionalization, *Polymer*, 2016, **104**, 1–9.
44 H. Xu, L.-X. Gong, X. Wang, L. Zhao, Y.-B. Pei, G. Wang, Y.-J. Liu, L.-B. Wu, J.-X. Jiang and L.-C. Tang, Influence of processing conditions on dispersion, electrical and mechanical properties of graphene-filled-silicone rubber composites, *Composites, Part A*, 2016, **91**, 53–64.
45 X. Cheng, V. Kumar, T. Yokozeki, T. Goto, T. Takahashi, J. Koyanagi, L. Wu and R. Wang, Highly conductive graphene oxide/polyaniline hybrid polymer nanocomposites with simultaneously improved mechanical properties, *Composites, Part A*, 2016, **82**, 100–107.
46 C. Vallés, F. Beckert, L. Burk, R. Mülhaupt, R. J. Young and I. A. Kinloch, Effect of the C/O ratio in graphene oxide materials on the reinforcement of epoxy-based nanocomposites, *J. Polym. Sci., Part B: Polym. Phys.*, 2016, **54**(2), 281–291.
47 Y. Hernandez, V. Nicolosi, M. Lotya, F. M. Blighe, Z. Sun, S. De, I. T. McGovern, B. Holland, M. Byrne, Y. K. Gun'Ko, J. J. Boland, P. Niraj, G. Duesberg, S. Krishnamurthy, R. Goodhue, J. Hutchison, V. Scardaci, A. C. Ferrari and J. N. Coleman, High-yield production of graphene by liquid-phase exfoliation of graphite, *Nat. Nanotechnol.*, 2008, **3**, 563.
48 E.-C. Cho, J.-H. Huang, C.-P. Li, C.-W. Chang-Jian, K.-C. Lee, Y.-S. Hsiao and J.-H. Huang, Graphene-based thermoplastic composites and their application for LED thermal management, *Carbon*, 2016, **102**, 66–73.
49 D. G. Papageorgiou, I. A. Kinloch and R. J. Young, Hybrid multifunctional graphene/glass-fibre polypropylene composites, *Compos. Sci. Technol.*, 2016, **137**, 44–51.
50 Y. Liu and J. Feng, An attempt towards fabricating reduced graphene oxide composites with traditional polymer processing techniques by adding chemical reduction agents, *Compos. Sci. Technol.*, 2017, **140**, 16–22.
51 P. Bhawal, S. Ganguly, T. K. Das, S. Mondal, S. Choudhury and N. C. Das, Superior electromagnetic interference shielding effectiveness and electro-mechanical properties of EMA-IRGO nanocomposites through the *in situ* reduction of GO from melt blended EMA-GO composites, *Composites, Part B*, 2018, **134**, 46–60.
52 D. G. Papageorgiou, Z. Terzopoulou, A. Fina, F. Cuttica, G. Z. Papageorgiou, D. N. Bikiaris, K. Chrissafis, R. J. Young and I. A. Kinloch, Enhanced thermal and fire retardancy properties of polypropylene reinforced with a hybrid graphene/glass-fibre filler, *Compos. Sci. Technol.*, 2018, **156**, 95–102.
53 M. Liebscher, M.-O. Blais, P. Pötschke and G. Heinrich, A morphological study on the dispersion and selective localization behavior of graphene nanoplatelets in immiscible polymer blends of PC and SAN, *Polymer*, 2013, **54**(21), 5875–5882.
54 D. G. Papageorgiou, M. Liu, Z. Li, C. Vallés, R. J. Young and I. A. Kinloch, Hybrid poly(ether ether ketone) composites reinforced with a combination of carbon fibres and graphene nanoplatelets, *Compos. Sci. Technol.*, 2019, **175**, 60–68.
55 M. Liu, D. G. Papageorgiou, S. Li, K. Lin, I. A. Kinloch and R. J. Young, Micromechanics of reinforcement of a graphene-based thermoplastic elastomer nanocomposite, *Composites, Part A*, 2018, **110**, 84–92.

56 R. Santos, S. Mould, P. Formánek, M. Paiva and J. Covas, Effects of particle size and surface chemistry on the dispersion of graphite nanoplates in polypropylene composites, *Polymers*, 2018, **10**(2), 222.
57 R. Santos, C. Vilaverde, E. Cunha, M. Paiva and J. Covas, Probing dispersion and re-agglomeration phenomena upon melt-mixing of polymer-functionalized graphite nanoplates, *Soft Matter*, 2016, **12**(1), 77–86.
58 C. Vilaverde, R. M. Santos, M. C. Paiva and J. A. Covas, Dispersion and re-agglomeration of graphite nanoplates in polypropylene melts under controlled flow conditions, *Composites, Part A*, 2015, **78**, 143–151.
59 Z. Xu and C. Gao, In situ polymerization approach to graphene-reinforced nylon-6 composites, *Macromolecules*, 2010, **43**(16), 6716–6723.
60 X. Wang, Y. Hu, L. Song, H. Yang, W. Xing and H. Lu, In situ polymerization of graphene nanosheets and polyurethane with enhanced mechanical and thermal properties, *J. Mater. Chem.*, 2011, **21**(12), 4222–4227.
61 N. D. Luong, U. Hippi, J. T. Korhonen, A. J. Soininen, J. Ruokolainen, L.-S. Johansson, J.-D. Nam and J. Seppälä, Enhanced mechanical and electrical properties of polyimide film by graphene sheets via in situ polymerization, *Polymer*, 2011, **52**(23), 5237–5242.
62 M. A. Milani, D. González, R. Quijada, N. R. Basso, M. L. Cerrada, D. S. Azambuja and G. B. Galland, Polypropylene/graphene nanosheet nanocomposites by in situ polymerization: synthesis, characterization and fundamental properties, *Compos. Sci. Technol.*, 2013, **84**, 1–7.
63 X. Zhao, Q. Zhang, Y. Hao, Y. Li, Y. Fang and D. Chen, Alternate Multilayer Films of Poly(vinyl alcohol) and Exfoliated Graphene Oxide Fabricated via a Facial Layer-by-Layer Assembly, *Macromolecules*, 2010, **43**(22), 9411–9416.
64 C. Vallés, X. Zhang, J. Cao, F. Lin, R. J. Young, A. Lombardo, A. C. Ferrari, L. Burk, R. Mülhaupt and I. A. Kinloch, Graphene/Polyelectrolyte Layer-by-Layer Coatings for Electromagnetic Interference Shielding, *ACS Appl. Nano Mater.*, 2019, **2**(8), 5272–5281.
65 F.-X. Xiao, M. Pagliaro, Y.-J. Xu and B. Liu, Layer-by-layer assembly of versatile nanoarchitectures with diverse dimensionality: a new perspective for rational construction of multilayer assemblies, *Chem. Soc. Rev.*, 2016, **45**(11), 3088–3121.
66 S. Colonna, M. M. Bernal, G. Gavoci, J. Gomez, C. Novara, G. Saracco and A. Fina, Effect of processing conditions on the thermal and electrical conductivity of poly (butylene terephthalate) nanocomposites prepared via ring-opening polymerization, *Mater. Des.*, 2017, **119**, 124–132.
67 S. Colonna, O. Monticelli, J. Gomez, C. Novara, G. Saracco and A. Fina, Effect of morphology and defectiveness of graphene-related materials on the electrical and thermal conductivity of their polymer nanocomposites, *Polymer*, 2016, **102**, 292–300.
68 A. Maio, R. Fucarino, R. Khatibi, S. Rosselli, M. Bruno and R. Scaffaro, A novel approach to prevent graphene oxide re-aggregation during the melt compounding with polymers, *Compos. Sci. Technol.*, 2015, **119**, 131–137.
69 N. Yousefi, M. M. Gudarzi, Q. Zheng, X. Lin, X. Shen, J. Jia, F. Sharif and J.-K. Kim, Highly aligned, ultralarge-size reduced graphene oxide/polyurethane nanocomposites: Mechanical properties and moisture permeability, *Composites, Part A*, 2013, **49**, 42–50.
70 P.-G. Ren, D.-X. Yan, T. Chen, B.-Q. Zeng and Z.-M. Li, Improved properties of highly oriented graphene/polymer nanocomposites, *J. Appl. Polym. Sci.*, 2011, **121**(6), 3167–3174.
71 S. Wu, R. B. Ladani, J. Zhang, E. Bafekrpour, K. Ghorbani, A. P. Mouritz, A. J. Kinloch and C. H. Wang, Aligning multilayer graphene flakes with an external electric field to improve multifunctional properties of epoxy nanocomposites, *Carbon*, 2015, **94**, 607–618.
72 X. Li, G. B. McKenna, G. Miquelard-Garnier, A. Guinault, C. Sollogoub, G. Regnier and A. Rozanski, Forced assembly by multilayer coextrusion to create oriented graphene reinforced polymer nanocomposites, *Polymer*, 2014, **55**(1), 248–257.
73 I. Vlassiouk, G. Polizos, R. Cooper, I. Ivanov, J. K. Keum, F. Paulauskas, P. Datskos and S. Smirnov, Strong and Electrically Conductive Graphene-Based Composite Fibers and Laminates, *ACS Appl. Mater. Interfaces*, 2015, **7**(20), 10702–10709.
74 P. Liu, Z. Jin, G. Katsukis, L. W. Drahushuk, S. Shimizu, C.-J. Shih, E. D. Wetzel, J. K. Taggart-Scarff, B. Qing, K. J. Van Vliet, R. Li, B. L. Wardle and M. S. Strano, Layered and scrolled nanocomposites with aligned semi-infinite graphene inclusions at the platelet limit, *Science*, 2016, **353**(6297), 364.
75 M. Yoonessi, J. R. Gaier, J. A. Peck and M. A. Meador, Controlled direction of electrical and mechanical properties in nickel tethered graphene polyimide nanocomposites using magnetic field, *Carbon*, 2015, **84**, 375–382.
76 Y. Yang, X. Li, M. Chu, H. Sun, J. Jin, K. Yu, Q. Wang, Q. Zhou and Y. Chen, Electrically assisted 3D printing of nacre-inspired structures with self-sensing capability, *Sci. Adv.*, 2019, **5**(4), eaau9490.
77 Z. Li, R. J. Young, N. R. Wilson, I. A. Kinloch, C. Vallés and Z. Li, Effect of the orientation of graphene-based nanoplatelets upon the Young's modulus of nanocomposites, *Compos. Sci. Technol.*, 2016, **123**, 125–133.
78 Z. Li, R. J. Young, I. A. Kinloch, N. R. Wilson, A. J. Marsden and A. P. A. Raju, Quantitative determination of the spatial orientation of graphene by polarized Raman spectroscopy, *Carbon*, 2015, **88**, 215–224.
79 C. Vallés, A. M. Abdelkader, R. J. Young and I. A. Kinloch, The effect of flake diameter on the reinforcement of few-layer graphene–PMMA composites, *Compos. Sci. Technol.*, 2015, **111**, 17–22.
80 C. Vallés, A. M. Abdelkader, R. J. Young and I. A. Kinloch, Few layer graphene–polypropylene nanocomposites: the role of flake diameter, *Faraday Discuss.*, 2014, **173**(0), 379–390.

81 S. G. Prolongo, A. Jiménez-Suárez, R. Moriche and A. Ureña, Graphene nanoplatelets thickness and lateral size influence on the morphology and behavior of epoxy composites, *Eur. Polym. J.*, 2014, **53**, 292–301.
82 Z. Li, T. J. A. Slater, X. Ma, Y. Yu, R. J. Young and T. L. Burnett, The taxonomy of graphite nanoplatelets and the influence of nanocomposite processing, *Carbon*, 2019, **142**, 99–106.
83 S. Li, Z. Li, T. L. Burnett, T. J. A. Slater, T. Hashimoto and R. J. Young, Nanocomposites of graphene nanoplatelets in natural rubber: microstructure and mechanisms of reinforcement, *J. Mater. Sci.*, 2017, **52**(16), 9558–9572.
84 X. Wu, T. Lin, Z. Tang, B. Guo and G. Huang, Natural rubber/graphene oxide composites: Effect of sheet size on mechanical properties and strain-induced crystallization behavior, *eXPRESS Polym. Lett.*, 2015, **9**(8), 672–685.
85 V. M. Pereira, A. H. Castro Neto, H. Y. Liang and L. Mahadevan, Geometry, Mechanics, and Electronics of Singular Structures and Wrinkles in Graphene, *Phys. Rev. Lett.*, 2010, **105**(15), 156603.
86 C. Androulidakis, E. N. Koukaras, J. Rahova, K. Sampathkumar, J. Parthenios, K. Papagelis, O. Frank and C. Galiotis, Wrinkled Few-Layer Graphene as Highly Efficient Load Bearer, *ACS Appl. Mater. Interfaces*, 2017, **9**(31), 26593–26601.
87 M. A. Rafiee, J. Rafiee, I. Srivastava, Z. Wang, H. Song, Z.-Z. Yu and N. Koratkar, Fracture and Fatigue in Graphene Nanocomposites, *Small*, 2010, **6**(2), 179–183.
88 T. Ramanathan, A. A. Abdala, S. Stankovich, D. A. Dikin, M. Herrera-Alonso, R. D. Piner, D. H. Adamson, H. C. Schniepp, X. Chen, R. S. Ruoff, S. T. Nguyen, I. A. Aksay, R. K. Prud'Homme and L. C. Brinson, Functionalized graphene sheets for polymer nanocomposites, *Nat. Nanotechnol.*, 2008, **3**, 327.
89 M. A. Rafiee, J. Rafiee, Z. Wang, H. Song, Z.-Z. Yu and N. Koratkar, Enhanced Mechanical Properties of Nanocomposites at Low Graphene Content, *ACS Nano*, 2009, **3**(12), 3884–3890.
90 R. Moriche, S. G. Prolongo, M. Sánchez, A. Jiménez-Suárez, M. J. Sayagués and A. Ureña, Morphological changes on graphene nanoplatelets induced during dispersion into an epoxy resin by different methods, *Composites, Part B*, 2015, **72**, 199–205.
91 Z. Wang and M. Devel, Periodic ripples in suspended graphene, *Phys. Rev. B: Condens. Matter Mater. Phys.*, 2011, **83**(12), 125422.
92 S.-H. Liao, P.-L. Liu, M.-C. Hsiao, C.-C. Teng, C.-A. Wang, M.-D. Ger and C.-L. Chiang, One-Step Reduction and Functionalization of Graphene Oxide with Phosphorus-Based Compound to Produce Flame-Retardant Epoxy Nanocomposite, *Ind. Eng. Chem. Res.*, 2012, **51**(12), 4573–4581.
93 V. Georgakilas, M. Otyepka, A. B. Bourlinos, V. Chandra, N. Kim, K. C. Kemp, P. Hobza, R. Zboril and K. S. Kim, Functionalization of Graphene: Covalent and Non-Covalent Approaches, Derivatives and Applications, *Chem. Rev.*, 2012, **112**(11), 6156–6214.
94 N. Rubio, H. Au, H. S. Leese, S. Hu, A. J. Clancy and M. S. P. Shaffer, Grafting from versus Grafting to Approaches for the Functionalization of Graphene Nanoplatelets with Poly(methyl methacrylate), *Macromolecules*, 2017, **50**(18), 7070–7079.
95 B. Shen, W. Zhai, M. Tao, D. Lu and W. Zheng, Chemical functionalization of graphene oxide toward the tailoring of the interface in polymer composites, *Compos. Sci. Technol.*, 2013, **77**, 87–94.
96 S. Quiles-Díaz, P. Enrique-Jimenez, D. G. Papageorgiou, F. Ania, A. Flores, I. A. Kinloch, M. A. Gómez-Fatou, R. J. Young and H. J. Salavagione, Influence of the chemical functionalization of graphene on the properties of polypropylene-based nanocomposites, *Composites, Part A*, 2017, **100**, 31–39.
97 Y.-J. Wan, L.-X. Gong, L.-C. Tang, L.-B. Wu and J.-X. Jiang, Mechanical properties of epoxy composites filled with silane-functionalized graphene oxide, *Composites, Part A*, 2014, **64**, 79–89.
98 P.-C. Ma, N. A. Siddiqui, G. Marom and J.-K. Kim, Dispersion and functionalization of carbon nanotubes for polymer-based nanocomposites: a review, *Composites, Part A*, 2010, **41**(10), 1345–1367.
99 M. Moniruzzaman and K. I. Winey, Polymer Nanocomposites Containing Carbon Nanotubes, *Macromolecules*, 2006, **39**(16), 5194–5205.
100 Z. Spitalsky, D. Tasis, K. Papagelis and C. Galiotis, Carbon nanotube–polymer composites: chemistry, processing, mechanical and electrical properties, *Prog. Polym. Sci.*, 2010, **35**(3), 357–401.
101 N. G. Sahoo, S. Rana, J. W. Cho, L. Li and S. H. Chan, Polymer nanocomposites based on functionalized carbon nanotubes, *Prog. Polym. Sci.*, 2010, **35**(7), 837–867.
102 J. N. Coleman, U. Khan, W. J. Blau and Y. K. Gun'ko, Small but strong: a review of the mechanical properties of carbon nanotube–polymer composites, *Carbon*, 2006, **44**(9), 1624–1652.
103 L. Wang, J. Qiu, E. Sakai and X. Wei, The relationship between microstructure and mechanical properties of carbon nanotubes/polylactic acid nanocomposites prepared by twin-screw extrusion, *Composites, Part A*, 2016, **89**, 18–25.
104 M. Arjmand, T. Apperley, M. Okoniewski and U. Sundararaj, Comparative study of electromagnetic interference shielding properties of injection molded versus compression molded multi-walled carbon nanotube/polystyrene composites, *Carbon*, 2012, **50**(14), 5126–5134.
105 F. H. Gojny, M. H. G. Wichmann, U. Köpke, B. Fiedler and K. Schulte, Carbon nanotube-reinforced epoxy-composites: enhanced stiffness and fracture toughness at low nanotube content, *Compos. Sci. Technol.*, 2004, **64**(15), 2363–2371.

106 D. Xiang, E. Harkin-Jones, D. Linton and P. Martin, Structure, mechanical, and electrical properties of high-density polyethylene/multi-walled carbon nanotube composites processed by compression molding and blown film extrusion, *J. Appl. Polym. Sci.*, 2015, **132**(42), 42665.

107 M. A. L. Manchado, L. Valentini, J. Biagiotti and J. M. Kenny, Thermal and mechanical properties of single-walled carbon nanotubes–polypropylene composites prepared by melt processing, *Carbon*, 2005, **43**(7), 1499–1505.

108 M. T. Müller, B. Krause, B. Kretzschmar and P. Pötschke, Influence of a supplemental filler in twin-screw extruded PP/CNT composites using masterbatch dilution, *AIP Conf. Proc.*, 2019, **2055**(1), 090006.

109 M. Hoikkanen, M. Poikelispää, A. Das, U. Reuter, W. Dierkes and J. Vuorinen, Evaluation of mechanical and dynamic mechanical properties of multiwalled carbon nanotube-based ethylene–propylene copolymer composites mixed by masterbatch dilution, *J. Compos. Mater.*, 2016, **50**(29), 4093–4101.

110 I. Burmistrov, N. Gorshkov, I. Ilinykh, D. Muratov, E. Kolesnikov, E. Yakovlev, I. Mazov, J. P. Issi and D. Kuznetsov, Mechanical and electrical properties of ethylene-1-octene and polypropylene composites filled with carbon nanotubes, *Compos. Sci. Technol.*, 2017, **147**, 71–77.

111 G. Vaganov, V. Yudin, J. Vuorinen and E. Molchanov, Influence of multiwalled carbon nanotubes on the processing behavior of epoxy powder compositions and on the mechanical properties of their fiber reinforced composites, *Polym. Compos.*, 2016, **37**(8), 2377–2383.

112 F. F. Alves, A. A. Silva and B. G. Soares, Epoxy—MWCNT composites prepared from master batch and powder dilution: Effect of ionic liquid on dispersion and multifunctional properties, *Polym. Eng. Sci.*, 2018, **58**(10), 1689–1697.

113 T. Villmow, B. Kretzschmar and P. Pötschke, Influence of screw configuration, residence time, and specific mechanical energy in twin-screw extrusion of polycaprolactone/multi-walled carbon nanotube composites, *Compos. Sci. Technol.*, 2010, **70**(14), 2045–2055.

114 P. Pötschke, A. R. Bhattacharyya and A. Janke, Melt mixing of polycarbonate with multiwalled carbon nanotubes: microscopic studies on the state of dispersion, *Eur. Polym. J.*, 2004, **40**(1), 137–148.

115 T. Villmow, P. Pötschke, S. Pegel, L. Häussler and B. Kretzschmar, Influence of twin-screw extrusion conditions on the dispersion of multi-walled carbon nanotubes in a poly(lactic acid) matrix, *Polymer*, 2008, **49**(16), 3500–3509.

116 T. McNally, P. Pötschke, P. Halley, M. Murphy, D. Martin, S. E. J. Bell, G. P. Brennan, D. Bein, P. Lemoine and J. P. Quinn, Polyethylene multiwalled carbon nanotube composites, *Polymer*, 2005, **46**(19), 8222–8232.

117 T. Villmow, S. Pegel, P. Pötschke and U. Wagenknecht, Influence of injection molding parameters on the electrical resistivity of polycarbonate filled with multi-walled carbon nanotubes, *Compos. Sci. Technol.*, 2008, **68**(3), 777–789.

118 P. Pötschke, S. M. Dudkin and I. Alig, Dielectric spectroscopy on melt processed polycarbonate—multiwalled carbon nanotube composites, *Polymer*, 2003, **44**(17), 5023–5030.

119 I. Alig, P. Pötschke, D. Lellinger, T. Skipa, S. Pegel, G. R. Kasaliwal and T. Villmow, Establishment, morphology and properties of carbon nanotube networks in polymer melts, *Polymer*, 2012, **53**(1), 4–28.

120 I. Alig, T. Skipa, D. Lellinger, M. Bierdel and H. Meyer, Dynamic percolation of carbon nanotube agglomerates in a polymer matrix: comparison of different model approaches, *Phys. Status Solidi B*, 2008, **245**(10), 2264–2267.

121 F. Du, J. E. Fischer and K. I. Winey, Coagulation method for preparing single-walled carbon nanotube/poly (methyl methacrylate) composites and their modulus, electrical conductivity, and thermal stability, *J. Polym. Sci., Part B: Polym. Phys.*, 2003, **41**(24), 3333–3338.

122 R. Haggenmueller, J. E. Fischer and K. I. Winey, Single wall carbon nanotube/polyethylene nanocomposites: nucleating and templating polyethylene crystallites, *Macromolecules*, 2006, **39**(8), 2964–2971.

123 K. Wiemann, W. Kaminsky, F. H. Gojny and K. Schulte, Synthesis and Properties of Syndiotactic Poly(propylene)/Carbon Nanofiber and Nanotube Composites Prepared by in situ Polymerization with Metallocene/MAO Catalysts, *Macromol. Chem. Phys.*, 2005, **206**(15), 1472–1478.

124 A. A. Mamedov, N. A. Kotov, M. Prato, D. M. Guldi, J. P. Wicksted and A. Hirsch, Molecular design of strong single-wall carbon nanotube/polyelectrolyte multilayer composites, *Nat. Mater.*, 2002, **1**(3), 190–194.

125 K. J. Loh, J. Kim, J. P. Lynch, N. W. S. Kam and N. A. Kotov, Multifunctional layer-by-layer carbon nanotube–polyelectrolyte thin films for strain and corrosion sensing, *Smart Mater. Struct.*, 2007, **16**(2), 429.

126 M. Olek, J. Ostrander, S. Jurga, H. Möhwald, N. Kotov, K. Kempa and M. Giersig, Layer-by-Layer Assembled Composites from Multiwall Carbon Nanotubes with Different Morphologies, *Nano Lett.*, 2004, **4**(10), 1889–1895.

127 B. S. Shim and N. A. Kotov, Single-walled carbon nanotube combing during layer-by-layer assembly: From random adsorption to aligned composites, *Langmuir*, 2005, **21**(21), 9381–9385.

128 D. E. Bergbreiter and K.-S. Liao, Covalent layer-by-layer assembly—an effective, forgiving way to construct functional robust ultrathin films and nanocomposites, *Soft Matter*, 2009, **5**(1), 23–28.

129 D. Bonduel, M. Mainil, M. Alexandre, F. Monteverde and P. Dubois, Supported coordination polymerization: a unique way to potent polyolefin carbon nanotube nanocomposites, *Chem. Commun.*, 2005, (6), 781–783.

130 S. Peeterbroeck, B. Lepoittevin, E. Pollet, S. Benali, C. Broekaert, M. Alexandre, D. Bonduel, P. Viville,

R. Lazzaroni and P. Dubois, Polymer layered silicate/carbon nanotube nanocomposites: The catalyzed polymerization approach, *Polym. Eng. Sci.*, 2006, **46**(8), 1022–1030.

131 P. Pötschke, S. Pegel, M. Claes and D. Bonduel, A Novel Strategy to Incorporate Carbon Nanotubes into Thermoplastic Matrices, *Macromol. Rapid Commun.*, 2008, **29**(3), 244–251.

132 E. T. Thostenson and T.-W. Chou, Aligned multi-walled carbon nanotube-reinforced composites: processing and mechanical characterization, *J. Phys. D: Appl. Phys.*, 2002, **35**(16), L77.

133 R. Beigmoradi, A. Samimi and D. Mohebbi-Kalhori, Engineering of oriented carbon nanotubes in composite materials, *Beilstein J. Nanotechnol.*, 2018, **9**(1), 415–435.

134 C. Martin, J. Sandler, A. Windle, M.-K. Schwarz, W. Bauhofer, K. Schulte and M. Shaffer, Electric field-induced aligned multi-wall carbon nanotube networks in epoxy composites, *Polymer*, 2005, **46**(3), 877–886.

135 A. I. Oliva-Avilés, F. Avilés and V. Sosa, Electrical and piezoresistive properties of multi-walled carbon nanotube/polymer composite films aligned by an electric field, *Carbon*, 2011, **49**(9), 2989–2997.

136 C. Ma, W. Zhang, Y. Zhu, L. Ji, R. Zhang, N. Koratkar and J. Liang, Alignment and dispersion of functionalized carbon nanotubes in polymer composites induced by an electric field, *Carbon*, 2008, **46**(4), 706–710.

137 S. U. Khan, J. R. Pothnis and J.-K. Kim, Effects of carbon nanotube alignment on electrical and mechanical properties of epoxy nanocomposites, *Composites, Part A*, 2013, **49**, 26–34.

138 Y.-F. Zhu, C. Ma, W. Zhang, R.-P. Zhang, N. Koratkar and J. Liang, Alignment of multiwalled carbon nanotubes in bulk epoxy composites via electric field, *J. Appl. Phys.*, 2009, **105**(5), 054319.

139 M. Abdalla, D. Dean, M. Theodore, J. Fielding, E. Nyairo and G. Price, Magnetically processed carbon nanotube/epoxy nanocomposites: Morphology, thermal, and mechanical properties, *Polymer*, 2010, **51**(7), 1614–1620.

140 Y. He, S. Yang, H. Liu, Q. Shao, Q. Chen, C. Lu, Y. Jiang, C. Liu and Z. Guo, Reinforced carbon fiber laminates with oriented carbon nanotube epoxy nanocomposites: Magnetic field assisted alignment and cryogenic temperature mechanical properties, *J. Colloid Interface Sci.*, 2018, **517**, 40–51.

141 C. Ma, H.-Y. Liu, X. Du, L. Mach, F. Xu and Y.-W. Mai, Fracture resistance, thermal and electrical properties of epoxy composites containing aligned carbon nanotubes by low magnetic field, *Compos. Sci. Technol.*, 2015, **114**, 126–135.

142 C. Du, M. Li, M. Cao, S. Feng, H. Guo and B. Li, Enhanced thermal and mechanical properties of polyvinlydene fluoride composites with magnetic oriented carbon nanotube, *Carbon*, 2018, **126**, 197–207.

143 T. Kimura, H. Ago, M. Tobita, S. Ohshima, M. Kyotani and M. Yumura, Polymer composites of carbon nanotubes aligned by a magnetic field, *Adv. Mater.*, 2002, **14**(19), 1380–1383.

144 E. Camponeschi, R. Vance, M. Al-Haik, H. Garmestani and R. Tannenbaum, Properties of carbon nanotube–polymer composites aligned in a magnetic field, *Carbon*, 2007, **45**(10), 2037–2046.

145 M. Arjmand, M. Mahmoodi, G. A. Gelves, S. Park and U. Sundararaj, Electrical and electromagnetic interference shielding properties of flow-induced oriented carbon nanotubes in polycarbonate, *Carbon*, 2011, **49**(11), 3430–3440.

146 Y. A. Kim, T. Hayashi, M. Endo, Y. Gotoh, N. Wada and J. Seiyama, Fabrication of aligned carbon nanotube-filled rubber composite, *Scr. Mater.*, 2006, **54**(1), 31–35.

147 T. H. Nam, K. Goto, K. Oshima, E. V. A. Premalal, Y. Shimamura, Y. Inoue, K. Naito and S. Ogihara, Mechanical property enhancement of aligned multi-walled carbon nanotube sheets and composites through press-drawing process, *Adv. Compos. Mater.*, 2016, **25**(1), 73–86.

148 P. Pötschke, H. Brünig, A. Janke, D. Fischer and D. Jehnichen, Orientation of multiwalled carbon nanotubes in composites with polycarbonate by melt spinning, *Polymer*, 2005, **46**(23), 10355–10363.

149 Q. Wang, J. Dai, W. Li, Z. Wei and J. Jiang, The effects of CNT alignment on electrical conductivity and mechanical properties of SWNT/epoxy nanocomposites, *Compos. Sci. Technol.*, 2008, **68**(7), 1644–1648.

150 C. Jolowsky, R. Sweat, J. G. Park, A. Hao and R. Liang, Microstructure evolution and self-assembling of CNT networks during mechanical stretching and mechanical properties of highly aligned CNT composites, *Compos. Sci. Technol.*, 2018, **166**, 125–130.

151 L. Jin, C. Bower and O. Zhou, Alignment of carbon nanotubes in a polymer matrix by mechanical stretching, *Appl. Phys. Lett.*, 1998, **73**(9), 1197–1199.

152 S. D. McCullen, D. R. Stevens, W. A. Roberts, S. S. Ojha, L. I. Clarke and R. E. Gorga, Morphological, Electrical, and Mechanical Characterization of Electrospun Nanofiber Mats Containing Multiwalled Carbon Nanotubes, *Macromolecules*, 2007, **40**(4), 997–1003.

153 L. Jiang, H. Tu, Y. Lu, Y. Wu, J. Tian, X. Shi, Q. Wang, Y. Zhan, Z. Huang and H. Deng, Spherical and rodlike inorganic nanoparticle regulated the orientation of carbon nanotubes in polymer nanofibers, *Chem. Phys. Lett.*, 2016, **650**, 82–87.

154 H. Hou, J. J. Ge, J. Zeng, Q. Li, D. H. Reneker, A. Greiner and S. Z. D. Cheng, Electrospun Polyacrylonitrile Nanofibers Containing a High Concentration of Well-Aligned Multiwall Carbon Nanotubes, *Chem. Mater.*, 2005, **17**(5), 967–973.

155 F. Ko, Y. Gogotsi, A. Ali, N. Naguib, H. Ye, G. Yang, C. Li and P. Willis, Electrospinning of continuous carbon nanotube-filled nanofiber yarns, *Adv. Mater.*, 2003, **15**(14), 1161–1165.

156 R. Sen, B. Zhao, D. Perea, M. E. Itkis, H. Hu, J. Love, E. Bekyarova and R. C. Haddon, Preparation of Single-Walled Carbon Nanotube Reinforced Polystyrene and Polyurethane Nanofibers and Membranes by Electrospinning, *Nano Lett.*, 2004, **4**(3), 459–464.

157 Y. Song, Z. Sun, L. Xu and Z. Shao, Preparation and Characterization of Highly Aligned Carbon Nanotubes/Polyacrylonitrile Composite Nanofibers, *Polymers*, 2017, **9**(1), 1.

158 S. G. King, N. J. Terrill, A. J. Goodwin, R. Stevens, V. Stolojan and S. R. P. Silva, Probing of polymer to carbon nanotube surface interactions within highly aligned electrospun nanofibers for advanced composites, *Carbon*, 2018, **138**, 207–214.

159 L.-Y. Mei, P. Song and Y.-Q. Liu, Magnetic-field-assisted electrospinning highly aligned composite nanofibers containing well-aligned multiwalled carbon nanotubes, *J. Appl. Polym. Sci.*, 2015, **132**(22), 41995.

160 N. Shehata, E. Elnabawy, M. Abdelkader, A. H. Hassanin, M. Salah, R. Nair and S. Ahmad Bhat, Static-Aligned Piezoelectric Poly (Vinylidene Fluoride) Electrospun Nanofibers/MWCNT Composite Membrane: Facile Method, *Polymers*, 2018, **10**(9), 965.

161 T. Liu and S. Kumar, Quantitative characterization of SWNT orientation by polarized Raman spectroscopy, *Chem. Phys. Lett.*, 2003, **378**(3–4), 257–262.

162 M. Van Gurp, The use of rotation matrices in the mathematical description of molecular orientations in polymers, *Colloid Polym. Sci.*, 1995, **273**(7), 607–625.

163 H. Krenchel, *Fibre reinforcement; theoretical and practical investigations of the elasticity and strength of fibre-reinforced materials*, Akademisk Forlag, Copenhagen, 1964.

164 J. B. Bai and A. Allaoui, Effect of the length and the aggregate size of MWNTs on the improvement efficiency of the mechanical and electrical properties of nanocomposites—experimental investigation, *Composites, Part A*, 2003, **34**(8), 689–694.

165 K. Lu, R. Lago, Y. Chen, M. Green, P. Harris and S. Tsang, Mechanical damage of carbon nanotubes by ultrasound, *Carbon*, 1996, **34**(6), 814–816.

166 H. Wan, F. Delale and L. Shen, Effect of CNT length and CNT-matrix interphase in carbon nanotube (CNT) reinforced composites, *Mech. Res. Commun.*, 2005, **32**(5), 481–489.

167 X. Wang, Q. Jiang, W. Xu, W. Cai, Y. Inoue and Y. Zhu, Effect of carbon nanotube length on thermal, electrical and mechanical properties of CNT/bismaleimide composites, *Carbon*, 2013, **53**, 145–152.

168 L. Schadler, S. A. Giannaris and P. Ajayan, Load transfer in carbon nanotube epoxy composites, *Appl. Phys. Lett.*, 1998, **73**(26), 3842–3844.

169 M. Cadek, J. N. Coleman, K. P. Ryan, V. Nicolosi, G. Bister, A. Fonseca, J. B. Nagy, K. Szostak, F. Béguin and W. J. Blau, Reinforcement of Polymers with Carbon Nanotubes: The Role of Nanotube Surface Area, *Nano Lett.*, 2004, **4**(2), 353–356.

170 A. H. Barber, S. R. Cohen, S. Kenig and H. D. Wagner, Interfacial fracture energy measurements for multi-walled carbon nanotubes pulled from a polymer matrix, *Compos. Sci. Technol.*, 2004, **64**(15), 2283–2289.

171 E. T. Thostenson and T.-W. Chou, On the elastic properties of carbon nanotube-based composites: modelling and characterization, *J. Phys. D: Appl. Phys.*, 2003, **36**(5), 573.

172 L. H. Shao, R. Y. Luo, S. L. Bai and J. Wang, Prediction of effective moduli of carbon nanotube–reinforced composites with waviness and debonding, *Compos. Struct.*, 2009, **87**(3), 274–281.

173 J. Nafar Dastgerdi, G. Marquis and M. Salimi, The effect of nanotubes waviness on mechanical properties of CNT/SMP composites, *Compos. Sci. Technol.*, 2013, **86**, 164–169.

174 A. Alian and S. Meguid, Molecular dynamics simulations of the effect of waviness and agglomeration of CNTs on interface strength of thermoset nanocomposites, *Phys. Chem. Chem. Phys.*, 2017, **19**(6), 4426–4434.

175 U. A. Joshi, S. C. Sharma and S. P. Harsha, Effect of carbon nanotube orientation on the mechanical properties of nanocomposites, *Composites, Part B*, 2012, **43**(4), 2063–2071.

176 U. A. Joshi, S. C. Sharma and S. P. Harsha, Effect of waviness on the mechanical properties of carbon nanotube based composites, *Phys. E*, 2011, **43**(8), 1453–1460.

177 R. Rafiee, Influence of carbon nanotube waviness on the stiffness reduction of CNT/polymer composites, *Compos. Struct.*, 2013, **97**, 304–309.

178 A. Y. Matveeva, S. V. Pyrlin, M. M. D. Ramos, H. J. Böhm and F. W. J. van Hattum, Influence of waviness and curliness of fibres on mechanical properties of composites, *Comput. Mater. Sci.*, 2014, **87**, 1–11.

179 C. Li and T.-W. Chou, Failure of carbon nanotube/polymer composites and the effect of nanotube waviness, *Composites, Part A*, 2009, **40**(10), 1580–1586.

180 F. T. Fisher, R. D. Bradshaw and L. C. Brinson, Fiber waviness in nanotube-reinforced polymer composites—I: Modulus predictions using effective nanotube properties, *Compos. Sci. Technol.*, 2003, **63**(11), 1689–1703.

181 R. D. Bradshaw, F. T. Fisher and L. C. Brinson, Fiber waviness in nanotube-reinforced polymer composites—II: modeling via numerical approximation of the dilute strain concentration tensor, *Compos. Sci. Technol.*, 2003, **63**(11), 1705–1722.

182 D. Tasis, N. Tagmatarchis, A. Bianco and M. Prato, Chemistry of Carbon Nanotubes, *Chem. Rev.*, 2006, **106**(3), 1105–1136.

183 H. Kim and C. W. Macosko, Processing-property relationships of polycarbonate/graphene composites, *Polymer*, 2009, **50**(15), 3797–3809.

184 S. Uchida, T. Murakami, T. Iwamura, R. Ishige and S. Ando, Enhanced thermal conductivity in immiscible polyimide blend composites with needle-shaped ZnO particles, *RSC Adv.*, 2017, **7**(25), 15492–15499.

185 T. Fornes and D. R. Paul, Modeling properties of nylon 6/clay nanocomposites using composite theories, *Polymer*, 2003, **44**(17), 4993–5013.
186 X. Lin, X. Shen, Q. Zheng, N. Yousefi, L. Ye, Y.-W. Mai and J.-K. Kim, Fabrication of highly-aligned, conductive, and strong graphene papers using ultralarge graphene oxide sheets, *ACS Nano*, 2012, **6**(12), 10708–10719.
187 H. Liu and L. C. Brinson, Reinforcing efficiency of nanoparticles: A simple comparison for polymer nanocomposites, *Compos. Sci. Technol.*, 2008, **68**(6), 1502–1512.
188 Z. Li, J. Chu, C. Yang, S. Hao, M. A. Bissett, I. A. Kinloch and R. J. Young, Effect of functional groups on the agglomeration of graphene in nanocomposites, *Compos. Sci. Technol.*, 2018, **163**, 116–122.
189 M. Omidi, H. Rokni D. T., A. S. Milani, R. J. Seethaler and R. Arasteh, Prediction of the mechanical characteristics of multi-walled carbon nanotube/epoxy composites using a new form of the rule of mixtures, *Carbon*, 2010, **48**(11), 3218–3228.
190 R. J. Young and P. A. Lovell, *Introduction to polymers*, CRC Press, 2011.
191 A. Kelly, *Strong Solids*, Clarendon Press, 1966.
192 J. A. Nairn, On the use of shear-lag methods for analysis of stress transfer in unidirectional composites, *Mech. Mater.*, 1997, **26**(2), 63–80.
193 R. Young, *Composite micromechanics: From carbon fibres to graphene*, Structural Integrity and Durability of Advanced Composites, Elsevier, 2015, pp. 3–23.
194 M. Andrews and R. Young, Fragmentation of aramid fibres in single-fibre model composites, *J. Mater. Sci.*, 1995, **30**(22), 5607–5616.
195 R. J. Young, M. Liu, I. A. Kinloch, S. Li, X. Zhao, C. Vallés and D. G. Papageorgiou, The mechanics of reinforcement of polymers by graphene nanoplatelets, *Compos. Sci. Technol.*, 2018, **154**, 110–116.
196 M. Terrones, O. Martín, M. González, J. Pozuelo, B. Serrano, J. C. Cabanelas, S. M. Vega-Díaz and J. Baselga, Interphases in Graphene Polymer-based Nanocomposites: Achievements and Challenges, *Adv. Mater.*, 2011, **23**(44), 5302–5310.
197 M. Piggott, Why interface testing by single-fibre methods can be misleading, *Compos. Sci. Technol.*, 1997, **57**(8), 965–974.
198 R. J. Young, I. A. Kinloch, L. Gong and K. S. Novoselov, The mechanics of graphene nanocomposites: a review, *Compos. Sci. Technol.*, 2012, **72**(12), 1459–1476.
199 M. Liu, I. A. Kinloch, R. J. Young and D. G. Papageorgiou, Modelling mechanical percolation in graphene-reinforced elastomer nanocomposites, arXiv preprint arXiv:1903.10224, 2019.
200 J. C. Halpin and J. Kardos, The Halpin-Tsai equations: a review, *Polym. Eng. Sci.*, 1976, **16**(5), 344–352.
201 T. Mori and K. Tanaka, Average stress in matrix and average elastic energy of materials with misfitting inclusions, *Acta Metall.*, 1973, **21**(5), 571–574.
202 J. Liang, Y. Huang, L. Zhang, Y. Wang, Y. Ma, T. Guo and Y. Chen, Molecular-level dispersion of graphene into poly (vinyl alcohol) and effective reinforcement of their nanocomposites, *Adv. Funct. Mater.*, 2009, **19**(14), 2297–2302.
203 X. Zhang, T. Liu, T. Sreekumar, S. Kumar, V. C. Moore, R. H. Hauge and R. E. Smalley, Poly (vinyl alcohol)/SWNT composite film, *Nano Lett.*, 2003, **3**(9), 1285–1288.
204 X.-Y. Ji, Y.-P. Cao and X.-Q. Feng, Micromechanics prediction of the effective elastic moduli of graphene sheet-reinforced polymer nanocomposites, *Modell. Simul. Mater. Sci. Eng.*, 2010, **18**(4), 045005.
205 D. S. Bethune, G. Meijer, W. C. Tang, H. J. Rosen, W. G. Golden, H. Seki, C. A. Brown and M. S. de Vries, Vibrational Raman and infrared spectra of chromatographically separated C60 and C70 fullerene clusters, *Chem. Phys. Lett.*, 1991, **179**(1–2), 181–186.
206 M. Dresselhaus, G. Dresselhaus and P. Eklund, Raman scattering in fullerenes, *J. Raman Spectrosc.*, 1996, **27**(3–4), 351–371.
207 M. S. Dresselhaus, G. Dresselhaus, R. Saito and A. Jorio, Raman spectroscopy of carbon nanotubes, *Phys. Rep.*, 2005, **409**(2), 47–99.
208 A. C. Ferrari, J. Meyer, V. Scardaci, C. Casiraghi, M. Lazzeri, F. Mauri, S. Piscanec, D. Jiang, K. Novoselov and S. Roth, Raman spectrum of graphene and graphene layers, *Phys. Rev. Lett.*, 2006, **97**(18), 187401.
209 F. Tuinstra and J. L. Koenig, Raman spectrum of graphite, *J. Chem. Phys.*, 1970, **53**(3), 1126–1130.
210 L. Malard, M. Guimaraes, D. Mafra and A. Jorio, Group-theory analysis of electrons and phonons in N-layer graphene systems, *Phys. Rev. B: Condens. Matter Mater. Phys.*, 2009, **79**(12), 125426.
211 A. Rao, E. Richter, S. Bandow, B. Chase, P. Eklund, K. Williams, S. Fang, K. Subbaswamy, M. Menon and A. Thess, Diameter-selective Raman scattering from vibrational modes in carbon nanotubes, *Science*, 1997, **275**(5297), 187–191.
212 A. C. Ferrari, Raman spectroscopy of graphene and graphite: disorder, electron–phonon coupling, doping and non-adiabatic effects, *Solid State Commun.*, 2007, **143**(1–2), 47–57.
213 A. C. Ferrari and D. M. Basko, Raman spectroscopy as a versatile tool for studying the properties of graphene, *Nat. Nanotechnol.*, 2013, **8**(4), 235.
214 M. S. Dresselhaus, A. Jorio, M. Hofmann, G. Dresselhaus and R. Saito, Perspectives on carbon nanotubes and graphene Raman spectroscopy, *Nano Lett.*, 2010, **10**(3), 751–758.
215 R. J. Young and S. J. Eichhorn, Deformation mechanisms in polymer fibres and nanocomposites, *Polymer*, 2007, **48**(1), 2–18.
216 A. C. Ferrari, J. C. Meyer, V. Scardaci, C. Casiraghi, M. Lazzeri, F. Mauri, S. Piscanec, D. Jiang, K. S. Novoselov, S. Roth and A. K. Geim, Raman Spectrum

of Graphene and Graphene Layers, *Phys. Rev. Lett.*, 2006, **97**(18), 187401.

217 T. M. G. Mohiuddin, A. Lombardo, R. R. Nair, A. Bonetti, G. Savini, R. Jalil, N. Bonini, D. M. Basko, C. Galiotis, N. Marzari, K. S. Novoselov, A. K. Geim and A. C. Ferrari, Uniaxial strain in graphene by Raman spectroscopy: *G* peak splitting, Grüneisen parameters, and sample orientation, *Phys. Rev. B: Condens. Matter Mater. Phys.*, 2009, **79**(20), 205433.

218 G. Tsoukleri, J. Parthenios, K. Papagelis, R. Jalil, A. C. Ferrari, A. K. Geim, K. S. Novoselov and C. Galiotis, Subjecting a graphene monolayer to tension and compression, *Small*, 2009, **5**(21), 2397–2402.

219 T. M. G. Mohiuddin, A. Lombardo, R. R. Nair, A. Bonetti, G. Savini, R. Jalil, N. Bonini, D. M. Basko, C. Galiotis, N. Marzari, K. S. Novoselov, A. K. Geim and A. C. Ferrari, Uniaxial strain in graphene by Raman spectroscopy: G peak splitting, Gruneisen parameters, and sample orientation, *Phys. Rev. B: Condens. Matter Mater. Phys.*, 2009, **79**(20), 205433.

220 I. Polyzos, M. Bianchi, L. Rizzi, E. N. Koukaras, J. Parthenios, K. Papagelis, R. Sordan and C. Galiotis, Suspended monolayer graphene under true uniaxial deformation, *Nanoscale*, 2015, **7**(30), 13033–13042.

221 L. Gong, R. J. Young, I. A. Kinloch, I. Riaz, R. Jalil and K. S. Novoselov, Optimizing the reinforcement of polymer-based nanocomposites by graphene, *ACS Nano*, 2012, **6**(3), 2086–2095.

222 G. Tsoukleri, J. Parthenios, C. Galiotis and K. Papagelis, Embedded trilayer graphene flakes under tensile and compressive loading, *2D Mater.*, 2015, **2**(2), 024009.

223 G. Anagnostopoulos, C. Androulidakis, E. N. Koukaras, G. Tsoukleri, I. Polyzos, J. Parthenios, K. Papagelis and C. Galiotis, Stress transfer mechanisms at the submicron level for graphene/polymer systems, *ACS Appl. Mater. Interfaces*, 2015, **7**(7), 4216–4223.

224 O. Frank, G. Tsoukleri, I. Riaz, K. Papagelis, J. Parthenios, A. C. Ferrari, A. K. Geim, K. S. Novoselov and C. Galiotis, Development of a universal stress sensor for graphene and carbon fibres, *Nat. Commun.*, 2011, **2**, 255.

225 N. Melanitis, P. L. Tetlow and C. Galiotis, Characterization of PAN-based carbon fibres with laser Raman spectroscopy, *J. Mater. Sci.*, 1996, **31**(4), 851–860.

226 Y. Huang and R. J. Young, Effect of fibre microstructure upon the modulus of PAN- and pitch-based carbon fibres, *Carbon*, 1995, **33**(2), 97–107.

227 G. Wang, Z. Dai, L. Liu, H. Hu, Q. Dai and Z. Zhang, Tuning the Interfacial Mechanical Behaviors of Monolayer Graphene/PMMA Nanocomposites, *ACS Appl. Mater. Interfaces*, 2016, **8**(34), 22554–22562.

228 J. Zabel, R. R. Nair, A. Ott, T. Georgiou, A. K. Geim, K. S. Novoselov and C. Casiraghi, Raman spectroscopy of graphene and bilayer under biaxial strain: bubbles and balloons, *Nano Lett.*, 2012, **12**(2), 617–621.

229 F. Ding, H. Ji, Y. Chen, A. Herklotz, K. Dörr, Y. Mei, A. Rastelli and O. G. Schmidt, Stretchable graphene: a close look at fundamental parameters through biaxial straining, *Nano Lett.*, 2010, **10**(9), 3453–3458.

230 C. Androulidakis, E. N. Koukaras, J. Parthenios, G. Kalosakas, K. Papagelis and C. Galiotis, Graphene flakes under controlled biaxial deformation, *Sci. Rep.*, 2015, **5**, 18219.

231 C. Metzger, S. Rémi, M. Liu, S. V. Kusminskiy, A. H. Castro Neto, A. K. Swan and B. B. Goldberg, Biaxial strain in graphene adhered to shallow depressions, *Nano Lett.*, 2009, **10**(1), 6–10.

232 Z. Li, I. A. Kinloch, R. J. Young, K. S. Novoselov, G. Anagnostopoulos, J. Parthenios, C. Galiotis, K. Papagelis, C.-Y. Lu and L. Britnell, Deformation of wrinkled graphene, *ACS Nano*, 2015, **9**(4), 3917–3925.

233 G. Anagnostopoulos, G. Paterakis, I. Polyzos, P.-N. Pappas, K. Kouroupis-Agalou, N. Mirotta, A. Scida, V. Palermo, J. Parthenios and K. Papagelis, Strain Engineering in Highly Wrinkled CVD Graphene/Epoxy Systems, *ACS Appl. Mater. Interfaces*, 2018, **10**(49), 43192–43202.

234 M. G. P. Carbone, A. C. Manikas, I. Souli, C. Pavlou and C. Galiotis, Mosaic pattern formation in exfoliated graphene by mechanical deformation, *Nat. Commun.*, 2019, **10**(1), 1572.

235 Z. Li, R. J. Young, D. Papageorgiou, I. Kinloch, X. Zhao, C. Yang and S.-J. Hao, Interfacial stress transfer in strain engineered wrinkled and folded graphene, *2D Mater.*, 2019, **6**(4), 045026.

236 Z. Li, I. A. Kinloch and R. J. Young, The role of interlayer adhesion in graphene oxide upon its reinforcement of nanocomposites, *Philos. Trans. R. Soc., A*, 2016, **374**(2071), 20150283.

237 R. J. Young, L. Gong, I. A. Kinloch, I. Riaz, R. Jalil and K. S. Novoselov, Strain mapping in a graphene monolayer nanocomposite, *ACS Nano*, 2011, **5**(4), 3079–3084.

238 J. Morgan, M. Craciun and S. Eichhorn, Quantification of stress transfer in a model cellulose nanocrystal/graphene bilayer using Raman spectroscopy, *Compos. Sci. Technol.*, 2019, **177**, 34–40.

239 O. Frank, G. Tsoukleri, J. Parthenios, K. Papagelis, I. Riaz, R. Jalil, K. S. Novoselov and C. Galiotis, Compression behavior of single-layer graphenes, *ACS Nano*, 2010, **4**(6), 3131–3138.

240 A. Ferrari, J. Robertson, A. Jorio, R. Saito, G. Dresselhaus and M. S. Dresselhaus, Determination of nanotubes properties by Raman spectroscopy, *Philos. Trans. R. Soc., A*, 2004, **362**(1824), 2311–2336.

241 J. Wood, Q. Zhao and H. Wagner, Orientation of carbon nanotubes in polymers and its detection by Raman spectroscopy, *Composites, Part A*, 2001, **32**(3–4), 391–399.

242 H. Gommans, J. Alldredge, H. Tashiro, J. Park, J. Magnuson and A. Rinzler, Fibers of aligned single-walled carbon nanotubes: Polarized Raman spectroscopy, *J. Appl. Phys.*, 2000, **88**(5), 2509–2514.

243 T. E. Chang, L. R. Jensen, A. Kisliuk, R. B. Pipes, R. Pyrz and A. P. Sokolov, Microscopic mechanism of reinforcement in single-wall carbon nanotube/polypropylene nanocomposite, *Polymer*, 2005, **46**(2), 439–444.

244 Z. Wang, P. Ciselli and T. Peijs, The extraordinary reinforcing efficiency of single-walled carbon nanotubes in oriented poly (vinyl alcohol) tapes, *Nanotechnology*, 2007, **18**(45), 455709.
245 S. Iijima and T. Ichihashi, Single-shell carbon nanotubes of 1 nm diameter, *Nature*, 1993, **363**(6430), 603.
246 C. A. Cooper, R. J. Young and M. Halsall, Investigation into the deformation of carbon nanotubes and their composites through the use of Raman spectroscopy, *Composites, Part A*, 2001, **32**(3), 401–411.
247 M. Frogley, Q. Zhao and H. Wagner, Polarized resonance Raman spectroscopy of single-wall carbon nanotubes within a polymer under strain, *Phys. Rev. B: Condens. Matter Mater. Phys.*, 2002, **65**(11), 113413.
248 L. Deng, S. J. Eichhorn, C.-C. Kao and R. J. Young, The effective Young's modulus of carbon nanotubes in composites, *ACS Appl. Mater. Interfaces*, 2011, **3**(2), 433–440.
249 S. Wang, Z. Liang, P. Gonnet, Y. H. Liao, B. Wang and Z. Zhang, Effect of Nanotube Functionalization on the Coefficient of Thermal Expansion of Nanocomposites, *Adv. Funct. Mater.*, 2007, **17**(1), 87–92.
250 S. Wang, R. Liang, B. Wang and C. Zhang, Load-transfer in functionalized carbon nanotubes/polymer composites, *Chem. Phys. Lett.*, 2008, **457**(4), 371–375.
251 Q. Zhao and H. D. Wagner, Raman spectroscopy of carbon–nanotube–based composites, *Philos. Trans. R. Soc., A*, 2004, **362**(1824), 2407–2424.
252 R. J. Young, L. Deng, T. Z. Wafy and I. A. Kinloch, Interfacial and internal stress transfer in carbon nanotube based nanocomposites, *J. Mater. Sci.*, 2016, **51**(1), 344–352.
253 M. Mu, S. Osswald, Y. Gogotsi and K. I. Winey, An in situ Raman spectroscopy study of stress transfer between carbon nanotubes and polymer, *Nanotechnology*, 2009, **20**(33), 335703.
254 C.-C. Kao and R. J. Young, Assessment of interface damage during the deformation of carbon nanotube composites, *J. Mater. Sci.*, 2010, **45**(6), 1425–1431.
255 L. Liu, A. H. Barber, S. Nuriel and H. D. Wagner, Mechanical properties of functionalized single-walled carbon-nanotube/poly (vinyl alcohol) nanocomposites, *Adv. Funct. Mater.*, 2005, **15**(6), 975–980.
256 N. Lachman, C. Bartholome, P. Miaudet, M. Maugey, P. Poulin and H. D. Wagner, Raman Response of Carbon Nanotube/PVA Fibers under Strain, *J. Phys. Chem. C*, 2009, **113**(12), 4751–4754.
257 S. Y. Jin, R. J. Young and S. J. Eichhorn, Controlling and mapping interfacial stress transfer in fragmented hybrid carbon fibre–carbon nanotube composites, *Compos. Sci. Technol.*, 2014, **100**, 121–127.
258 S. Y. Jin, R. J. Young and S. J. Eichhorn, Hybrid carbon fibre–carbon nanotube composite interfaces, *Compos. Sci. Technol.*, 2014, **95**, 114–120.